Crustal movements 2005-2007 in the Kárahnjúkar area, NE-Iceland, in relation to formation of the Hálslón water reservoir

Benedikt Gunnar Ófeigsson

UNIVERSITY OF ICELAND

A thesis submitted for a degree of Master of Science in Geophysics

FACULTY OF SCIENCE
DEPARTMENT OF PHYSICS
February, 2008

Supervisors:
Páll Einarsson
Freysteinn Sigmundsson

Crustal movements 2005-2007 in the Kárahnjúkar area, NE-Iceland, in relation to formation of the Hálslón water reservoir

ISBN 978-9979-9633-2-5
Printed by Oddi

This thesis can also be referred to as
Nordic Volcanological Center, Institute of Earth Sciences,
University of Iceland, Report 0801

Hér með lýsi ég því yfir að ritgerð þessi er samin af mér og að hún hefur hvorki að hluta né í heild verið lögð fram áður til hærri prófgráðu.

_____

Benedikt Gunnar Ófeigsson

Abstract

A major 2.4 km^3 water reservoir (Hálslón) was formed north of the Vatnajökull ice cap, Iceland, as a part of the Kárahnjúkar hydroelectric project. The Hálslón reservoir, which is located at the eastern edge of the plate boundary deformation zone in North Iceland, is 198 m deep with surface area of 57 km^2 when full. The filling began on September 28, 2006 and the reservoir was full for the first time at the end of August 2007. The load that is consequently being applied on the crust gives a good opportunity to study the characteristics of the crustal response. The reservoir partly overlies a fault system that has been active during the Holocene. An extensive network for crustal deformation research was established in 2005. A total of 35 benchmarks were measured in GPS-campaigns in August, 2005, 2006 and 2007 as described in this thesis. Complimentary geodetic efforts include establishment of eight continuously measuring GPS-stations for resolving temporal changes in the Hálslón area. The first of these was established in October, 2004, three in fall 2005 and the other four in September 2006. Known crustal movements in the area prior to the filling were uplift associated with decreasing load of the nearby Vatnajökull ice cap and seasonal variations due to the annual change in snow load. The uplift rate, infered from GPS-measurements described here, is 20-30 mm/yr at 50 km distance from the centre of mass of Vatnajökull which is comparable to previous studies. The uplift rate close to Hálslón (73 km from Vatnajökull's centre) was (15 ± 8) mm/yr in 2005-2006. In addition, local deformation has been detected during the period of initial filling of Hálslón. The average uplift rate close to Hálslón reduced to (2 ± 7) mm/yr in 2006-2007, signifying an average measured subsidence of (14 ± 10) mm due to the resevoir filling. Horizontal displacements close to the dams show an extension across Hálslón (39 ± 6) mm in direction $(329 \pm 7)°$. This suggests widening of faults underlying Hálslón. In the far region a significant asymmetry is observed from west to east across Hálslón. Horizontal displacements of 10-15 mm toward Hálslón are observed west of it, but insignificant displacements are observed east of Hálslón. It is infered that crustal parameters may change significantly with distance from the plate boundary. Comparison of the observed displacements with modelled elastic response from the weight of Hálslón, on a half space using a Young's modulus of 30 GPa, predicts somewhat more subsidence than observed. The predicted horizontal displacements are comparable to the horizontal displacements observed west of Hálslón. This indicates that the crust in the area can not be characterised with a single Young's modulus.

Ágrip

Hið 2.4 km^3 Miðlunarlón, Hálslón, sem er hluti af Kárahnjúkavirkjun, hefur verið fyllt norðan Vatnajökuls. Lónið er staðsett rétt austan við Norður gosbeltið og þegar það er fullt verður það 198 m djúpt þar sem það er dýpst og er 57 km^2 að flatarmáli. Fylling lónsins hófst þann 28. september, 2006 og það var orðið fullt í lok ágúst, 2007. Þær hreyfingar á jarðskorpunni sem fargið veldur gefur mjög gott tækifæri til að rannsaka einginleika hennar. Því til viðbótar liggur lónið að hluta til ofan á sprungukerfi sem hefur að einhverju leyti verið virkt á nútíma. Árið 2005 var sett upp net af 35 GPS mælipunktum til að rannsaka jarðskorpuhreyfingar umhverfis Hálslón. Þetta net ásamt nokkrum öðrum eldri merkjum, í nágrenni við Hálslón, var mælt í ágúst 2005, 2006 og 2007 og munu þessar mælingar vera megin viðfangsefni þessarar ritgerðar. Til viðbótar við þessar mælingar voru átta samfellt mælandi GPS stöðvar settar upp á svæðinu, sú fyrsta í október 2004, þrjár um haustið 2005 og síðustu fjórar september 2006. Þekktar jarðskorpuhreyfingar á svæðinu fyrir fyllingu Hálslóns eru landris vegna rýrnunar Vatnajökuls, árssveiflur vegna ákomu jökla á veturna. Landrisið mælist 20-30 mm/yr í 50 km fjarlægð frá miðju Vatnajökuls sem er í samræmi við það sem áður hefur verið mælt. Landrisið nálægt Hálslóni (73 km frá miðju Vatnajökuls) mældist um (15±8) mm/ár á bilinu 2005-2006. Á tímabilinu meðan fylling Hálslóns stóð yfir, 2006-2007, minnkaði landrisið í (2 ± 7) mm/ár sem bendir til sigs upp á (14 ± 10) mm, meðan á fyllingu stóð. Láréttar hreyfingar nálægt stíflumannvirkjunum sýna gliðnun yfir lónið, (39 ± 6) mm í stefnu $(329 \pm 7)^\circ$ sem bendir til hugsanlegrar gliðnunar á sprungum undir lóninu. Lengra frá stíflustæðinu gætir hins vegar ósamhverfu vestan og austan við Hálslón. Vestan við lónið sjást hreyfingar, 10-15 mm í átt að lóninu en austan við það sjást nánast engar hreyfingar. Þetta gæti bent til að eiginleikar jarðskorpunnar breytist talsvert eftir því sem fjarlægð frá flekaskilunum vex. Samanburður mælinga við líkan, sem gerir ráð fyrir þunga Hálslóns ofan á fjaðrandi hálfrúmi með fjaðurstuðul 30 GPa, sýnir að mælt sig er ívið minna en líkanið spáir fyrir um. Láréttar færslur vestan við Hálslón eru í góðu samræmi við líkanið. Þetta bendir til þess að gera þurfi ráð fyrir breytilegum fjaðureiginleikum jarðskorpunnar.

Acknowledgements

The GPS measurements in the Kárahnjúkar area 2005, 2006 and 2007 were funded by The National Energy Company (Landsvirkjun).

Erik Sturkell, Halldór Ólafsson, Jón Thuy Xuan Búi, Páll Einarsson, Magnús Pálsson, Ronni Grapenthin, Freysteinn Sigmundsson, Haukur Brynjólfsson and Ásta Rut Hjartardóttir participated in the GPS measurements.

I would especially like to thank my supervisors Freysteinn Sigmundsson and Páll Einarsson for their very good guidance and support. Erik Sturkell and Halldór Ólafsson have my special thanks for their support and guidance and for being an extra pair of supervisors and co-workers on this project. I would like to thank Rósa Ólafsdóttir for providing the topographic data, Finnur Pálsson for providing the Vatnajökull outline data, Kristján Sæmundsson for his map of faults in Kárahnjúkar and Ronni Grapenthin for the model figure and Theodór Theodórsson for the topographic data at Kárahnjúkar. I would like to thank Jón Thuy Xuan Búi (from Landsvirkjun) for his participation in the measurements. I would especially like to thank Yrsa Sigurðardóttir for all her help at the Kárahnjúkar camp as well as all the people who assisted us during the campaigns and made us feel welcome. I would like to thank Þóra Árnadóttir for her help with the GPS processing. I would like to thank the staff at the Institute of Earth Sciences for all assistance and support during this work.

Finally I would like to thank my family for their support especially I would like to thank my wife Þórunn Ósk Þorgeirsdóttir and my mother Guðbjörg Petersen for their continuous support and patience.

Contents

Appendices

List of Figures

List of Tables

Chapter 1

Introduction

A number of studies conducted around the Vantajökull Ice cap in Iceland have shown that the crust responds to ongoing retreat of the ice cap. A wide area around the ice cap is rising in response to the reduced ice load in the last century. Deformation has been evaluated from a number of GPS campaigns along the western and southern edge of Vatnajökull ice cap have been conducted since 1992 (e.g. *Sjöberg et al.*, 2004). The most recent study is by *Pagli et al.* (2007). Levelling measurements have also been conducted at lake Langisjór west of Vatnajökull ice cap (*Sigmundsson and Einarsson*, 1992) to study the uplift. These geodetic measurements allow a study of crustal deformation induced by a change in load on the Earth's surface, and have given a valuable insight into the properties of the Icelandic crust.

In 2005, a new study of load induced deformation became possible in the less studied area north of Vatnajökull ice cap. A hydropower plant, Kárahnjúkavirkjun, was constructed in NE Iceland. As a part of that project a major water reservoir, Hálslón, was formed north of Vatnajökull ice cap, slightly east of the plate boundary in North Iceland (Figure 1.1). Three dams were built to confine the Hálslón reservoir. The largest, the Kárahnjúkar-dam, is 198 m high. When full the area of the reservoir is 57 km^2 and it contains 2.4 km^3 of water. The filling began on September 28, 2006 and the reservoir was full in the fall of 2007. As a part of a monitoring and research program (initiated by Landsvirkjun, the National Power Company of Iceland), an extensive network for crustal deformation research was established in 2005. A total of 35 benchmarks were measured in a GPS-campaign in August, 2005 and remeasured in August, 2006 and again in August 2007.

This thesis presents the results of the three GPS campaigns, an evaluation of the ongoing tectonic processes in the area, as well as estimates of the crustal deformation caused by the load of the reservoir.

1.1 Tectonic movements

1.1.1 Plate spreading

Iceland is located on the divergent Mid-Atlantic Ridge (*Einarsson*, 1991a). The plate boundary comes onshore on Reykjanes Peninsula in south-west Iceland and continues to the Hengill triple-junction where it splits up. One branch is the Western Volcanic Zone (WVZ), the other branch is an E-W oriented transform zone, the South Iceland Seismic Zone (SISZ). The SISZ connects to a second branch of the divergent plate boundary, The Eastern Volcanic Zone (EVZ) (Figure 1.1). The divergent plate boundary in northern Iceland, the Northern Volcanic Zone (NVZ), connects to the Tjörnes Fracture Zone (TFZ) near the north coast of Iceland (*Einarsson*, 1991a) (Figure 1.1).

The plate spreading in Iceland can be constrained by a number of techniques. One is REVEL, a global geodetic model for recent plate velocities based on space geodetic data (primarily GPS). It predicts that the full spreading rate in Iceland ranges from 18.9 to 20 mm/y from the Kolbeinsey ridge to the Reykjanes ridge (*Sella et al.*, 2001) (see Figure 1.1). This is in accordance with continuous GPS measurements in Iceland (*Geirsson et al.*, 2006), and it shows good agreement with the NUVEL-1A model (*DeMets et al.*, 1994) derived from geologic data, constraining plate motion over ∼3 Ma.

In south Iceland the spreading rate is divided between WVZ and EVZ. A study by *LaFemina et al.* (2005) indicates that spreading rates across the WVZ increase from 2.6 ± 0.9 mm/yr in the northeast to 7.0 ± 0.4 mm/yr in the southwest. The spreading rate in the EVZ decreases from 19.0 ± 2.0 mm/yr in the northeast to 11.0 ± 0.8 mm/yr in the southwest. Summed extension rates across the two rift zones are approximately equal to the total plate rate, ∼18-20 mm/yr.

1.1.2 Glacio-isostatic adjustments

Temperature records in Iceland that are available since 1846 show a general increase in temperature since 1890 (see overview by *Sigmundsson*, 2006, chapter 8). This is in accordance with the general increase in average global temperature the last 100 y (e.g., *Brohan et al.*, 2006). The changes in average temperature have made an impact on the mass balance of Vatnajökull, the largest ice cap of Iceland covering an area of about 8100 km^2 (*Björnsson et al.*, 2002). The many outlet glaciers of Vatnajökull have generally been retreating since 1890 (*Björnsson*, 1979; *Björnsson et al.*, 2002). The retreat and thinning of the Vatnajökull ice cap during last century results in crustal rebound under the ice cap and in the

surrounding area. GPS campaign measurements south of Vatnajökull in 1996, 2002, 2003 and 2004 show uplift (*Pagli et al.*, 2007), where the highest uplift rate is measured at station Jökulheimar (JOKU) with average velocity of 25 mm/yr (*Pagli et al.*, 2007). The continuous GPS stations SKRO, HOFN and ISAK, which are a part of the continuous GPS network in Iceland (ISGPS), also show present uplift in the area around the ice cap (*Geirsson et al.*, 2006).

The opserved uplift around Vatnajökull can be atributed to the current retreat

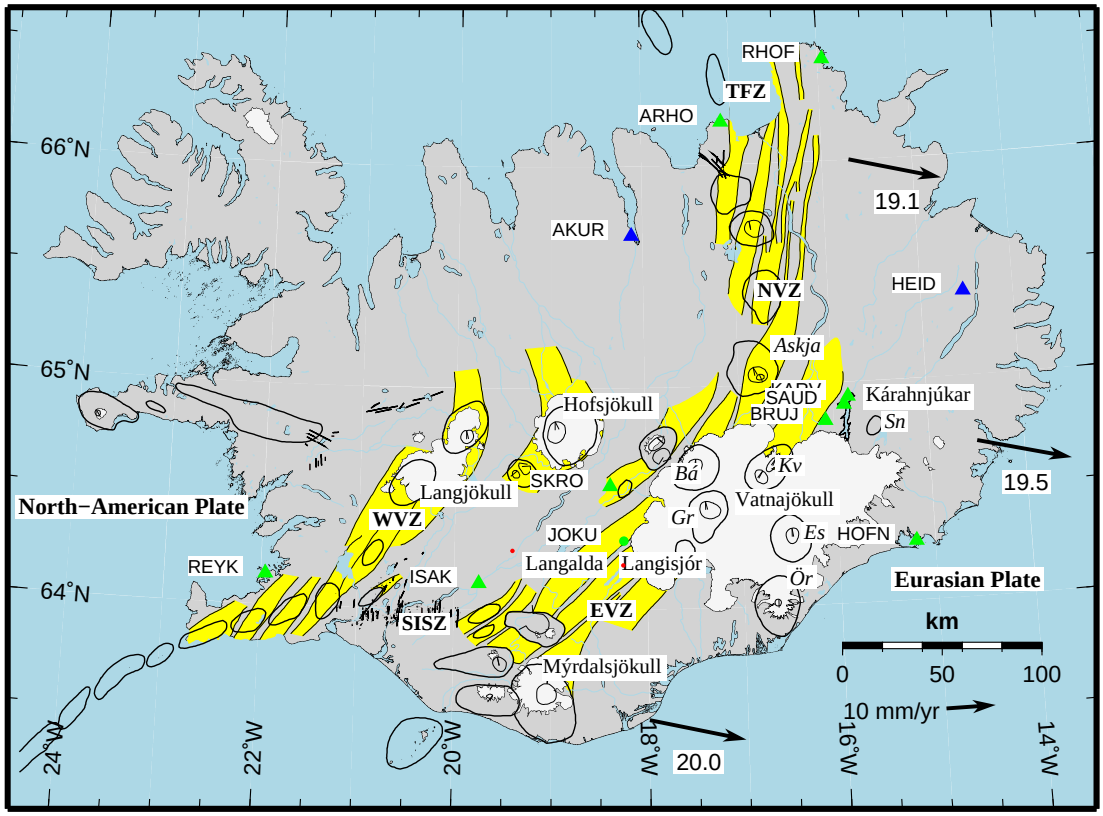

Figure 1.1: Tectonic overview of Iceland. The plate boundary between the North-Amercian Plate and the Eurasian Plate. The active volcanic systems consists of fissure swarms (shown in yellow), central volcanoes (thick oval outlines), and calderas at some of the volcanoes (thin oval outlines) (*Einarsson and Sæmundsson*, 1987). The Northern Volcanic Zone (NVZ) is located north of the Vatnajökull ice cap. In the south the plate boundary divides up into the Western Volcanic Zone (WVZ) and the Eastern Volcanic Zone (EVZ). The South Iceland Seismic Zone (SISZ) and Tjörnes Fracture Zone (TFZ) are transform zones. The labled volcanc systems are: Askja, Bárðarbunga (Bá), Esjufjöll (Es), Grímsvötn (Gr), Kverkfjöll (Kv), Snæfell (Sn) and Öræfajökull (Ör). The green triangles are continuous GPS stations run by the Iclandic Meteorological Office. The blue triangles are continuous GPS stations run by the National Land Survey of Iceland. The GPS station JOKU (green dot) is showing high uplift rates. The Kárahnjúkar area is north of Vatnajökull ice cap. The arrows show the full spreading rate over Iceland as predicted by *Sella et al.* (2001).

of the ice cap. Model calculations suggest that the GPS observations at the southern edge of Vatnajökull are consistent with an elastic plate thickness of 10-20 km and viscosity of $4 - 10 \times 10^{18}$ Pa s in the underlying material (*Pagli et al.*, 2007). A large scale uplift rates of ∼1 cm/yr over a large part of central and southeastern Iceland have been detected from the ISNET GPS campaigns in 1993 and 2004. The cause of these uplift rates are not fully understood but a finite element modelling of glacio-isostatic adjustments due to the thinnig of Iceland's four biggest ice caps: Vatnajökull, Hofsjökull, Langjökull and Mýrdalsjökull, assuming a viscosity of 8×10^{18} Pa s below a 10 km thick elastic plate could explain the broad area of high uplift rates (*Árnadóttir et al.*, 2007). An earlier study of current tilting of lake Langisjór, inferred from repeated levelling, suggested a viscosity under Iceland of $1 \times 10^{18} - 5 \times 10^{19}$ Pa s (*Sigmundsson and Einarsson*, 1992). Rapid glacio-isostatic adjustment at the Pleistocene-Holocene boundary associated with Iceland at that time has also been used to estimate viscosity. A maximum value of 1×10^{19} Pa s was inferred from these studies (*Sigmundsson*, 1991).

In addition to the high uplift rates related to the thinning of ice caps, a seasonal variation is observed in the ISGPS time series. *Grapenthin et al.* (2006) modelled the elastic response to the annual snow load on Iceland's four largest ice caps and showed that the observed signal in the ISGPS time series were consistent with the predicted signal.

1.2 Geological setting

1.2.1 Volcanic systems

Three volcanic systems are in the vicinity of Kárahnjúkar. The Askja volcanic system which is the most active system, the Kverkfjöll volcanic system and Snæfell. Askja and Kverkfjöll are a part of the divergent plate boundary, but Snæfell is at the northern end of a flank zone which includes the Esjufjöll and Öræfajökull volcanic systems. In addition, the volcanic systems Grímsvötn and Bárðarbunga are present within Vatnajökull ice cap, but they are more then 100 km away from Kárhanjúkar. These volcanic systems along with Askja are discussed in an overview of magma movements of active volcanoes in Iceland by *Sturkell et al.* (2006a)

The Askja central volcano is located on the plate boundary in the Northern Volcanic Zone 60-70 km west of Kárahnjúkar. The Askja volcanic system consists of three caldera structures (the largest is 8 km in diameter), an active geothermal

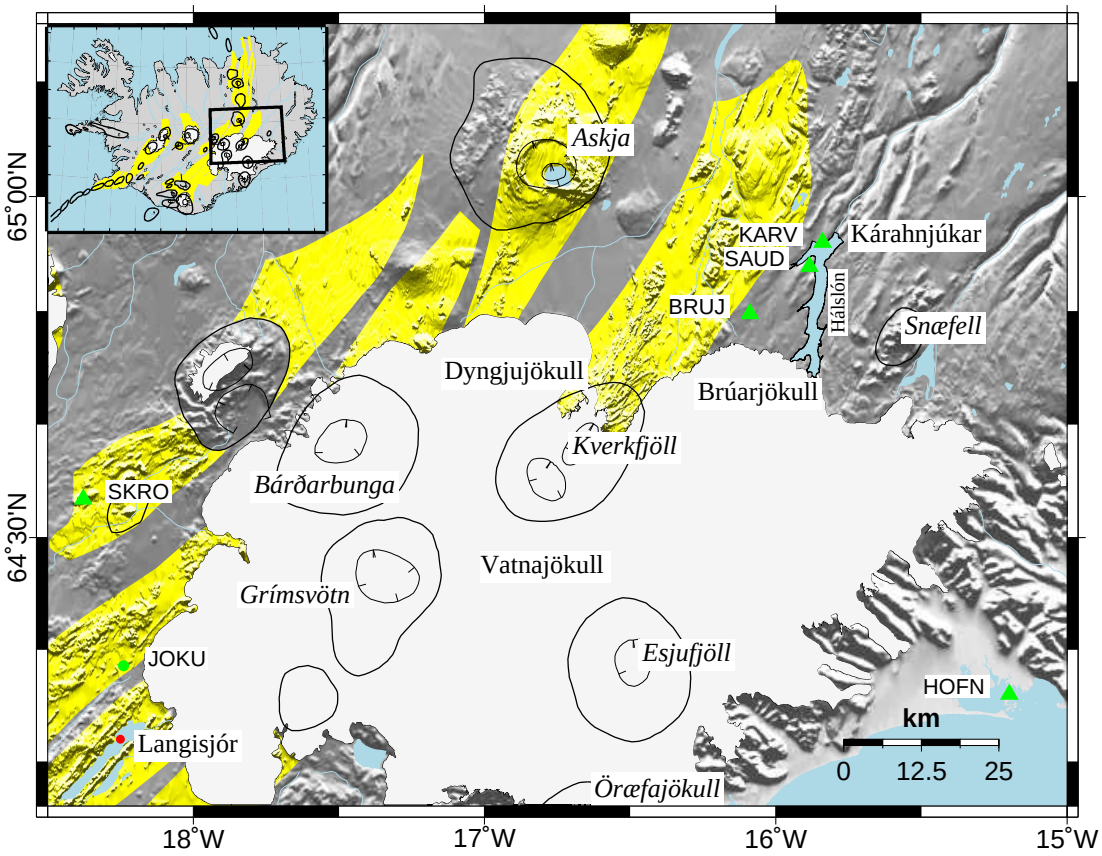

Figure 1.2: Study area in relation to volcanic systems and the Vatnajökull ice cap. Lake Langisjór is west of Vatnajökull ice cap. The outlet glaciers Dyngjujökull and Brúarjökull surrounding Kverkfjöll central volcano. The labled volcanic systems and there fissure swarm: Askja, Bárðarbunga, Esjufjöll, Grímsvötn, Kverkfjöll, Snæfell and Öræfajökull (*Einarsson and Sæmundsson*, 1987)

system and fissure swarms (*Sigvaldason*, 2002). The last rifting episode in Askja occurred in 1874-1875 (*Sigurdsson and Sparks*, 1978). The most resent eruption was in 1961 (*Thorarinsson and Sigvaldason*, 1962). A current deflation of Askja has been ongoing since 1973 (*Sturkell et al.*, 2006b).

The center of Kverkfjöll volcanic system is located between the Dyngjujökull and Brúarjökull outlet glaciers and is a part of the plate boundary in the NVZ. It's subglacial central volcano is located around 50 km south-sest of Kárahnjúkar but the northern part of the fissure swarm reaches to around 5 km from the westernmost part of the Hálslón reservoir (Figure 1.2). The orientation of the fault system underlying Hálslón (Figure 1.3) might suggest that it is a part of the Kverkföll fissure swarm. *Höskuldsson et al.* (2006) observed basalt pillows formed during six different subglacial fissure eruptions in the fissure swarm associated with the Kverkfjöll volcanic centre, during the last major glaciation period in Iceland. The latest observation of eruption connected to Kverkfjöll volcanic center are reported by *Sæmundsson and Jóhannesson* (2005) who suggest that

Lindahraun lava in Krepputunga, probably dates from about A.D. 1200.

Snæfell volcano is located about 15-20 km south-east of Kárahnjúkar. It is located at the northern end of a volcanic flank zone. Volcanic activity at Snæfell is indicated within the last 0.7-0.8 Ma and it is currently thought to be inactive (*Hards et al.*, 2000).

1.2.2 Hálslón Reservoir

When full, Hálslón contains 2.4 km^3 of water. Early evaluations estimated the load to cause eventual total crustal subsidence up to about 30 cm (*Sigmundsson*, 2002). Elastic response was expected to occur in a relatively short period and account for about half of the subsidence, but be localised mostly close to the reservoir. In ten years, depending on the viscosity, it was estimated that a fraction of the subsidence would have occurred within an area of about 50 km around Hálslón. It was estimated that initially the velocity of the subsidence could be around 1 cm/yr.

Geological observations made during the construction time led to the discovery of a fault system underlying the area with evidence of Holocene activity in some cases (*Sæmundsson and Jóhannesson*, 2005; *Guðmundsson and Helgason*, 2004; *Sigmundsson et al.*, 2005). Some of the most notable observations are evidence of Holocene slip on the Sauðárdalur fault and a fault at the base of the Desjarárdalur Dam (*Sæmundsson and Jóhannesson*, 2005). A system of faults underlies the Kárahnjúkar dam, but evidence for Holocene slip on them is inconclusive (Figure 1.3).

Earthquake triggering associated with reservoirs like Hálslón are well known. The increased pore pressure modifies the stress state of the surroundings and reduces the friction on fault planes, causing slip on faults in high state of stress. An overview on studies of triggered earthquakes by artificial water reservoirs is given by *Gupta* (2002). Aseismic movements on faults can also be expected. Such movement on fractures occurred at the Langalda dam in 1971 in the Tungná area in S-Iceland (*Tómasson*, 1976). In that case, a 8 m deep test reservoir with 1.5 km^2 area was drained through a fracture that opened up at the bottom. It was concluded that the condition that allowed this to happen was a low horizontal compressive stress normal to the faults compared to the water pressure and a low groundwater level, some tens of meters below the surface (*Tómasson*, 1976). A similar behaviour was observed during eruptions of Krafla volcano at the divergent plate boundary in N-Iceland when lava flowed into fissures and opened them up as the fluid pressure in them rose due to the weight of the fluid lava (*Einarsson*, 1991b).

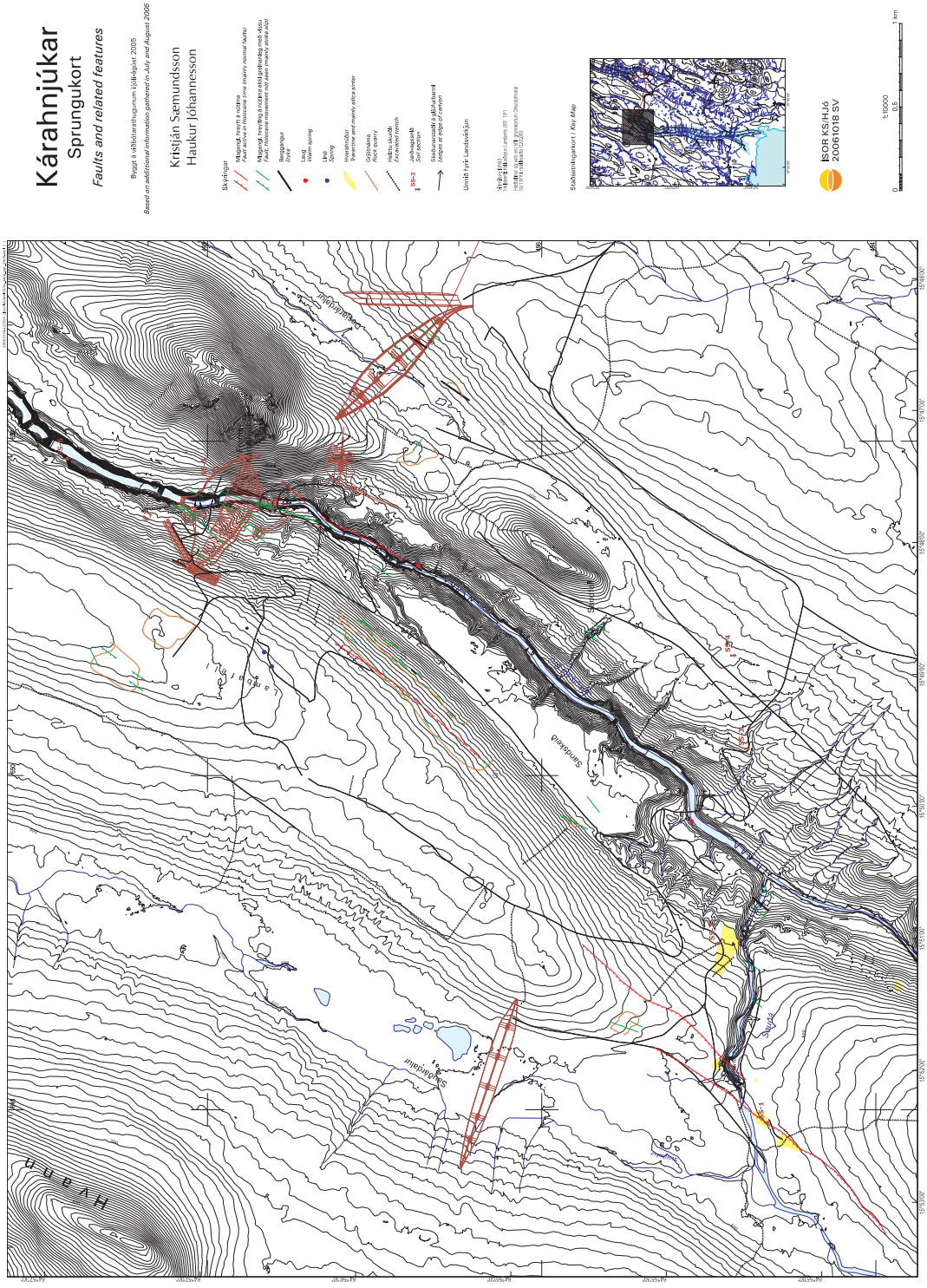

Figure 1.3: Faults discovered during the construction time at the Kárahnjúkar area. The most notable observations are evidence of Holocene slip on the Sauðárdalur fault (see the fault system that crosses a river marked Sauðá (lower left part of figure, shown in red), and fault systems underlying the Desjár-dam and Kárahnjúkar-dam (no Holocene slip detected). Detailed description is found in (*Sæmundsson and Jóhannesson*, 2005).

Printed with permission of Kristján Sæmundsson

Chapter 2

Data

2.1 The Kárahnjúkar GPS network

The Kárahnjúkar GPS network consists of 35 benchmarks in the vicinity of Hálslón. Most of the stations were installed and observed in August, 2005. In addition benchmarks located along the Kverkfjöll fissure swarm where included in the network (see Figures 2.1 and 2.2). The data from these campaign measurements are analysed together with data from a number of continuous GPS stations (CGPS). Included in the processing were the CGPS stations REYK, HOFN, ISAK, SKRO, RHOF, AKUR, ARHO, BRUJ, KARV, SAUD and HEID (Figure 1.1) as well as the IGS stations ALGO, ALRT, ONSA, TROM, MADR and WES2 (REYK and HOFN are also IGS stations) (Figure 2.3). The Kárhnjúkar GPS campaigns took place in August 2005, August 2006 and August 2007. By conducting the measurements at the same time each year (August), the effect of seasonal variations should be minimised. A summary of the 2005 and 2006 GPS campaigns is presented in *Ófeigsson et al.* (2006b, 2007b). Each GPS station was occupied for one whole session (24 hours) and for a part of two session (8-16 hours), giving a set of three coordinate values for each campaign. Appendix A.1.

2.1.1 Continuous GPS measurements

In order to resolve temporal changes in the Hálslón area in real time and monitor seasonal variations, three continuously measuring GPS stations were installed in the area by the Icelandic Meteorological Office (Figure 2.1). Station SAUD located at Sauðárháls was installed in October 30, 2004. Station KARV located near the camps at Kárahnjúkar was installed in September 17, 2005. Station BRUJ located near Brúarjökull was installed on September 16, 2005. Detailed

information about the continuous GPS sites can be found on the website of the Icelandic Meteorological Office (*Geirsson*, 2008). In addition, a continuous GPS station was installed in Heiðarsel (HEID) and run by the National Land Survey of Iceland (see e.g. Table A.1). Additional 4 continuously running GPS stations where installed on HAHV, KARA, BALD and DSTI in October 2006 and are maintained by Hnit Consulting Engineers and the Engineering Research Institute of the University of Iceland. These stations are included in the processing but the full resolution of the temporal behaviour is not explored.

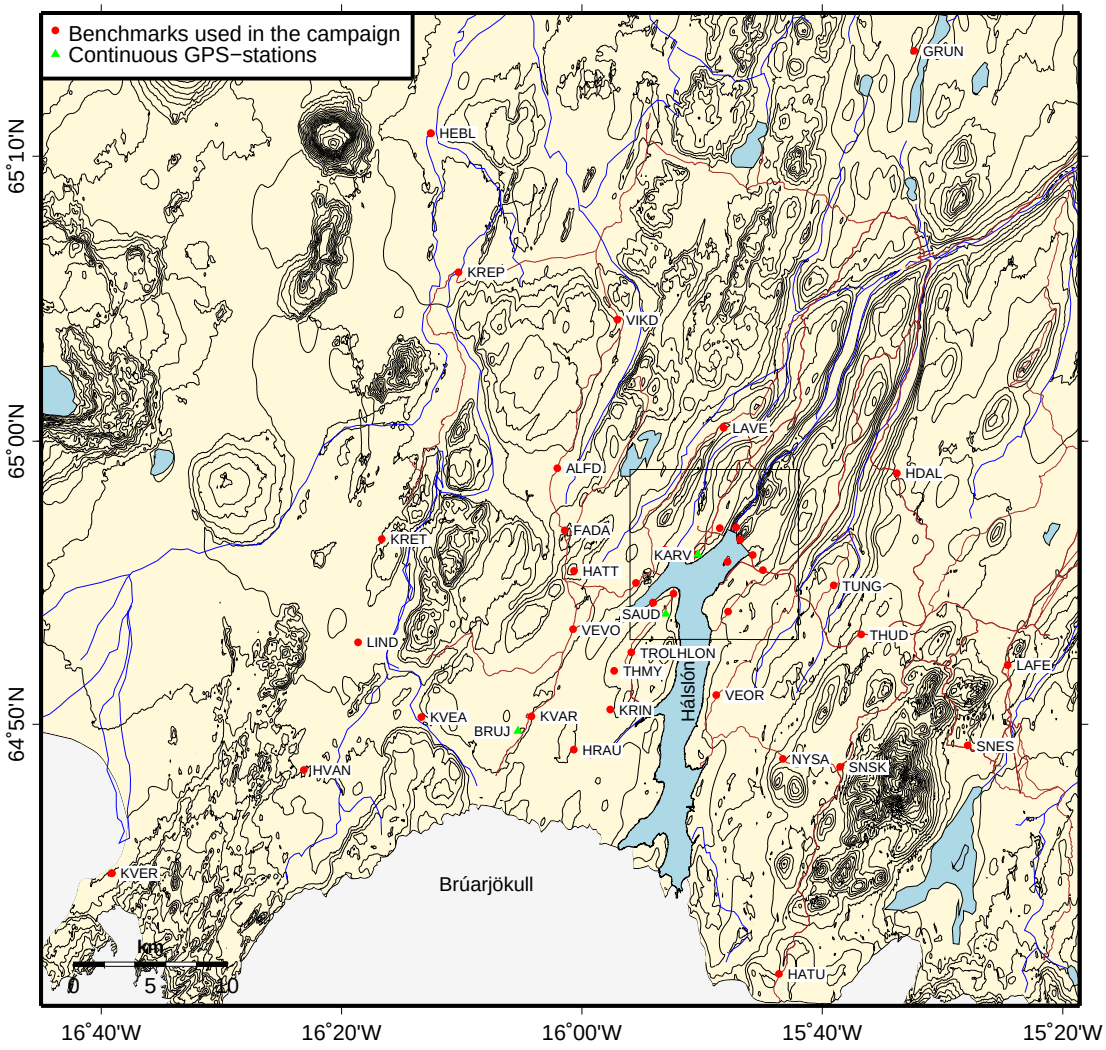

Figure 2.1: Benchmarks measured in the Kárahnjúkar 2005, 2006 and 2007 GPS campaigns. The figure shows all the benchmarks measured in the campaigns except station GRUN (see appendix A.1 for coordinates). It is located to the north of the map. The figure shows also the location of Hálslón when filled to elevation of 625 m above sea level. The box shows coverage of Figure 2.2. (see Appendix A.1 for coordinates).

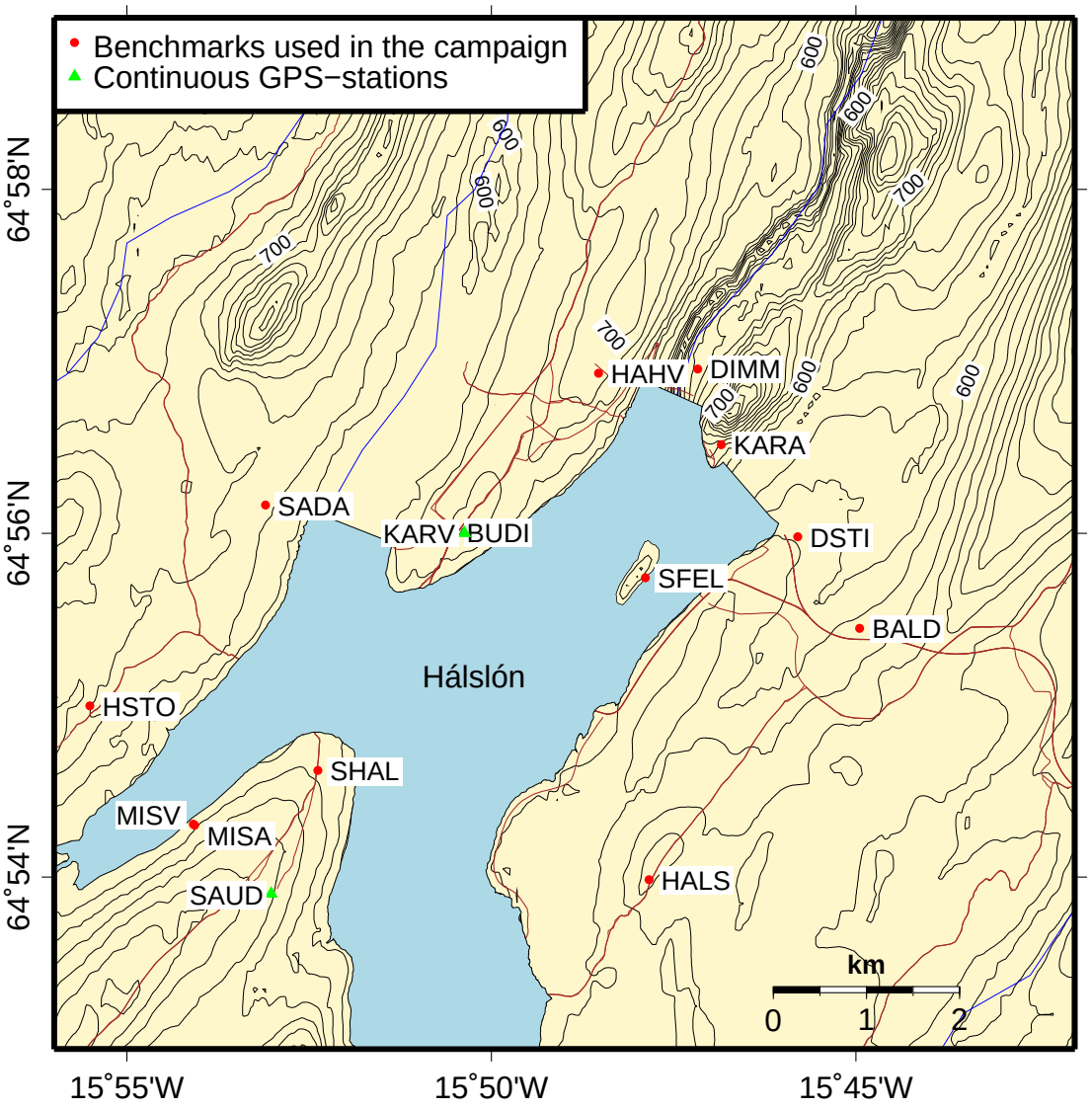

Figure 2.2: GPS Benchmarks close to dams in the Kárahnjúkar area, occupied in the 2005, 2006 and 2007 GPS campaigns. The figure shows Hálslón at an elevation of 625 m above sea level. (see appendix A.1 for coordinates).

2.2 Data Processing

2.2.1 Coordinate estimation

The processing of the GPS data was done using the software Bernese version 5.0, following a double-difference processing procedure described by *Dach et al.* (2007). In short the analysis is based on a double-difference processing where L1&L2 ambiguities are resolved (for baselines up to 2000 km long) using quasi-ionosphere-free (QIF) resolution strategy. The final network solution is a minimum constraint solution, realised by no-net-translation conditions imposed on a set of IGS05 reference coordinates. The IGS stations used to define the reference

frame are REYK, HOFN, ALGO, ALRT, ONSA, TROM, MADR and WES2 (Figure 2.3). The coordinate estimation is based on 24 hour sessions, estimating the average coordinates of each session.

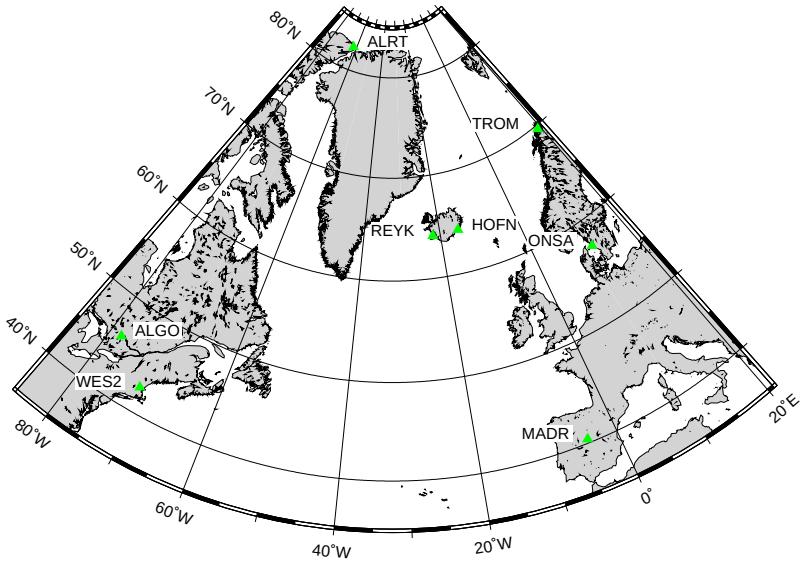

Figure 2.3: The location of the IGS stations used for constraining the reference frame.

The following description of the GPS data processing steps of the coordinate esitimation follows closly the description from *Dach et al.* (2007) Chapter 20.4.2. The first step prepares the pole information, the precise orbit files and satellite clock correction for the processing. The second step converts the observation data into Bernese format synchronising the receiver clocks to GPS time. Here, observation files with significant gaps and stations showing a large rms value, will automatically be removed from the processing.

The third step makes up the preprocessing part. First, phase single-difference observation files are created using OBS-MAX strategy to select the baselines. This strategy selects from all possible combinations of baselines, a set of baselines with maximum common observations is chosen. The phase single-difference observation files are then preprocessed, cycle slips are detected and corrected or new ambiguity is set up if the size of a cycle slip cannot reliably be determined. Then unpaired observations (i.e., only L1 or L2 at an epoch) and observations gathered at very low elevation angles are flagged as unusable. Large rms values, larger than 20 mm and/or baseline corrections much larger than 0.5 m, or lot of ambiguities may indicate a data problem. Next, a double-difference phase residual screening is performed (using L3 band) by creating a residual file which is screened for outliers and marked, then a new cleaned residual file and normal equation file is created using L3 band. Finally the statistics of the screening process is used to detect bad stations (containing overall rms error of more the 6 mm)

and remove them (only one at a time). These preprocessing steps are repeated until no bad stations are detected.

The fourth step resolves the phase ambiguities. Real valued ambiguities are computed based on normal equations stored in the residual screening preprocessing. Coordinates and troposphere estimates are saved. A posteriori rms error should be not higher than about 1.4 mm after this step. Baselines less then 2000 km are selected. Troposphere estimates and coordinates from the float solution in the previous step are introduced, then L1&L2 integer ambiguities are resolved simultaneously using the QIF strategy for each baseline separately. On average over 90% of the ambiguities are resolved.

The fifth step, as descriped in *Dach et al.* (2007) Chapter 20.4.2, estimates the final network-solution. An ambiguity fixed solution is computed and normal equation information is stored. Estimated parameters include station coordinates, zenith path delays, and horizontal tropospheric gradients *Dach et al.* (2007) Chapter 11.4.3. This is a free network solution where coordinates are estimated without any constraints. The normal equations, containing the free network solution, are used to compute the final solution. Then the final solution is a minimum constraint solution using no-net-translation conditions imposed on a set of fiducial (reference) sites (IGS05 reference coordinates). The coordinates of all involved fiducial stations are subsequently verified by means of a 3-parameter Helmert transformation. The three translation components should be zero, the residuals below 1 cm of the reference sites are rejected and the constrained solution is computed again until all reference sites meet the criteria. SINEX file is created to allow for both reconstruction of the unconstrained, free network solution and for straightforward extraction of station coordinates of the originally computed minimum-constraint solution (*Dach et al.*, 2007, Chapter 20.4.2).

The IGS05 reference coordinates are realisation of the ITRF2005 reference frame (*Altamimi et al.*, 2007). ITRF is a geocentric, Cartesian, global, reference frame constructed from combined station positions and velocities estimated from a number of space geodesy techniques: Very Long Baseline Interferometry (VLBI), Satellite Laser Ranging (SLR), Global Positioning System (GPS) and Doppler Orbitography Radiopositioning Integrated by Satellite (DORIS). It's origin is at (close to) Earth's centre of mass (geocentric), the Z-axis is the direction to the pole and the scale is SI (meters). It's orientation was initially given by the Bureau International de l'Heure (BIH) orientation at 1984.0. The time evolution is determined by using no-net-rotation condition with regards to horizontal tectonic motions over the whole Earth (*McCarthy and Petit*, 2004).

2.2.2 Uncertainties

The formal covariance matrix of the coordinates estimated by Bernese does not take into account all sources of systematic errors or mismodelled parameters and tends therefore to be overly optimistic of the true coordinate uncertainty. In order to derive a better estimate of the "true" uncertainties, a similar method as presented by *Geirsson* (2003) was used. The weighted standard deviation or repeatability can be estimated by

$$R = \left(\frac{N}{N-1} \frac{\sum_{i=1}^{N} \left(\frac{y_i - \widehat{y}_i}{\sigma_i^y} \right)^2}{\sum_{i=1}^{N} \left(\frac{1}{\sigma_i^y} \right)^2} \right)^{\frac{1}{2}} \tag{2.1}$$

where N is the number of sessions (session=1 day), y_i is the coordinate value for session i, $\widehat{y}_i$ is the weighted mean of the daily coordinate solutions and σ_i^y is the formal error estimate from the Bernese solution (*Geirsson*, 2003). To get a good estimate of the true errors from weighted repeatability a number of sessions is needed. Only three sessions are too small sample for a good estimate. The continuous GPS stations are included in the analysis of the campaign data and they processed for a few sessions before and after the campaigns. Therefore, coordinates of the CGPS stations are estimated for at least 10 consecutive sessions which gives better statistics. The CGPS stations are then used to estimate an average scaling factor to scale the formal error estimates with. The repeatability (R see equation 2.1) of the CGPS station coordinates are used to derive a scaling factor

$$s_j = \frac{R}{\sigma_{mj}^y} \tag{2.2}$$

for the formal error estimate of Bernese. Here j is an index for each station. The σ_{mj}^y is the mean of the σ_i^y. The average scaling factor (s) for all the CGPS station available is then used as a scaling factor for all the campaign GPS stations. The scaling factor obtained by this method was: (east,north,up)=(5,4,4). This implies that the formal errors in the coordinate are underestimated by a factor of $\sim$5.

2.2.3 Velocity estimation

Velocities were estimated from the time series of displacements using weighted least squares method (e.g. *Dach et al.*, 2007) to estimate the best linear fit to the time evolution of coordinate components of the data along with the associated uncertainties. For each displacement component, y_i (where y_i can be the east, north or up component) it is assumed that y_i is a linear function of time (t_i),

written

$$\widehat{y}_i = y_i + \varepsilon_i = vt_i + b \tag{2.3}$$

where v and b are unknown parameters to be determent, $\widehat{y}_i$ the estimated displacement and $\varepsilon_i = y_i - \widehat{y}_i$ is the residual. To solve for v and b, at least, to independent observations are needed. The vector form of equation 2.3 can be written as

$$\widehat{\mathbf{y}} = A\mathbf{p}, \tag{2.4}$$

where $\mathbf{p} = \begin{pmatrix} a & b \end{pmatrix}^T$ forms the vector of unknowns, $\widehat{\mathbf{y}} = \begin{pmatrix} \widehat{y}_1 & \cdots & \widehat{y}_N \end{pmatrix}^T$ is the estimated displacements ("best" line for the data set $\mathbf{y} = \begin{pmatrix} y_1 & \cdots & y_N \end{pmatrix}^T$) for N number of observations and

$$A = \begin{pmatrix} t_1 & 1 \\ t_2 & 1 \\ \vdots & \vdots \\ t_N & 1 \end{pmatrix}. \tag{2.5}$$

is the matrix of coefficients. If individual sessions are independent of each other, the weight matrix is formed from the scaled uncertainties (estimated as described in Section 2.2.2) of the observations y_i and the diagonal matrix of the inverse square of the uncertainties σ_i^y becomes

$$\Lambda = \begin{pmatrix} \frac{1}{(\sigma_1^y)^2} & 0 & \cdots & 0 \\ 0 & \frac{1}{(\sigma_2^y)^2} & & 0 \\ \vdots & & \ddots & 0 \\ 0 & \cdots & 0 & \frac{1}{(\sigma_n^y)^2} \end{pmatrix} \tag{2.6}$$

Dach et al. (2007) gives overview of basic theory of Least-Squares Estimation using the Gauss-Markoff modelling. According to Gauss-Markoff the model, the vector of unknowns then becomes

$$\widehat{\mathbf{p}} = (A^T \Lambda A)^{-1} \Lambda^T P \mathbf{y} \tag{2.7}$$

Where the estimated velocity is v. The covariance matrix, D, is given as

$$D(\widehat{\mathbf{p}}) = \widehat{\sigma}^2 (\Lambda^T P A)^{-1} \tag{2.8}$$

The variance of unit weight, $\widehat{\sigma}^2$, is given as

$$\widehat{\sigma}^2 = \frac{(\mathbf{y} - \widehat{\mathbf{y}})^T \Lambda (\mathbf{y} - \widehat{\mathbf{y}})}{N - 2} = \frac{1}{N-2} \sum_{i=1}^{N} \frac{(y_i - \widehat{y}_i)^2}{(\sigma_i^y)^2}. \tag{2.9}$$

The 2 in $N-2$ is the number of unknowns. The variance of the velocity is the element $(D(\widehat{\mathbf{p}}))_{11}$ of the covariance matrix (equation 2.8). Writing out the equation for the covariance of the velocity gives

$$\sigma_v^2 = \frac{\widehat{\sigma}^2}{\sum_{i=1}^{N}\left(\frac{t_i}{\sigma_i}\right)^2 - \left(\sum_{i=1}^{N}\frac{t_i}{(\sigma_i^y)^2}\right)^2 / \sum_{i=1}^{N}\frac{1}{(\sigma_i^y)^2}}. \tag{2.10}$$

This procedure derived from *Dach et al.* (2007) is also very similar to the procedure used by *Geirsson* (2003).

Chapter 3

Velocity fields

3.1 Horizontal velocities

Figures 3.1-3.6 show the horizontal velocity fields derived from the three GPS campaigns in the ITRF2005 reference system (the velocities are also given in Tables A.4-A.9). The velocities of the GPS stations are derived as described in Section 2.2.3. The velocities are obtained in the reference system of the coordinates, ITRF2005, (see Section 2.2.1) and therefore they include the time evolution of the reference system as well as tectonic movements such as the plate movements. The figures are derived from a different subsets of GPS campaigns. The 2005-2006 velocity field, spanning the interval before the filling of Hálslón began, is shown in Figures 3.1 and 3.2. The velocity field between 2006-2007 which is the interval during the filling of Hálslón is shown in Figures 3.3 and 3.4. Some changes in velocities occur relative to the former interval. Comparison of the two intervals is then used to estimate the deformation related to the filling process. The average velocity field over the whole interval 2005-2007 is then shown in Figures 3.3 and 3.4. The average velocities over the whole period 2005-2007 may give a better estimation of stable background processes far away from Hálslón, such as plate movements and glacial icostacy signals because it contains more data of the longer time series. Averaging over the whole period, 2005-2007 may on the other hand average out velocities that are not constant in time.

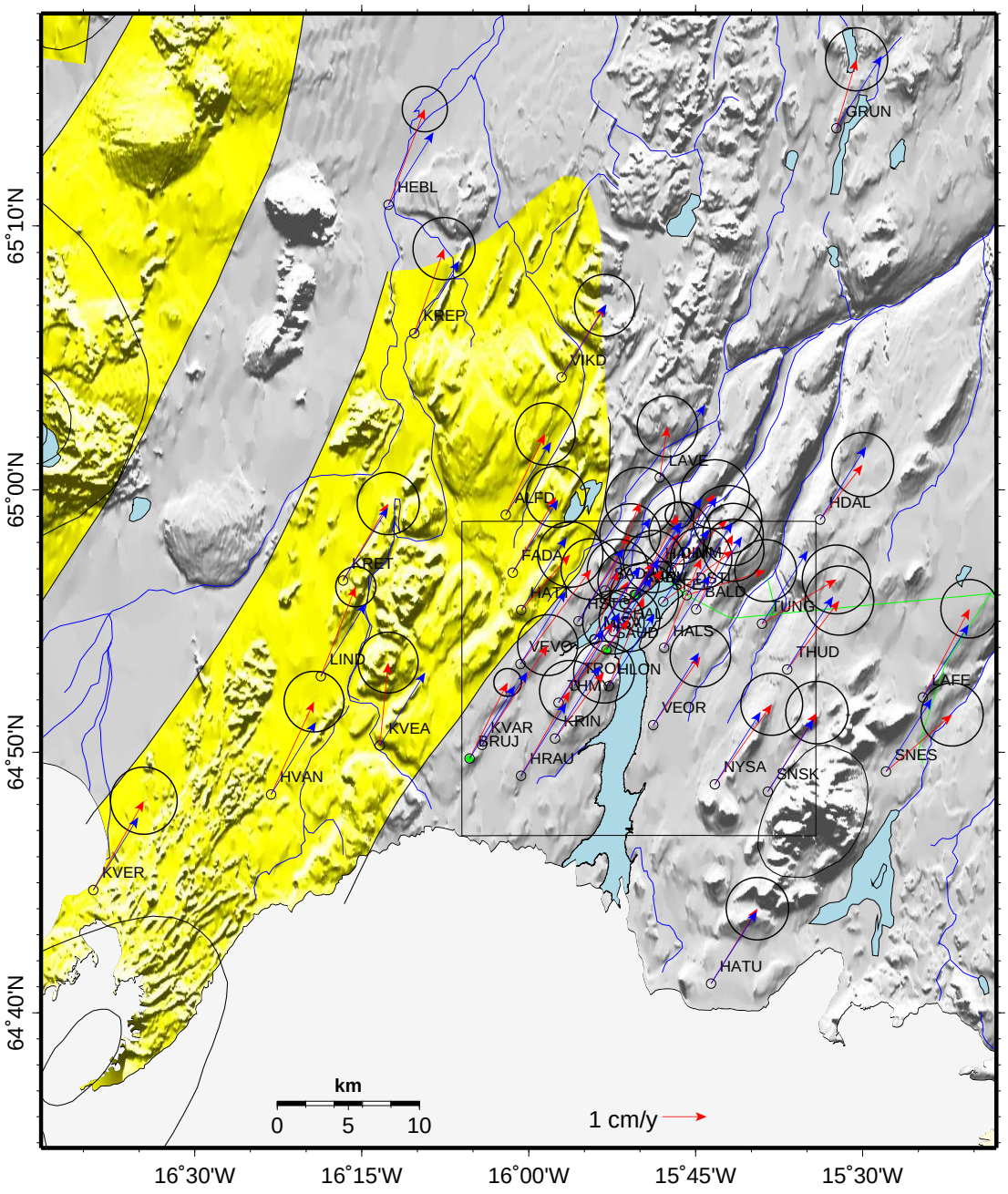

Figure 3.1: Horizontal velocities calculated from measurements in August 2005 and August 2006 in the ITRF2005 reference frame (red arrows). Also shown are the predicted velocities of the NNR-NUVEL1A model (blue arrows) for the Eurasian Plate. The ellipses show the 95% confidence interval. The box shows the coverage of Figure 3.2. The estimated velocities are also shown in Table A.4.

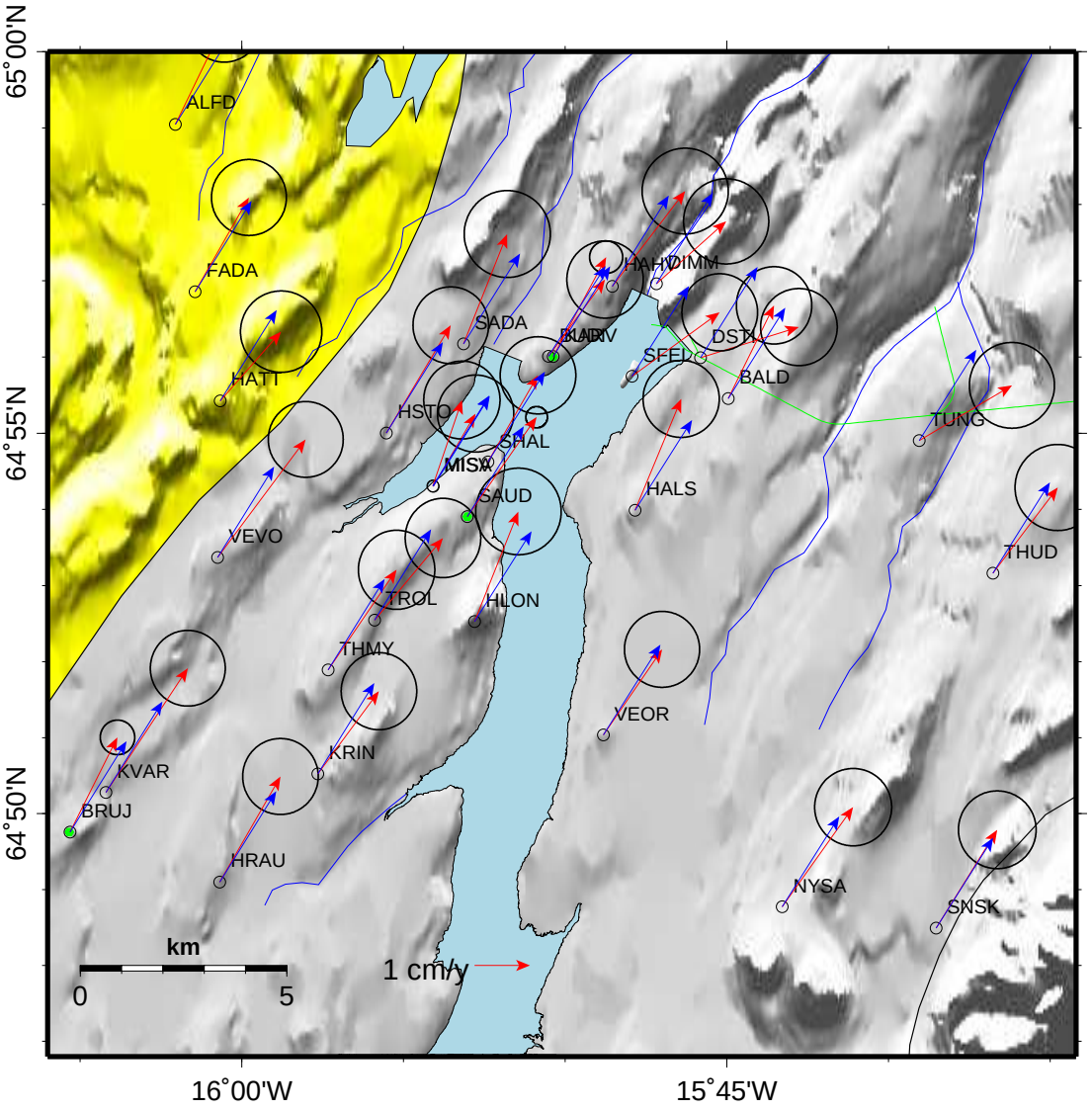

Figure 3.2: Horizontal velocities calculated from measurements in August 2005 and August 2006 in the ITRF2005 reference frame (red arrows). Also shown are the predicted velocities of the NNR-NUVEL1A model (blue arrows) for the Eurasian Plate. The ellipses show the 95% confidence interval. The green line shows the tunnel that leads the water from the reservoir to the power plant. The figure shows the area inside the box in Figure 3.1. The estimated velocities are also shown in Table A.4.

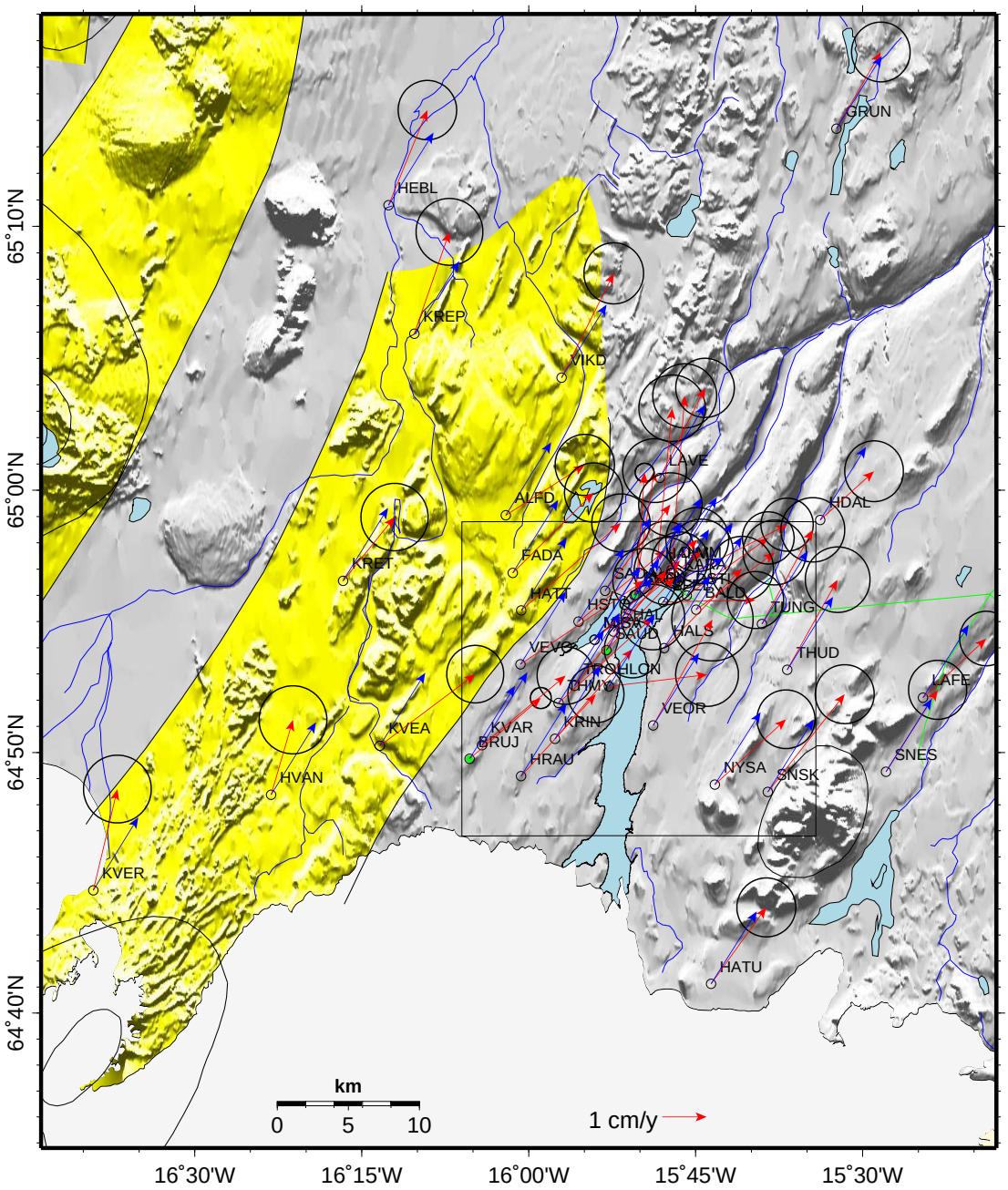

Figure 3.3: Horizontal velocities calculated from measurements in August 2006 and August 2007 in the ITRF2005 reference frame (red arrows). Also shown are the predicted velocities of the NNR-NUVEL1A model (blue arrows) for the Eurasian Plate. The ellipses show the 95% confidence interval. The green line shows the tunnel that leads the water from the reservoir to the power plant. The box shows the coverage of Figure 3.4. The estimated velocities are also shown in Table A.6.

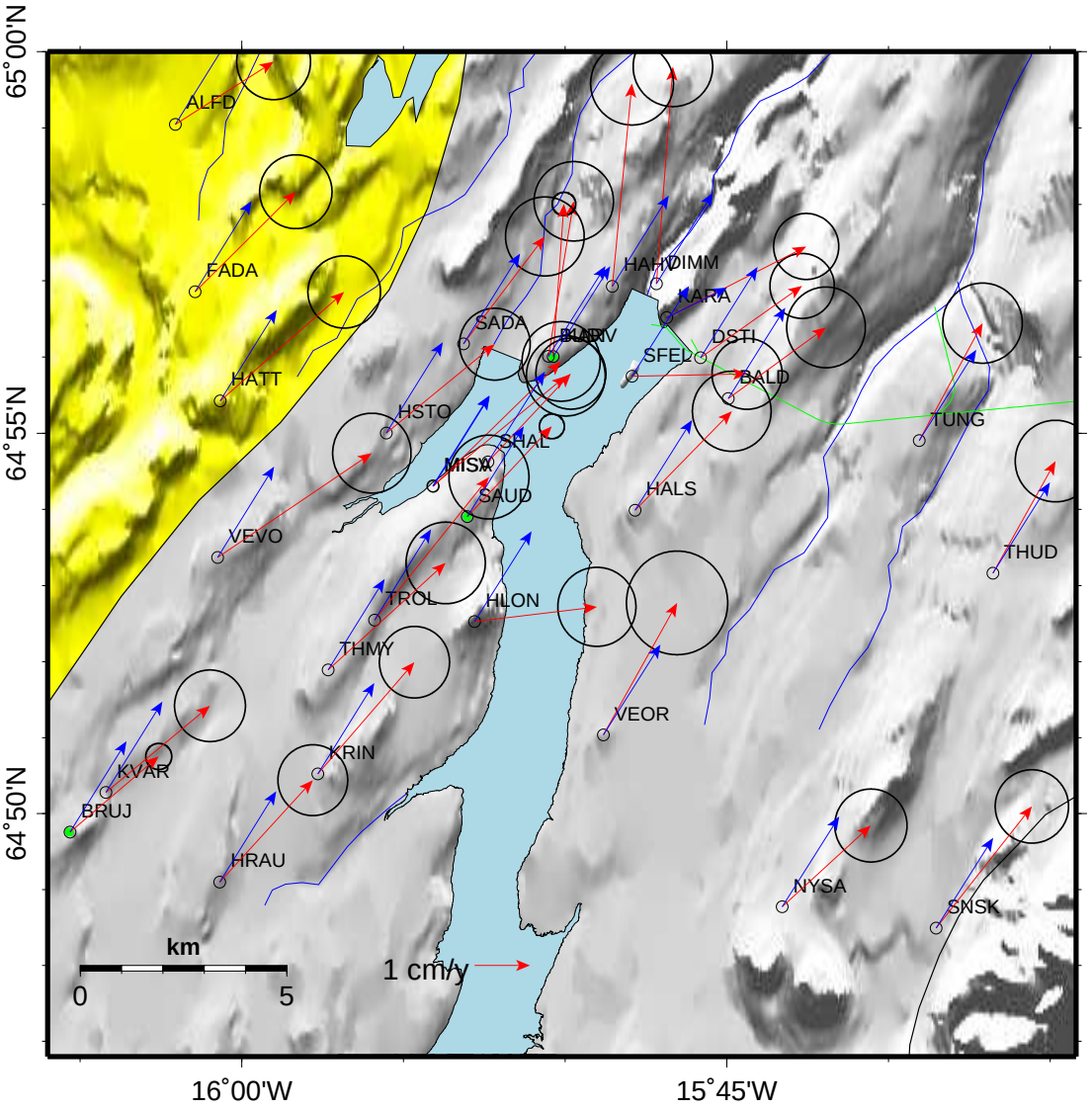

Figure 3.4: Horizontal velocities calculated from measurements in August 2006 and August 2007 in the ITRF2005 reference frame (red arrows). Also shown are the predicted velocities of the NNR-NUVEL1A model (blue arrows) for the Eurasian Plate. The ellipses show the 95% confidence interval. The green line shows the tunnel that leads the water from the reservoir to the power plant. The figure shows the area inside the box in Figure 3.3. The estimated velocities are also shown in Table A.6.

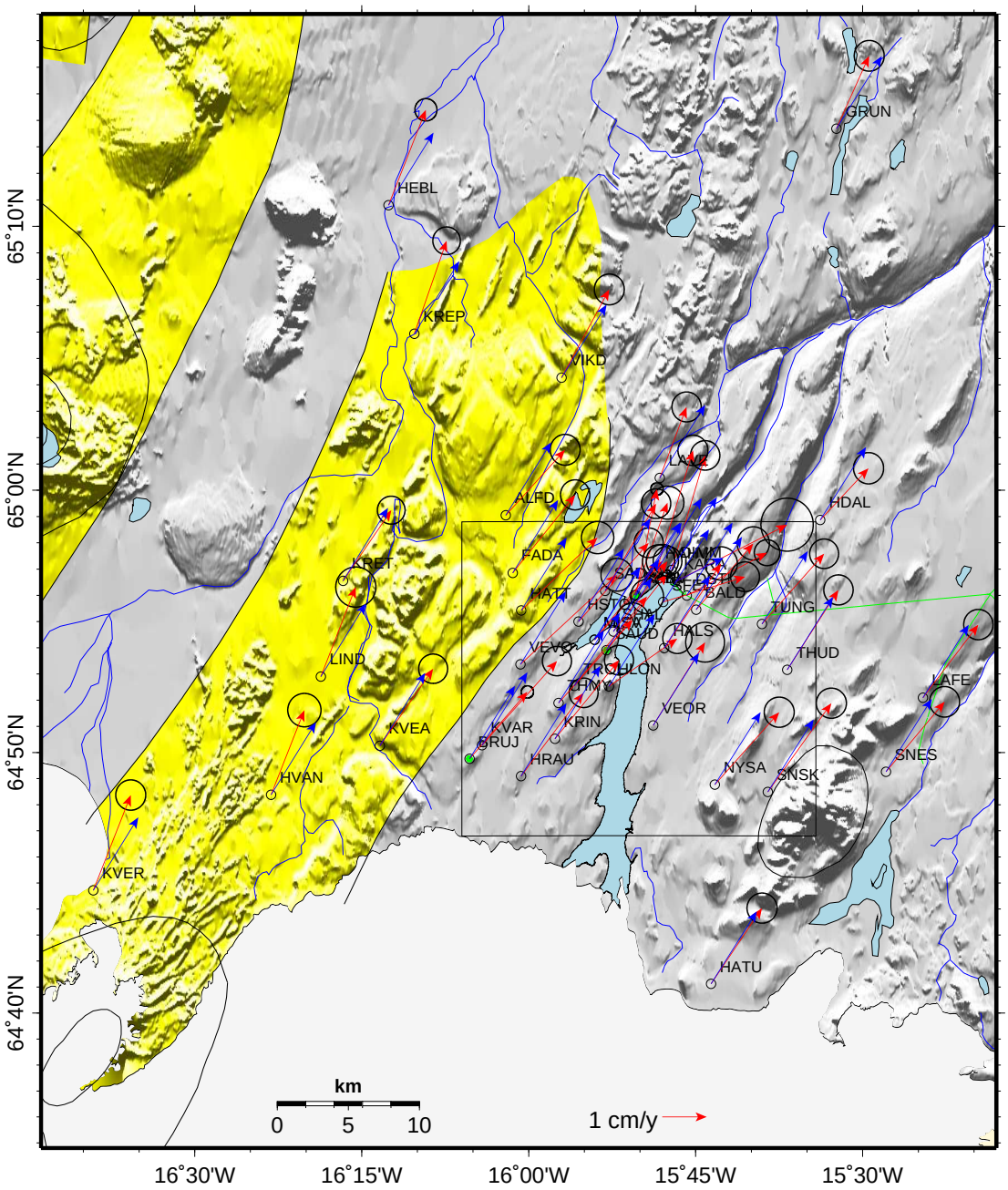

Figure 3.5: Horizontal velocities calculated from measurements in August 2005, August 2006 and August 2007 in the ITRF2005 reference frame (red arrows). Also shown are the predicted velocities of the NNR-NUVEL1A model (blue arrows) for the Eurasian Plate. The ellipses show the 95% confidence interval. The green line shows the tunnel that leads the water from the reservoir to the power plant. The box shows the coverage of Figure 3.6. The estimated velocities are also shown in Table A.8.

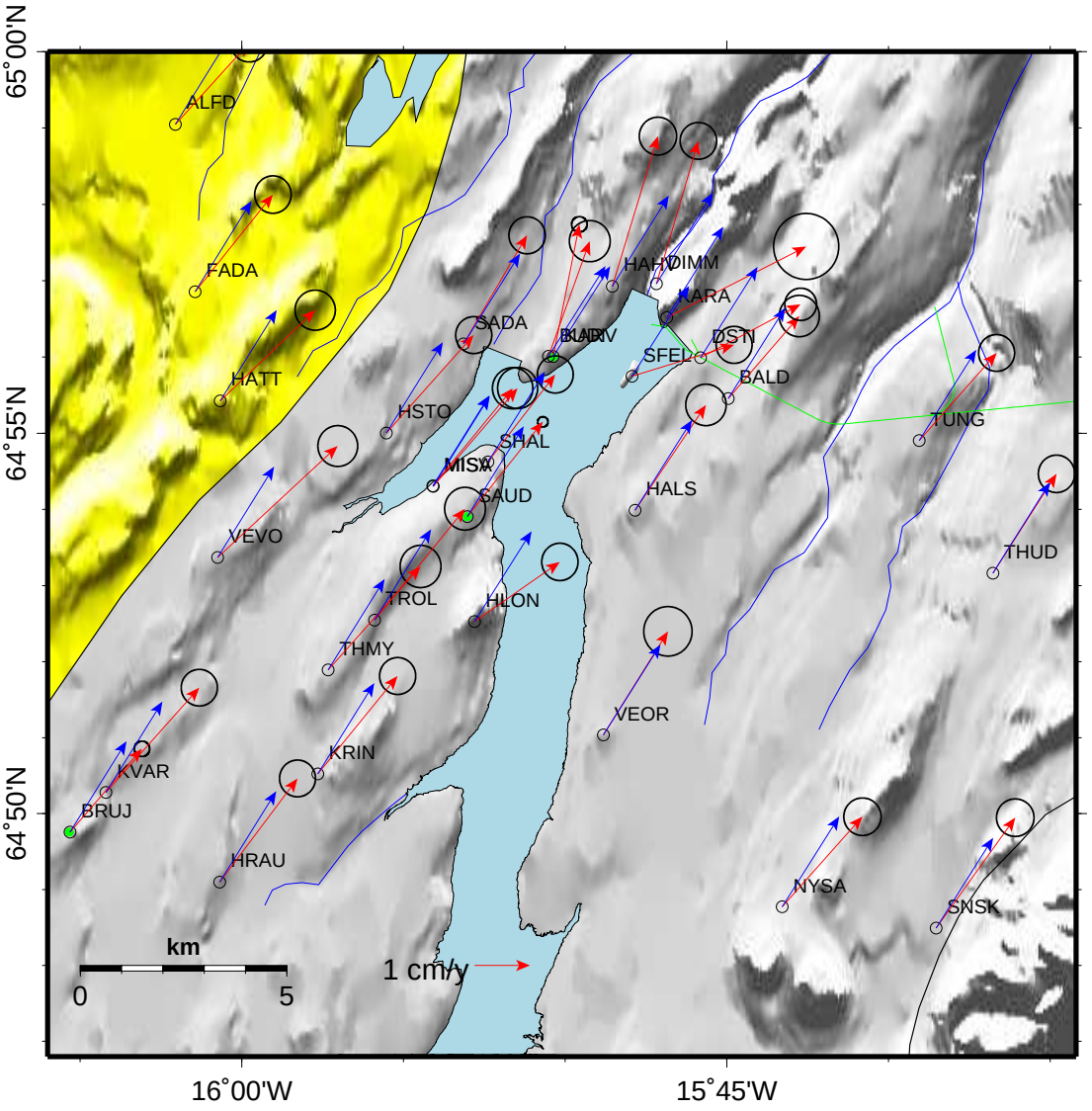

Figure 3.6: Horizontal velocities calculated from measurements in August 2005, August 2006 and August 2007 in the ITRF2005 reference frame (red arrows). Also shown are the predicted velocities of the NNR-NUVEL1A model (blue arrows) for the Eurasian Plate. The ellipses show the 95% confidence interval. The green line shows the tunnel that leads the water from the reservoir to the power plant. The figure shows the area inside the box in Figure 3.5. The estimated velocities are also shown in Table A.8.

3.1.1 Plate velocities

In order to the plate movements the velocities are also shown relative to a stable Eurasian Plate. In this case, the predicted velocities of the Eurasian Plate (blue arrows in Figures 3.1-3.6) are subtracted from the observed velocities (red arrows in Figures 3.1-3.6). For the 2005-2006 interval, the fixing of the Eurasian Plate by subtracting the velocity vectors from the NNR-NUVEL1A model shows that the network is mostly moving with the Eurasian Plate without deforming (Figures 3.7 and 3.8). For the 2006-2007 interval the velocities close to Hálslón (Figure 3.10) change significantly compared to 2005-2006. The average velocity 2005-2007 shows a slight deformation at the westernmost part of the network. This part of the network is only at about 20 km distance from the Askja caldera, that is expected to lie close to the central axis of the plate boundary of the plate boundary (*Sturkell and Sigmundsson*, 2000).

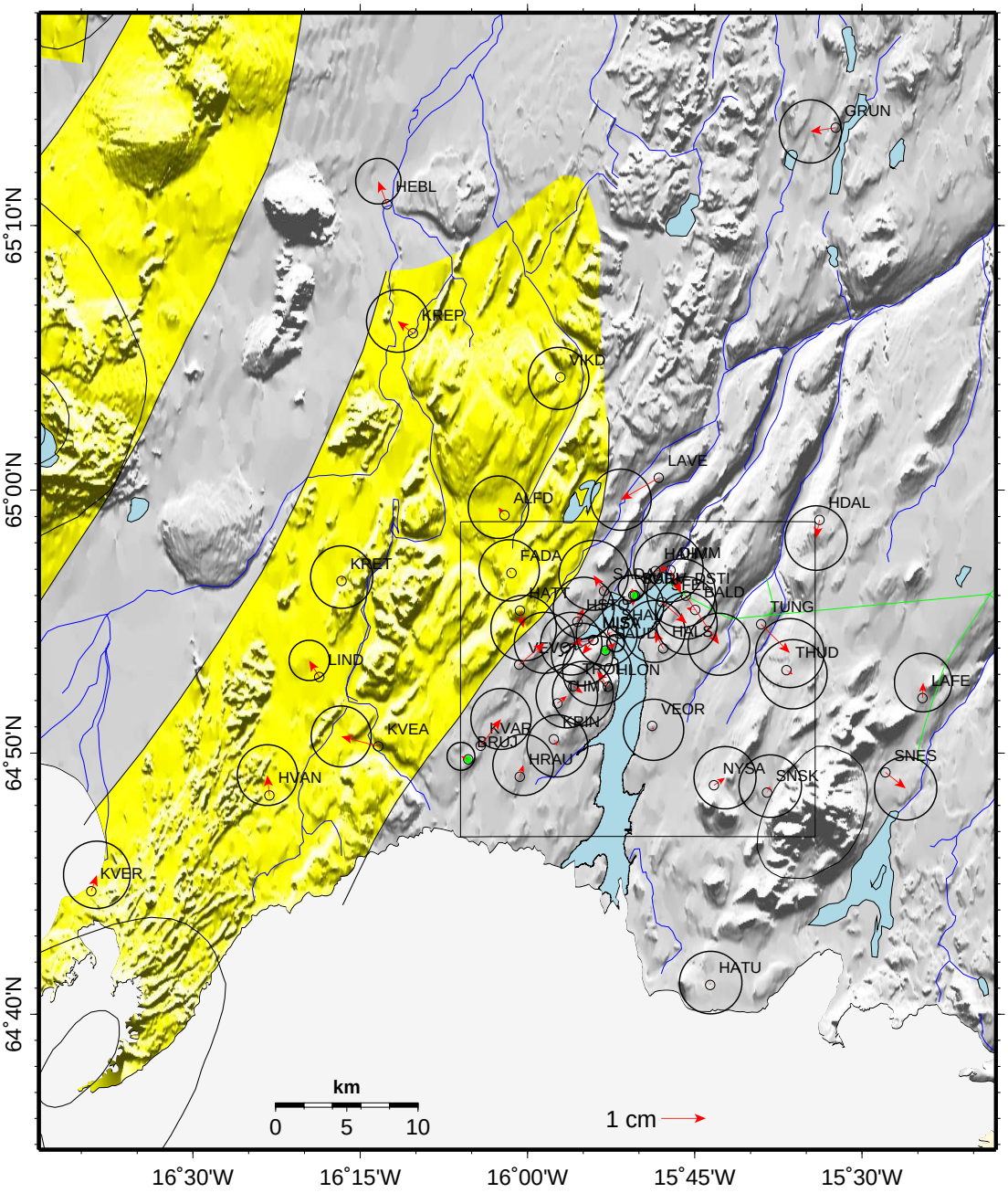

Figure 3.7: Horizontal velocities relative to the Eurasian Plate, based on measurements in 2005 and 2006. The ellipses show the 95% confidence interval. The green line shows the tunnel that leads the water from the reservoir to the power plant. The box shows the coverage of Figure 3.8. The estimated velocities are also shown in Table A.5.

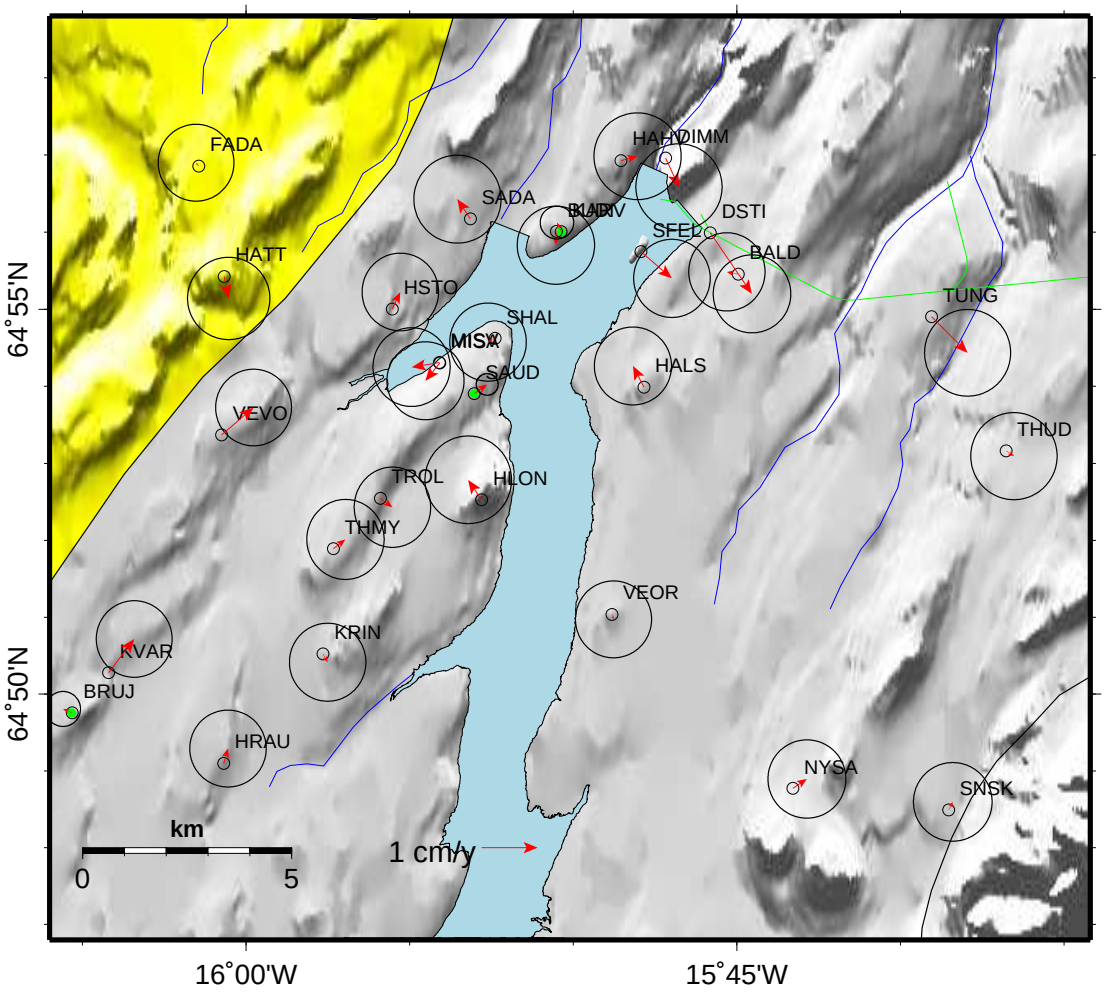

Figure 3.8: Horizontal velocities relative to the Eurasian Plate based on measurements in 2005 and 2006. The ellipses show the 95% confidence interval. The green line shows the tunnel that leads the water from the reservoir to the power plant. The stations DSTI and DUNG are showing displacements which is probably related to the tunnel. The figure shows the area inside the box in Figure 3.7. The estimated velocities are also shown in Table A.5.

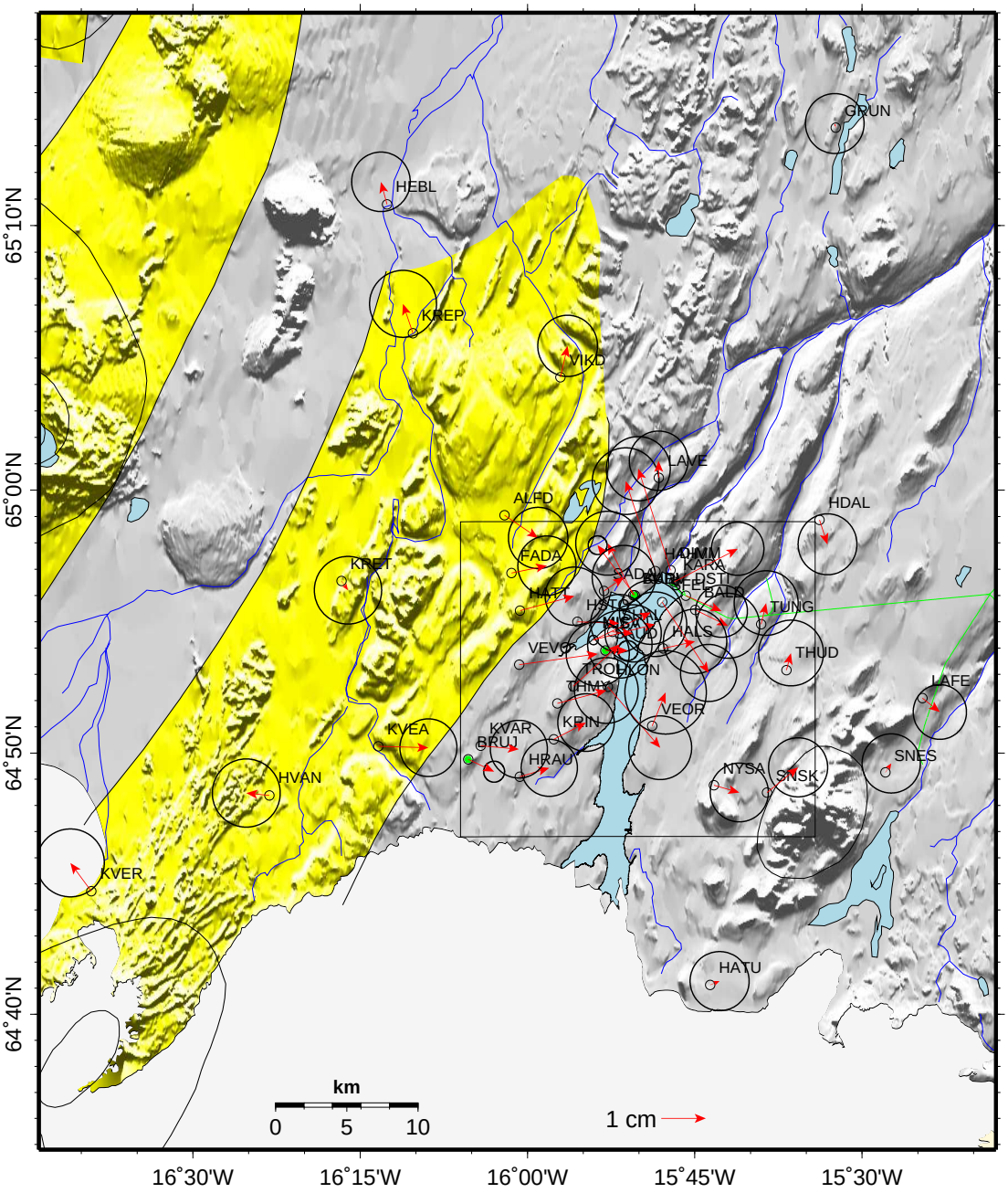

Figure 3.9: Horizontal velocities relative to the Eurasian Plate based on measurements in August 2006 and August 2007. The ellipses show the 95% confidence interval. The green line shows the tunnel that leads the water from the reservoir to the power plant. The box shows the coverage of Figure 3.10. The estimated velocities are also shown in Table A.7.

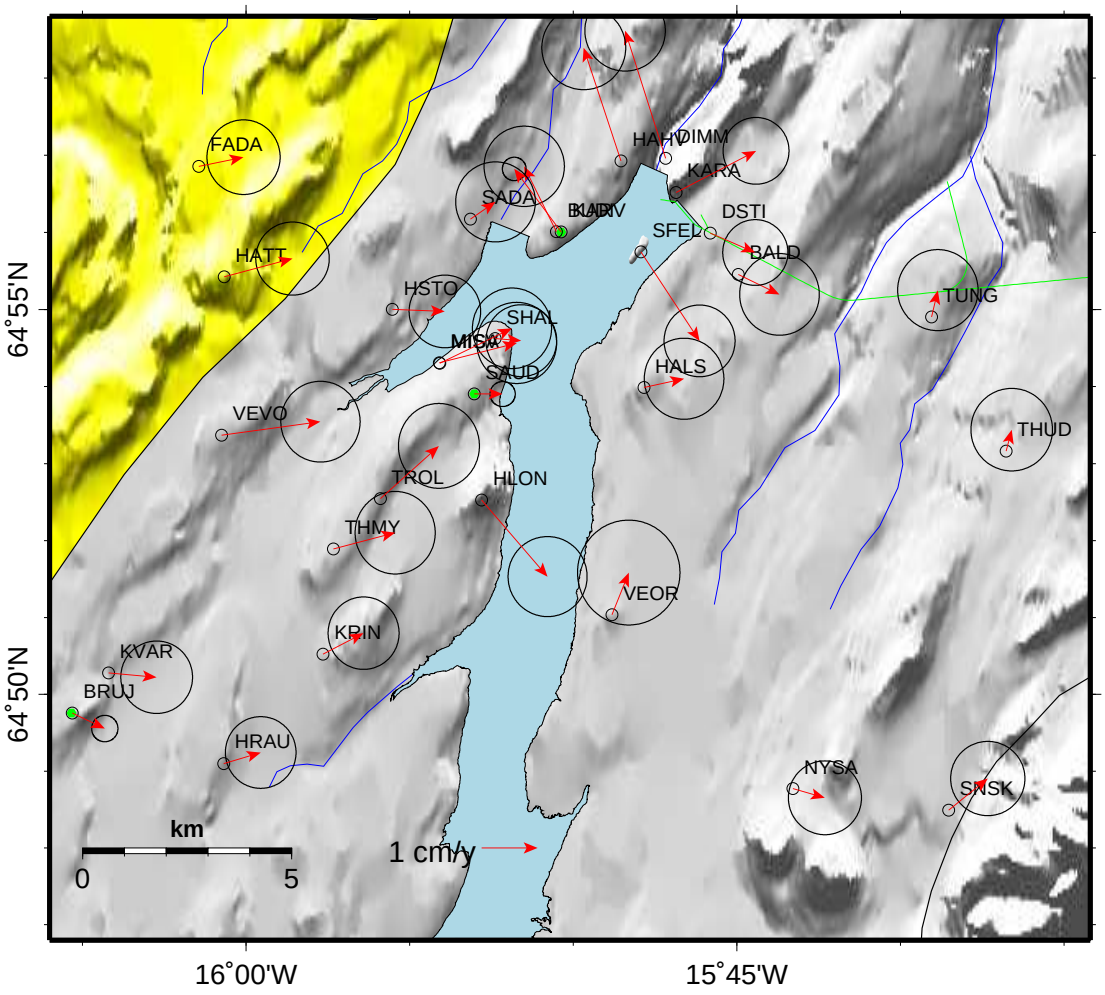

Figure 3.10: Horizontal velocities relative to the Eurasian Plate based on measurements in 2006 and 2007. The ellipses show the 95% confidence interval. The green line shows the tunnel that leads the water from the reservoir to the power plant. The figure shows the area inside the box in Figure 3.9. The estimated velocities are also shown in Table A.7.

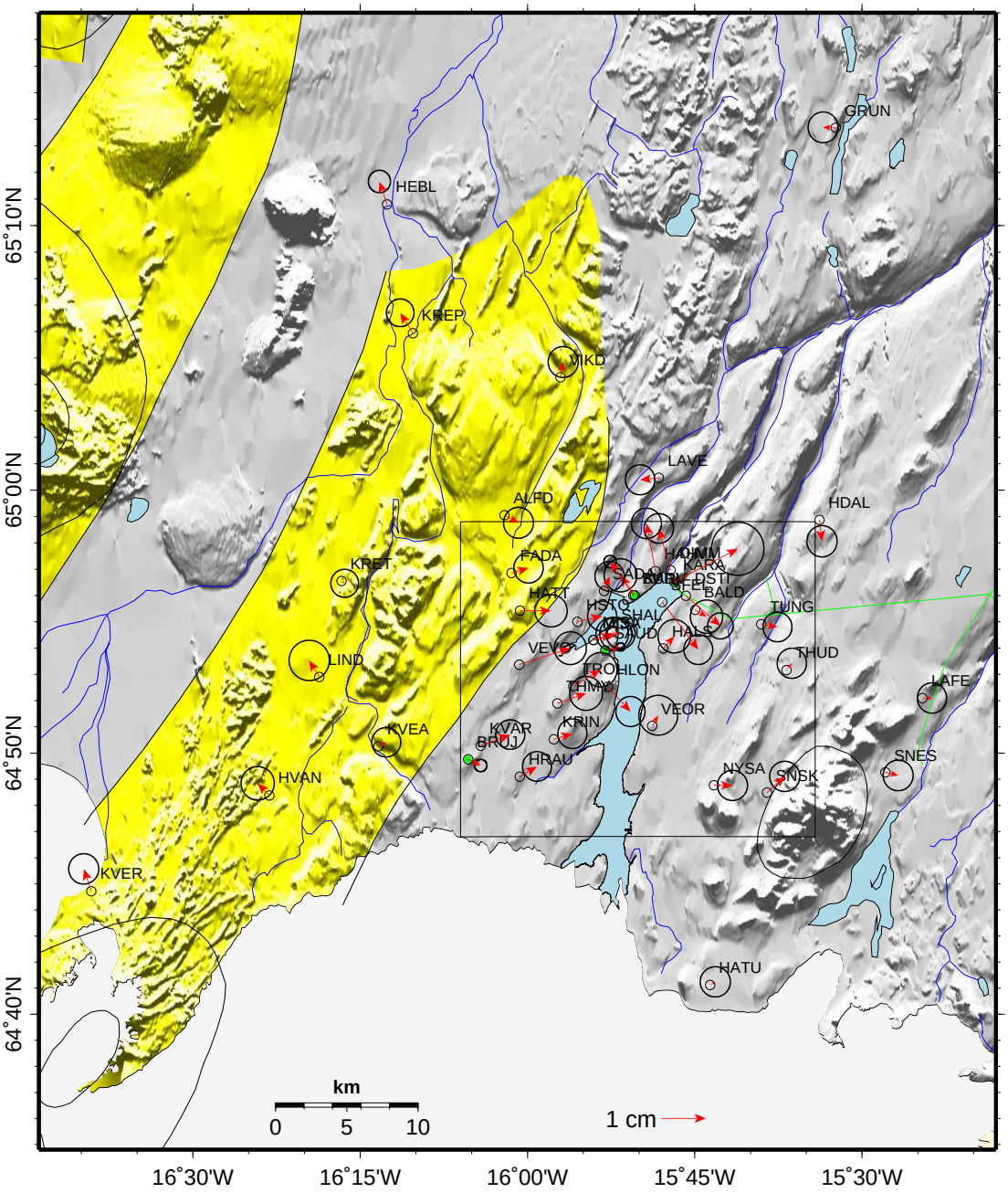

Figure 3.11: Average horizontal velocities relative to the Eurasian Plate based on measurements in August 2005, August 2006 and August 2007. The ellipses show the 95% confidence interval. The green line shows the tunnel that leads the water from the reservoir to the power plant. The box shows the coverage of Figure 3.12. The estimated velocities are also shown in Table A.9.

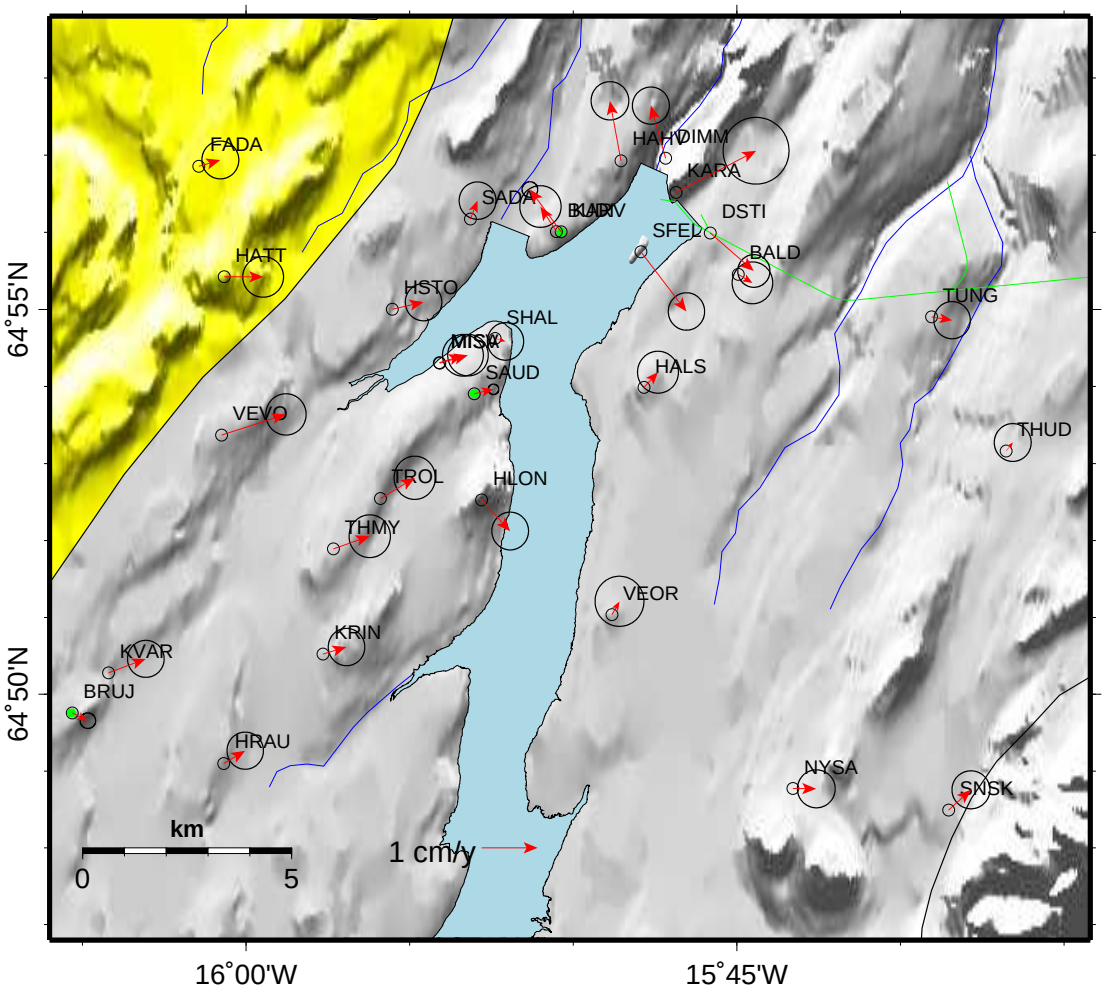

Figure 3.12: Average horizontal velocities relative to the Eurasian Plate based on measurements in August 2005, August 2006 and August 2007. The ellipses show the 95% confidence interval. The green line shows the tunnel that leads the water from the reservoir to the power plant. The figure shows the area inside the box in Figure 3.11. The estimated velocities are also shown in Table A.9.

3.2 Vertical velocities

Figures 3.13-3.18 show the vertical velocity fields derived from the three GPS campaigns. The velocities are also shown in Tables A.4-A.9. The vertical signal is dominated by high uplift rates.

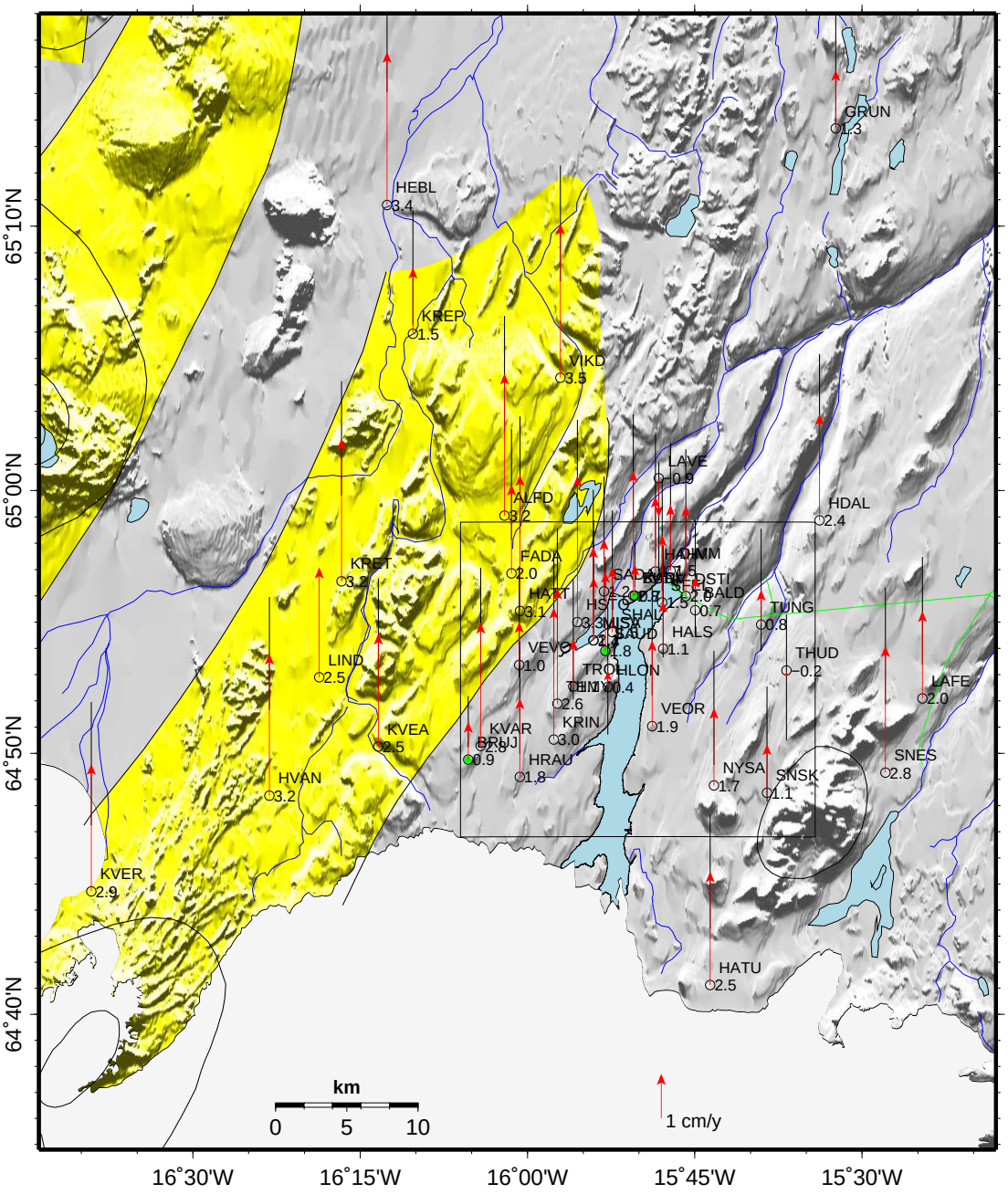

Figure 3.13: Vertical velocities based on measurements in August 2005 and August 2006 in the ITRF2005 reference frame. The black bars around the arrow heads show the size of the 95% confidence interval. The green line shows the tunnel that leads the water from the reservoir to the power plant. The box shows the coverage of Figure 3.14. The estimated velocities are also shown in Table A.5.

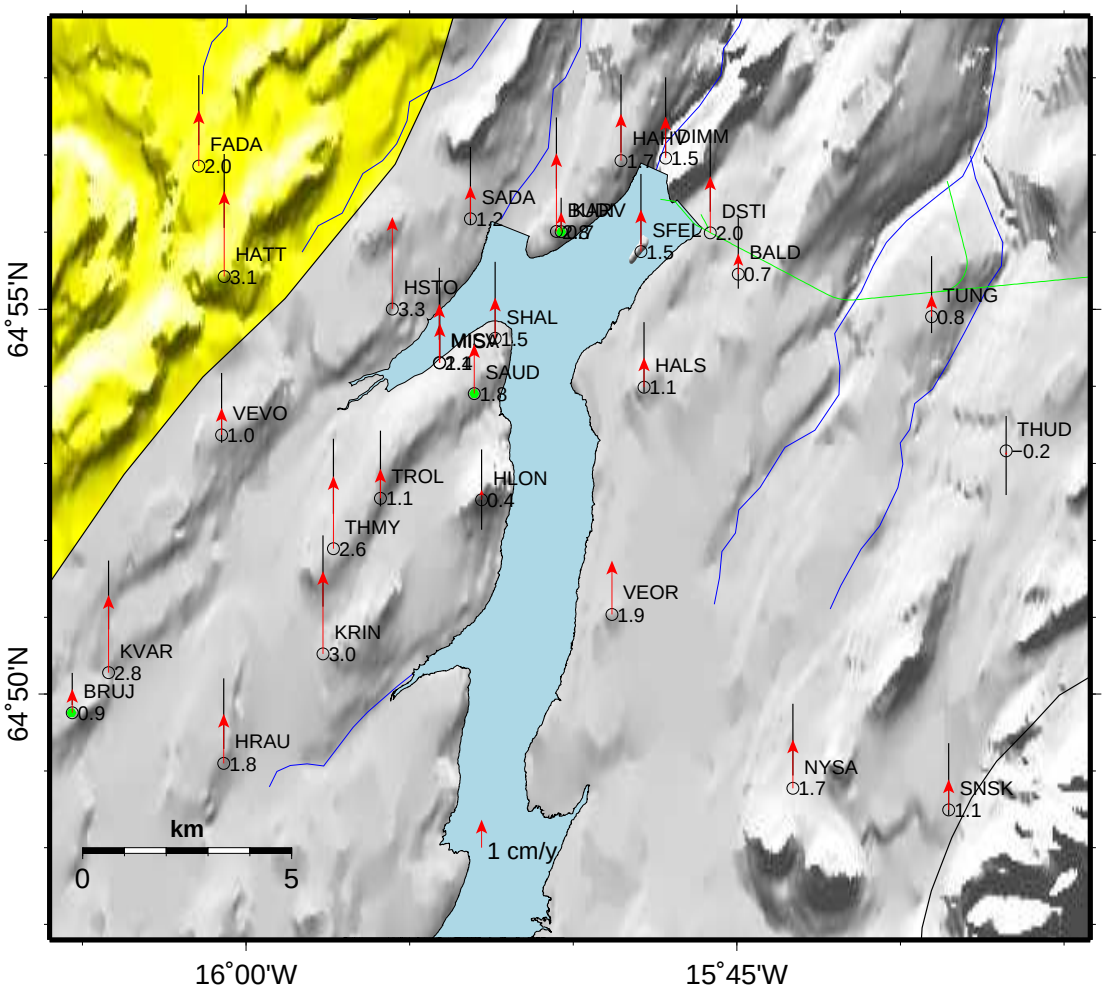

Figure 3.14: Vertical velocities based on measurements in August 2005 and August 2006 in the ITRF2005 reference frame. The black bars around the arrow heads show the size of the 95% confidence interval. The green line shows the tunnel that leads the water from the reservoir to the power plant. The figure shows the area inside the box in Figure 3.13. The estimated velocities are also shown in Table A.5.

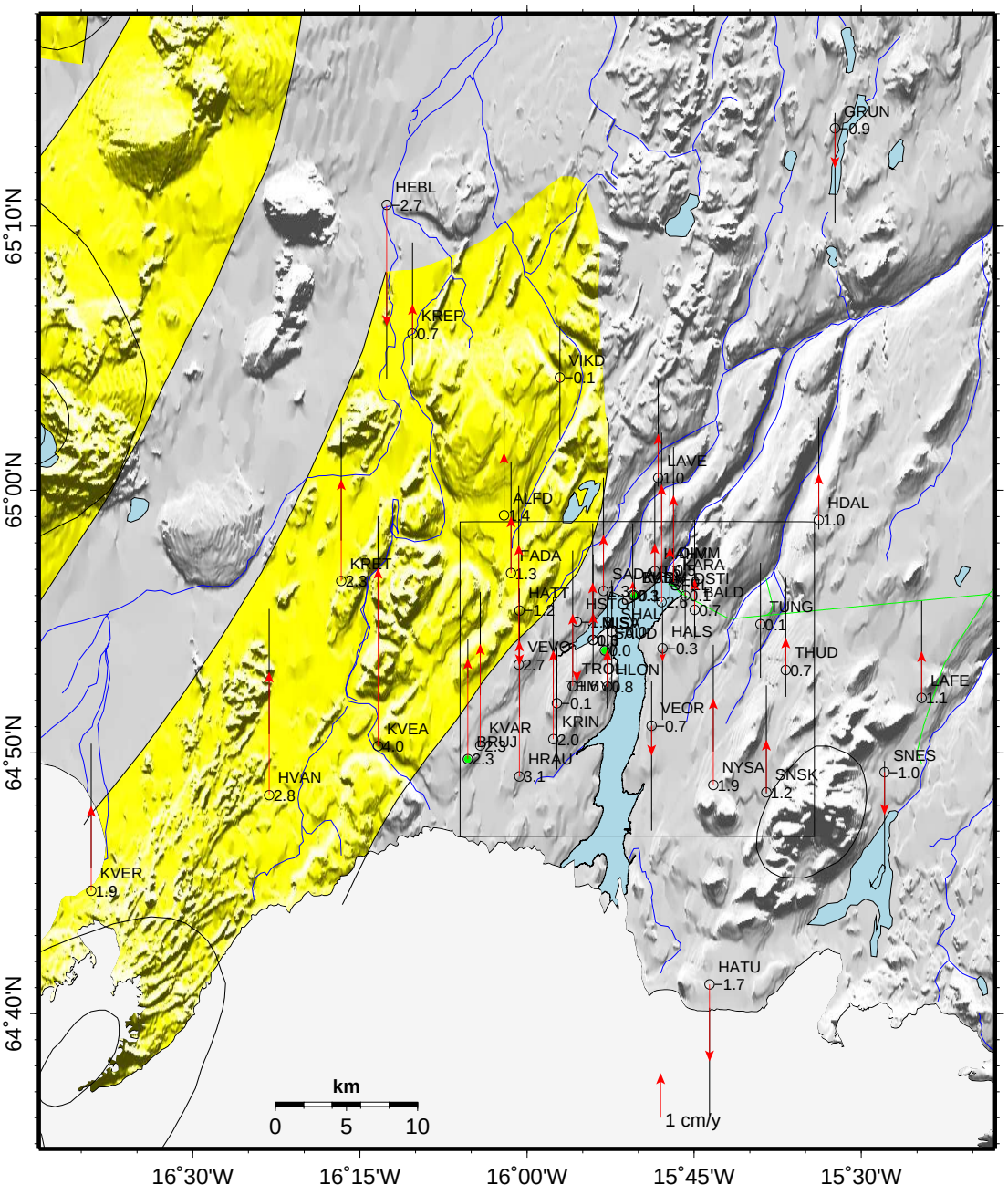

Figure 3.15: Vertical velocities based on measurements in August 2006 and August 2007 in the ITRF2005 reference frame. The black bars around the arrow heads show the size of the 95% confidence interval. The green line shows the tunnel that leads the water from the reservoir to the power plant. The box shows the coverage of Figure 3.16. The estimated velocities are also shown in Table A.7.

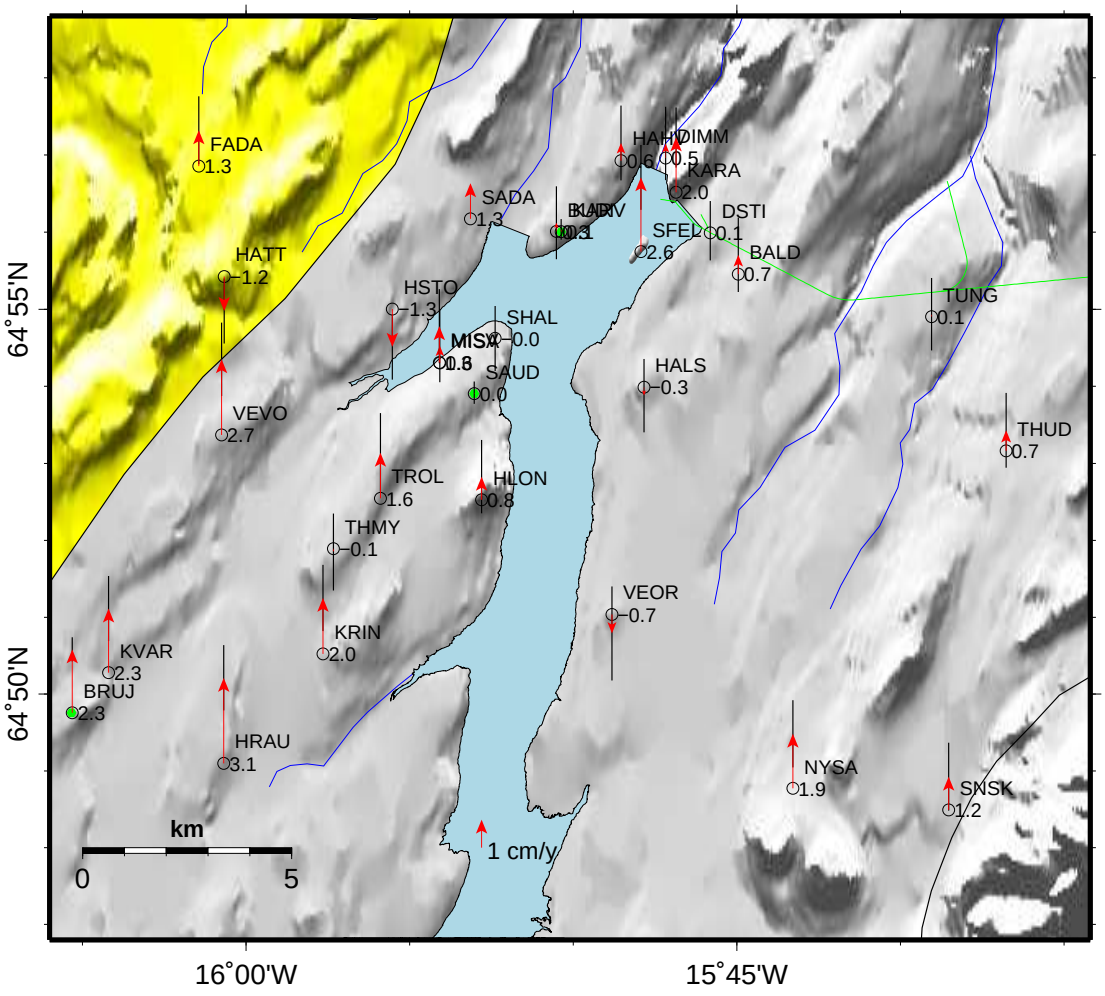

Figure 3.16: Vertical velocities based on measurements in August 2006 and August 2007 in the ITRF2005 reference frame. The black bars around the arrow heads show the size of the 95% confidence interval. The green line shows the tunnel that leads the water from the reservoir to the power plant. The figure shows the area inside the box in Figure 3.15. The estimated velocities are also shown in Table A.7.

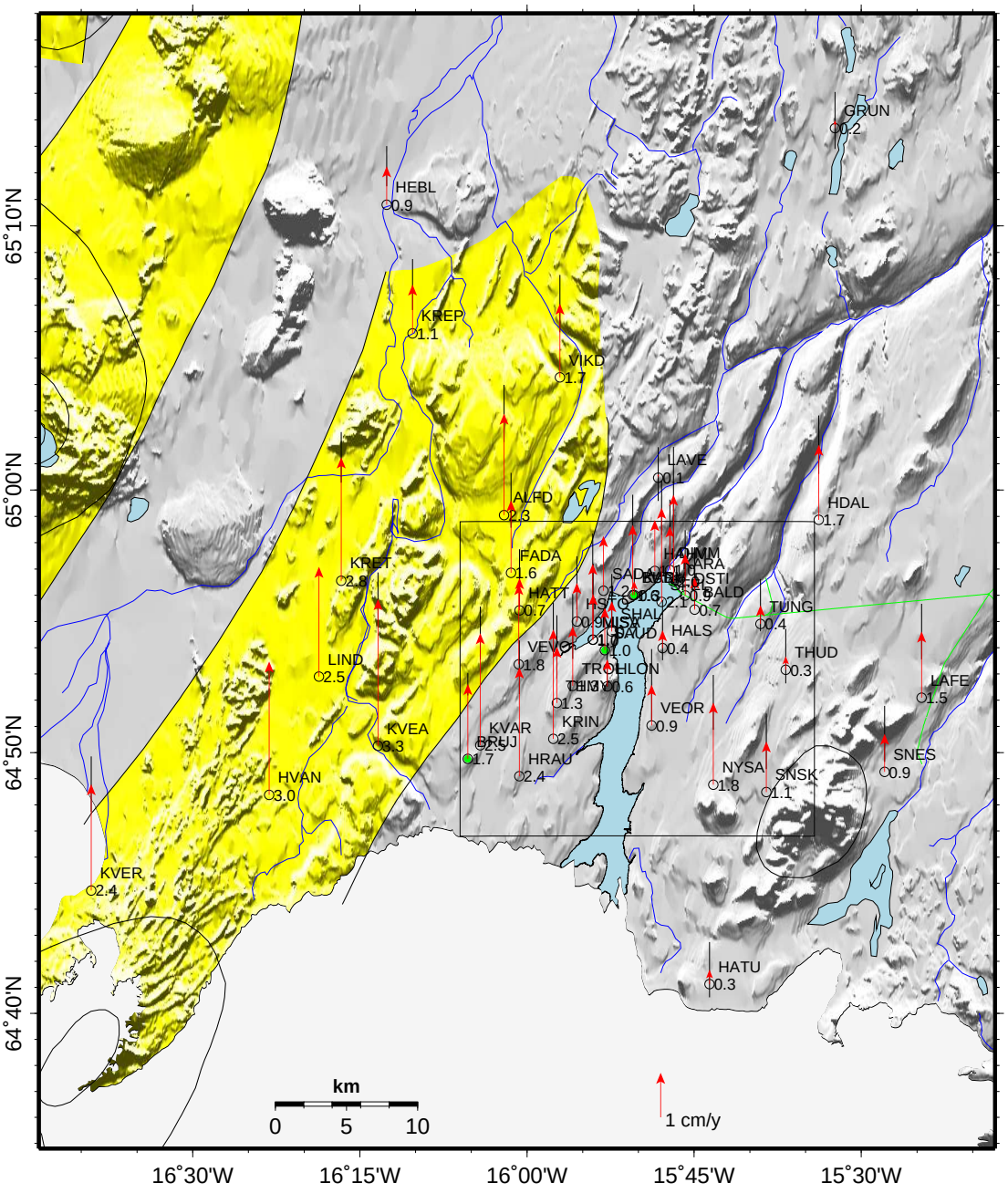

Figure 3.17: Vertical velocities based on measurements in August 2005, August 2006 and August 2007 in the ITRF2005 reference frame. The black bars around the arrow heads show the size of the 95% confidence interval. The green line shows the tunnel that leads the water from the reservoir to the power plant. The box shows the coverage of Figure 3.18. The estimated velocities are also shown in Table A.9.

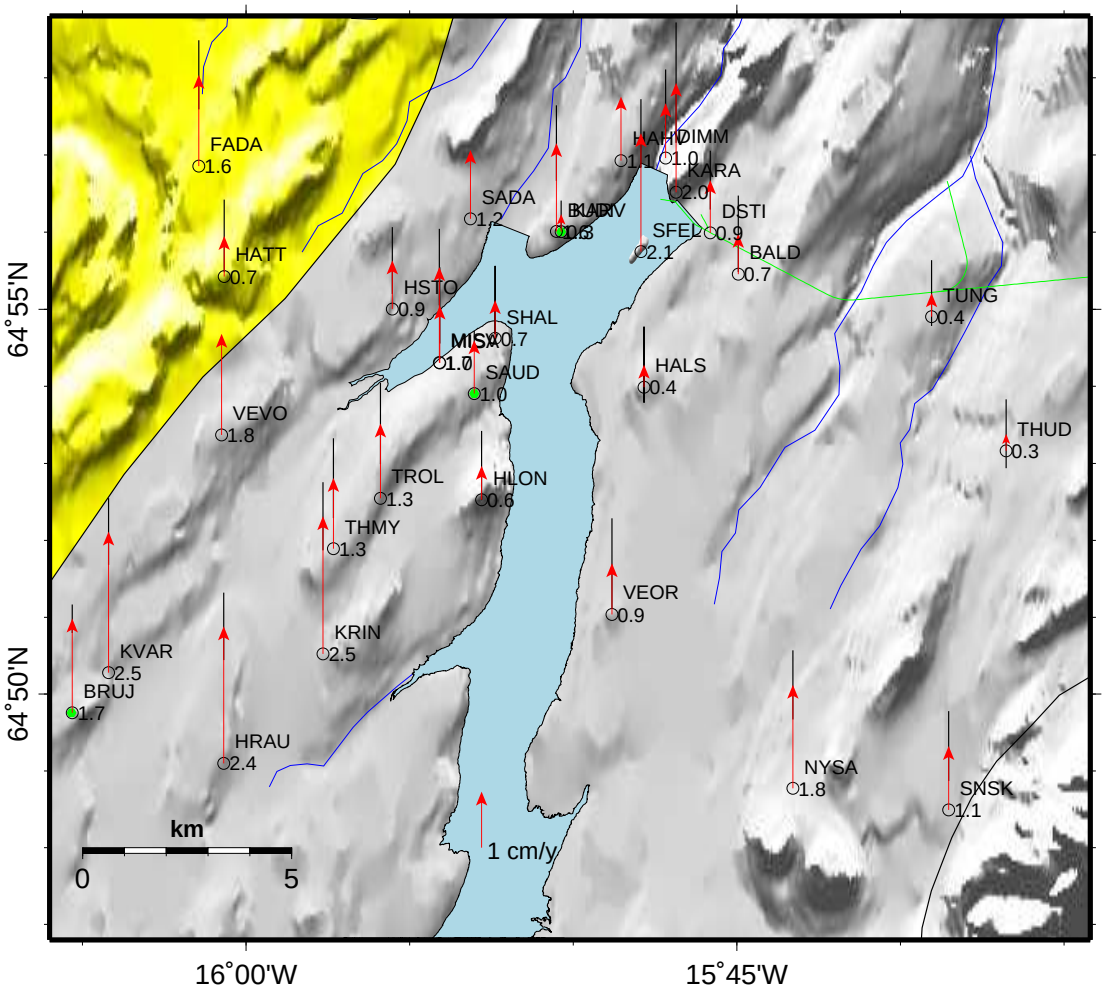

Figure 3.18: Vertical velocities based on measurements in August 2005, August 2006 and August 2007 in the ITRF2005 reference frame. The black bars around the arrow heads show the size of the 95% confidence interval. The green line shows the tunnel that leads the water from the reservoir to the power plant. The figure shows the area inside the box in Figure 3.17. The estimated velocities are also shown in Table A.9.

Chapter 4

Evaluation of deformation processes

4.1 Ongoing crustal deformation

In order to evaluate the deformation related to the filling of Hálslón reservoir, a background velocity field needs to be estimated. The 2005 and 2006 GPS campaigns where conducted before the filling of Hálslón began. The observed velocity field derived from these two GPS campaigns should give an estimate of the ongoing processes in the area prior to the formation of Hálslón. The stations close to the dam area, and above tunnel's need to be examined specially because of possible effects from the construction work. Stations DSTI, SFEL and TUNG (see Figure 3.8) are the only stations showing significant movements 2005-2006.

4.1.1 Horizontal velocities

The horizontal velocities are largely dominated by the plate spreading and are generally in agreement with the NNR-NUVEL1A plate model prediction for the Eurasian plate (see Figures 3.1 and 3.2). There is though a small bias toward the plate boundary at the western edge of the network (see Figures 3.7) which suggests that the westernmost part of the network is within the plate boundary deformation zone. After subtracting the plate velocities (see Figures 3.7-3.12) there is no sign of internal horizontal deformation in the network between 2005 and 2006, except for the westernmost part, and at the anomalous stations in close vicinity of the dams mentioned in Section 4.1.

For the later 2006-2007 interval there is, however, a clear sign of internal deformation that seems to relate to the filling of Hálslón (see Figures 3.9 and 3.10). Velocities of stations close to the northern part of the reservoir point away from the reservoir, indicating widening of faults under it. The largest velocities are at DIMM: (24±3) mm/yr with azimuth (342±3) ° and HAHV: (21 ± 3) mm/yr with

Table 4.1: The velocity field of the GPS stations closest to the dam area as displayed in Figure 3.10. The velocities are represented as size v and azimuth θ.

Station	v [mm/y]	θ [°]
BALD	8.2±2.9	116.0±26.2
BUDI	13.0±2.9	333.7±8.1
DIMM	23.9±2.9	342.4±3.0
DSTI	8.7±2.4	113.3±20.3
HAHV	21.2±3.1	341.7±3.7
KARA	16.1±2.4	62.5±10.8
KARV	14.0±0.9	323.4±3.0
SFEL	19.0±2.6	146.7±6.1

azimuth (342±4) ° see Table 4.1.

At more then 5 km distances from the dam area, the crustal response changes significantly from the response observed close to the dams. West of Hálslón, general movements toward Hálslón are observed, with 1-2 cm/yr, but east of it there is no response observed (Figure 3.10). This asymmetry between the west and the east site of Hálslón may suggest a significant change in rheological properties of the crust across the area.

4.1.2 Vertical velocities

In the study of glacio-isostatic deformation by *Pagli et al.* (2007), uplift rates from the southern edge of Vatnajökull were fitted to a Finite Element Model of the unloading of a circular disk centred at Vatnajökull's centre of mass as an approximation of Vatnajökull ice cap. The Earth model was axisymmetric, with an elastic plate over a uniform viscoelastic medium. The model is symmetric about the centre point so that the uplift rates are only a function of distance from the ice cap's centre. In the study by *Pagli et al.* (2007) a gradually decreasing uplift rates are detected and the best fit to the data were obtained by assuming an elastic thickness of 10-20 km and viscosity of $4 - 10 \times 10^{18}$ Pa s.

In order to study the uplift rates north of Vatnajökull (this study) as a function of distance from Vatnajökull's centre, the distance between the ice caps centre and the GPS stations has to be estimated. To calculate the distance between to points on Earths surface it is convenient to use a sphere approximation to estimate the great circle distance. Assume we have two points $\mathbf{r_f} = (x_f, y_f, z_f)$ and $\mathbf{r_s} = (x_s, y_s, z_s)$ which can be related to geographic coordinates by

$$\mathbf{r} = \mathrm{R_E}(\cos\phi\cos\lambda, \cos\phi\sin\lambda, \sin\phi) \tag{4.1}$$

where ϕ is a latitude, λ is longitude, h is the height an R_E is Earth's mean radus. The angle between these vectors ($\Delta\alpha$) is given with (e.g *Apostol*, 1975)

$$\cos\Delta\alpha = \frac{\mathbf{r_s}\cdot\mathbf{r_f}}{\|\mathbf{r_s}\|\,\|\mathbf{r_f}\|}. \tag{4.2}$$

Using spherical coordinates an and trigonometric identeties, the angle between the two points becomes

$$\Delta\widehat{\sigma} = \arctan\left(\frac{\sqrt{(\cos\phi_f\sin\Delta\lambda)^2 + (\cos\phi_s\sin\phi_f - \sin\phi_s\cos\phi_f\cos\Delta\lambda)^2}}{\sin\phi_s\sin\phi_f + \cos\phi_s\cos\phi_f\cos\Delta\lambda}\right), \tag{4.3}$$

where $\Delta\lambda$ is the longitude difference. If we take the Earth's mean Radius to be R_E=6371000 m, the great-circle distance between the the two points is $R_E\Delta\alpha$.

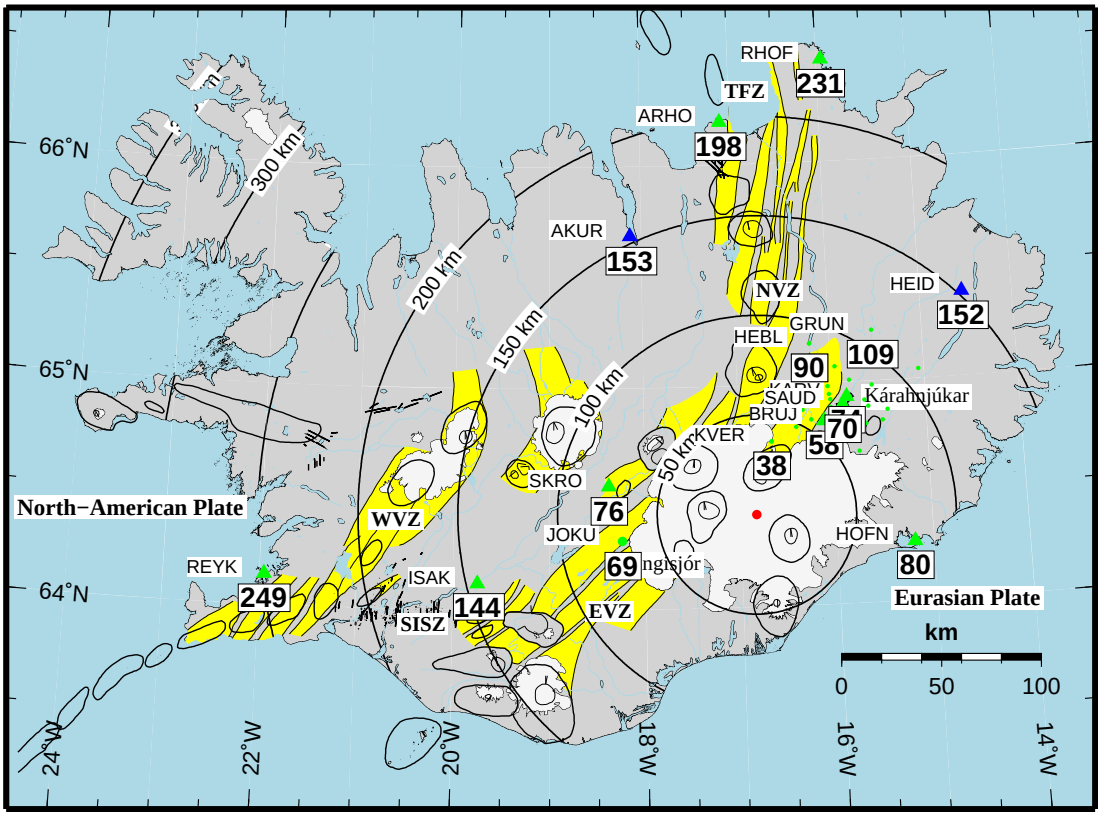

Figure 4.1: Distances of the GPS stations to the centre of Vatnajökull ice cap (red dot at N64°25′ W16°50′). The CGPS stations (green triangles) are labelled with the distance in km. Three of the campaign stations (green dots), GRUN, HEBL and KVER are labelled with the distance in km. KVER is the campaign GPS station closest to the ice cap's centre (38 km) and GRUN, farthest away (109 km).

Due to the short distance of Kárahnjúkar area from Vatnajökull's edges, a large part of the vertical movements may be assumed to be caused by the glacial

isostatic adjustment to thinning of Vatnajökull ice cap in as observed south of Vatnajökull by *Pagli et al.* (2007). If we define the centre of Vatnajökull as the point (N64°25′ W16°50′) we can calculate the distance to each point by using equation 4.3. The location of each station in relation to the distance from Vatnajökull's centre is shown in Figure 4.1. To study the change in uplift rates, the vertical velocities of all the GPS stations are plotted as a function of the distances from the centre of Vatnajökull. Figures 4.2 and 4.3 show the average velocities for the intervals 2005-2006 and 2006-2007 respectively. Figure 4.4 shows the average velocities in the interval 2005-2007.

At about 40-60 km distance from the ice caps centre the average velocities of the whole 2005-2007 period (Figure 4.4) are comparable (even a bit higher) to the velocities *Pagli et al.* (2007) observed at the same distance from the ice cap's centre which is on the order of 20-30 mm/yr. By looking only at the GPS stations far from Hálslón (green crosses in Figures 4.2 and 4.4) a similar observation can be made from Figures 4.2 and 4.3.

Horizontal velocities of up to (3±2) mm/yr due to isostatic adjustments are observed, in ∼50 km distance from the centre of Vatnajökull (*Pagli et al.*, 2007). These velocity vectors point away from the ice cap's centre. By looking at Figures 3.7 and 3.8 there is no clear indication of similar glacial isostatic adjustment as observed by *Pagli et al.* (2007). Even though the time series is too short for an evaluation of such a small signal a bias pointing away from the ice cap might be present. This could bee an indication that the crustal properties north of Vatnajökull are somewhat different from those south of the ice cap, or the glacial unloading is different. This is inconclusive until a better constraint on the velocity is obtained.

The GPS stations that are close to Hálslón are shown as red crosses in Figures 4.2 and 4.3 and are at a mean distance of 73 km. Comparison of Figures 4.2 and 4.3 reveals a decrease in vertical velocity close to the reservoir for 2006-2007, relative to the 2005-2006 period. This reduction in uplift rates correlates both spatially and temporally with the formation of the Hálslón reservoir. The mean uplift rate, close to Hálslón, in 2005-2006 is (16 ± 8) mm/yr and in 2006-2007 it is (2 ± 7) mm/yr. The decrease in uplift rates are therefore (14 ± 10) mm/yr and the subsidence estimated due to the reservoir in one year is then about 4-24 mm.

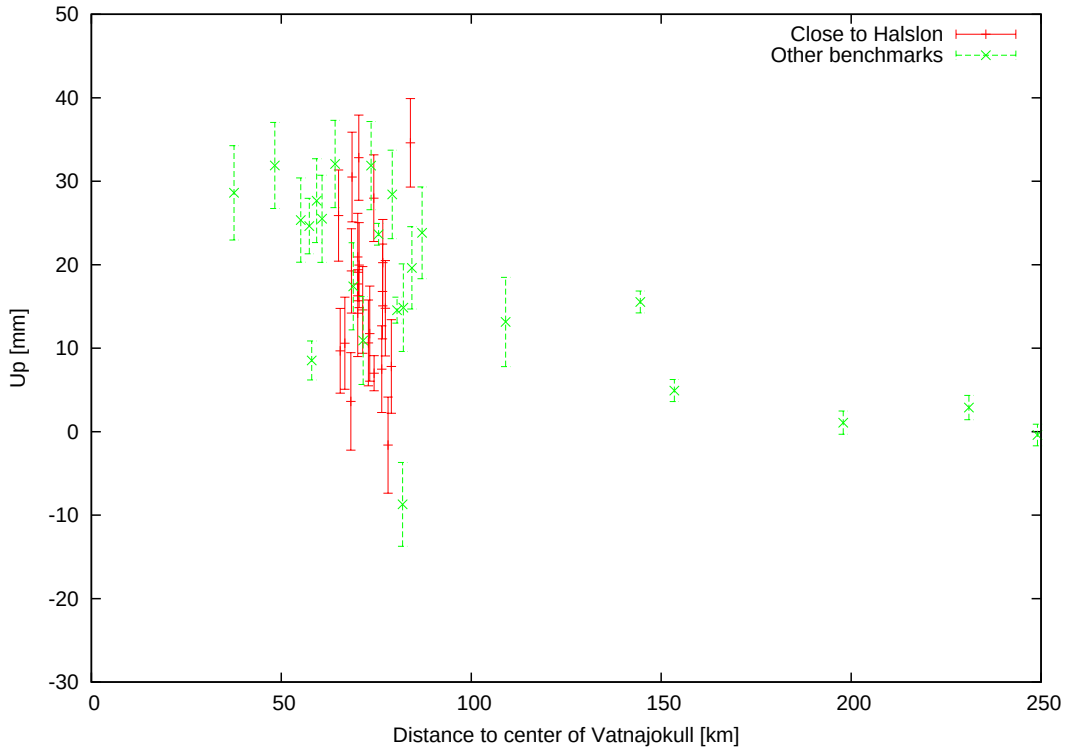

Figure 4.2: Vertical velocities as a function of distance from the centre of Vatnajökull glacier. Based on the measurements in August 2005 and August 2006, including the CGPS station REYK and the stations in east Iceland.

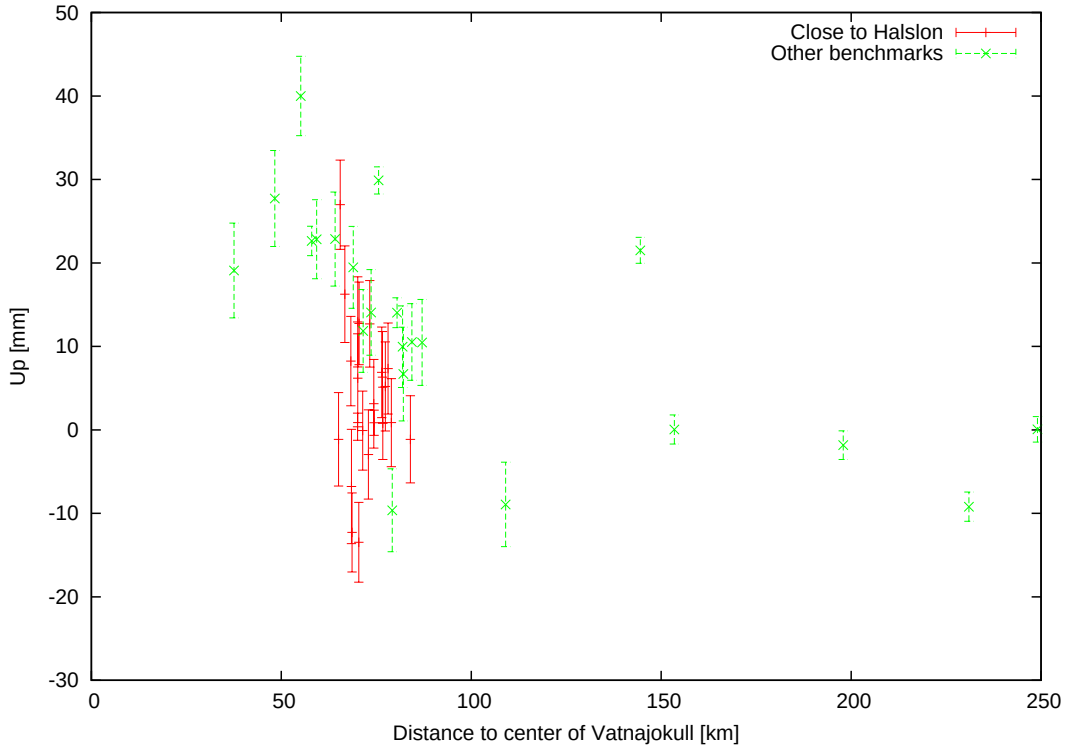

Figure 4.3: Vertical velocities as a function of distance from the centre of Vatnajökull glacier. based on the measurements in 2006 and 2007, including the ISGPS station REYK and the stations in east Iceland.

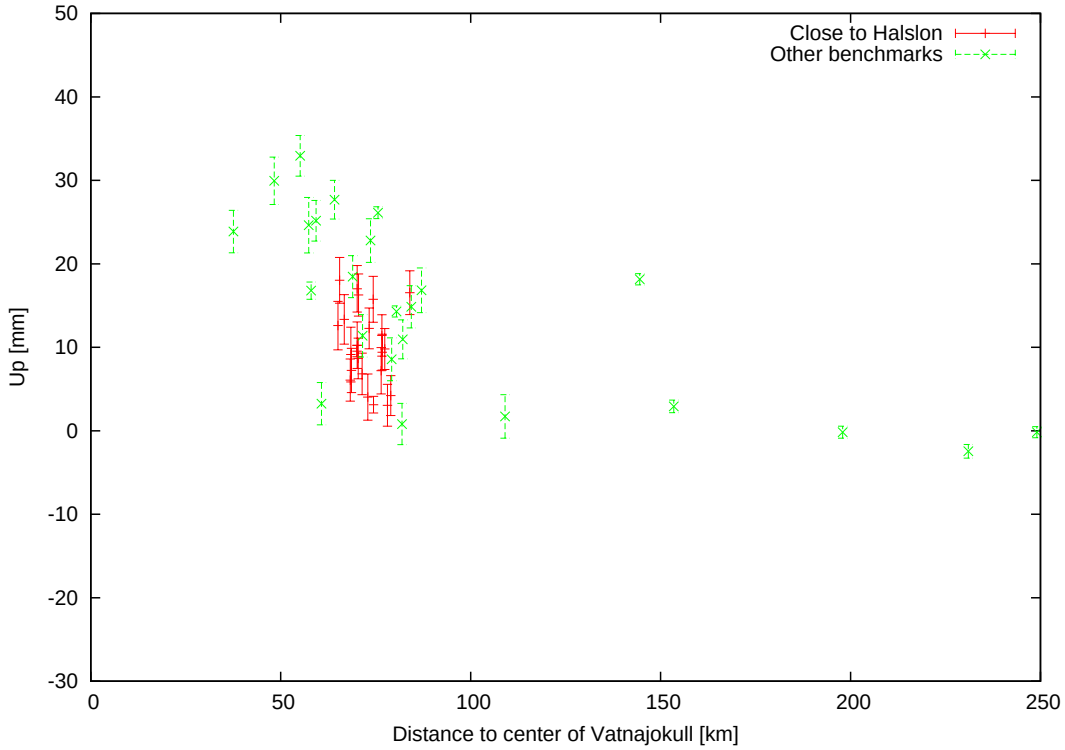

Figure 4.4: Vertical velocities as a function of distance from the centre of Vatnajökull glacier. based on the measurements in 2005, 2006 and 2007, including the ISGPS station REYK and the stations in east Iceland.

4.2 The effect of Hálslón on displacement fields

In order to evaluate the effect of the the filling of Hálslón on the deformation field, the velocity field from the 2005-2006 interval before the filling process began, is used as background velocity ($\dot{u}^*$). By assuming a steady state in the area before the filling of Hálslón began, the expected displacements can be calculated from the background velocity and compared with the observed displacements 2006-2007. We define $\Delta t = t_3 - t_1$ as the time interval between the first and the last measurements (interval used to estimate the displacements). u_{3i} is the observed displacements in August 2007 where i stands for (east, north or up) and $\dot{u}^*_{1i}$ is the least square fit (see Section 2.2.3) for the interval August 2005 until August 2006. Using $\dot{u}^*_{1i}$ as the background velocity, then the deviation from the background becomes

$$\Delta u_i = \dot{u}^*_{1i}\Delta t - u_{3i}, \tag{4.4}$$

and the uncertainty

$$\sigma_{\Delta u_i} = \sqrt{(\sigma_{\dot{u}^*_{1i}}\Delta t)^2 + (\sigma_{u_{3i}})^2} \tag{4.5}$$

where $\sigma_{\dot{u}^*_{1i}}$ and $\sigma_{u_{3i}}$ are the uncertainties of the relevant components. The Δu_i is zero if there are no changes in velocity between years. If we assume that the only change between the 2005-2006 and 2006-2007 is the filling of Hálslón, Δu_i shows the deformation due to the increased load. This is evaluated in Section 4.2.2.

4.2.1 Expected displacements

A preliminary study done by *Sigmundsson* (2002), assuming a point load at the northern end of Hálslón evaluated an eventual total maximum crustal subsidence up to about 30 cm with an initial elastic response of 1 cm the first year. A more refined model calculations for the elastic response have since been done by taking into account the geometry of Hálslón. A model by *Grapenthin and Sigmundsson* (2006) uses a Green's function approach to apply the load of Hálslón on an elastic half space (Figure 4.5). The same type of model was presented by *Grapenthin et al.* (2006) for the seasonal snow load of the four biggest ice caps in Iceland. A Young's modulus of 30 GPa and Poisson ratio of 0.25 is used to predict elastic response to the load of Hálslón (*Ófeigsson et al.*, 2006a, 2007a). These parameters give the best fit for the observed seasonal variations of the SAUD GPS station at Kárahnjúkar (*Grapenthin et al.*, 2006). The model predicts the horizontal and vertical elastic crustal response to the load of a full reservoir. As can be seen in Figure 4.5 the geometry of the reservoir influences the displacements, especially close to dam area. The red color in Figure 4.5 represents the largest displace-

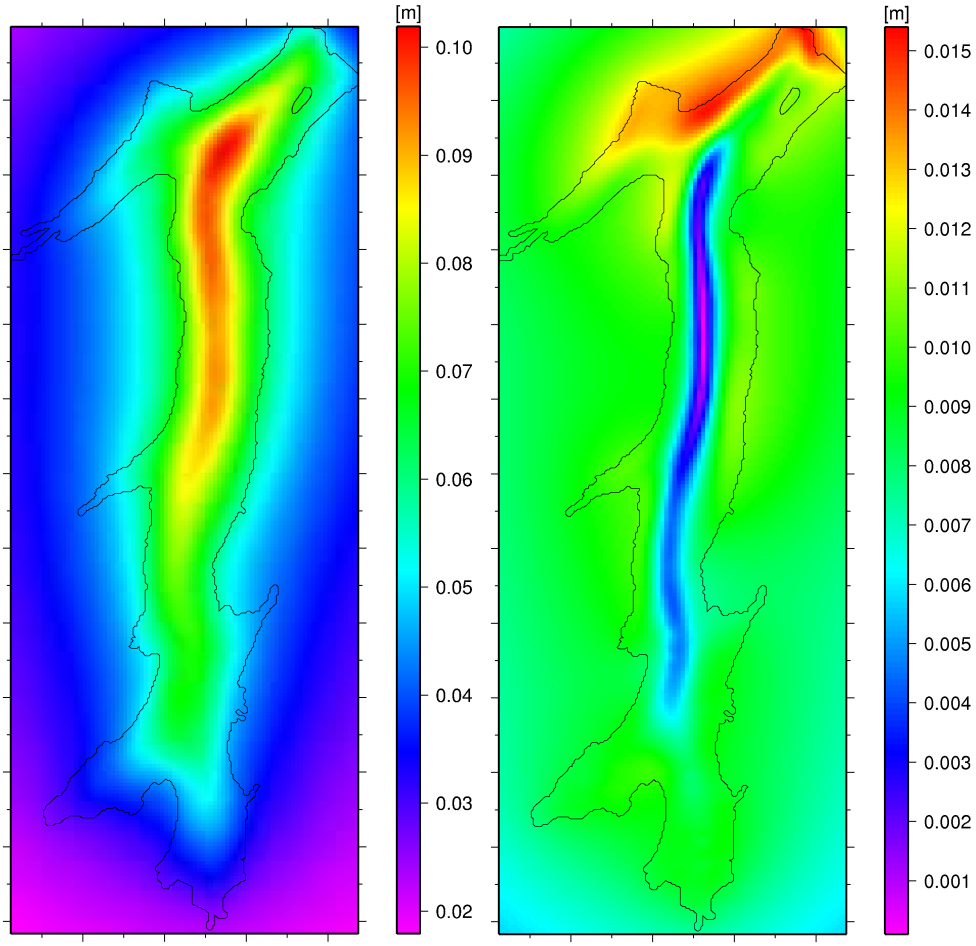

Figure 4.5: Modelled elastic crustal movements due to the load of the Hálslón reservoir when full. **Left:** The vertical displacement (subsidence). **Right:** The horizontal displacement (all displacements are pointing toward the reservoir). The red color represents the largest displacements. The maximum subsidence is about 0.1 m. A Young's modulus of 30 GPa and Poisson ratio of 0.25 is used to predict elastic response to the load .
Figure: Ronni Grapenthin (*Ófeigsson et al.*, 2007a).

ments. The predicted horizontal displacement field points toward the reservoir and the largest horizontal displacements are in the area around Sauðárdalur dam and Kárahnjúkar dam, 10-15 mm toward the reservoir. In other areas close to the reservoir the predicted displacement field varies from 7-10 mm in the direction to the reservoir (Figure 4.5). The predicted vertical displacements show subsidence with a maximum of 100 mm at the north end of Hálslón, just south of the dams. The subsidence then gradually decreases away from the centre to about 30 mm at a 10 km distance from it. In the vicinity of the Kárahnjúkar dam and at the Kárahnjúkar camp site the subsidence is 40-50 mm. These are the predicted displacements due to initial elastic response to weight of Hálslón, assuming a Young's modulus of 30 GPa, a possion ratio of 0.25 and uniform halfspace.

Prior to formation of Hálslón, the movements of faults underlying Hálslón reservoir where evaluated by *Snæbjörnsson et al.* (2006). The expected fault movements were strike-slip movements, normal movements and/or the combination of the two. Due to the general azimuth of faults underlying Hálslón area (Figure 1.3) the normal fault movements, should appear as an extension across Hálslón with direction between E-W and NW-SE. Strike-slip faulting occurres parallel to the fault plane moving therefore in direction between N-S and NE-SW. A combination gives a superposition of the two processes. In the study by *Snæbjörnsson et al.* (2006) it was concluded that movement on faults underlying Hálslón, due to the load of Hálslón and the increased pore pressure could be around $\sim$8 cm. The expected fault movements are, however, somewhat sensitive to the geometry of fault planes.

The observed deformation field close to Hálslón is most likely caused by a superposition of elastic response due to the weight of Hálslón reservoir and movements on faults underlying Hálslón. By taking into account the different characteristic of movements caused by these two processes they could eventually be separated.

4.2.2 Evaluation of displacements due to Hálslón

The horizontal displacements, estimated as described in Section 4.2, show similar behaviour as the velocities observed in Figure 3.9. Horizontal displacements estimated for the filling interval 2006-2007 are mostly confined to a 10-15 km distance from of Hálslón (Figure 4.6). Comparing the observed displacements to the elastic model in Figure 4.5 shows some discrepancies.

In close vicinity of the dams the observed displacements point away from the reservoir (see Figure 4.6). The displacement of the stations closest to the dams are shown in Table 4.2. The largest displacements are observed on HAHV: (23 ± 5) mm in direction $(334 \pm 7)^\circ$, located $\sim$0.5 km west of Kárahnjúkar dam, and DIMM: (31 ± 4) mm in direction $(341 \pm 4)^\circ$, located on the east site of Hafrahvammagljúfur west of Fremri Kárahnjúkar. On the east site of Hálslón at BALD the displacement observed is (11 ± 4) mm in direction $(113 \pm 30)^\circ$ opposite to the stations on west site of Hálslón. The widening across the reservoir between DIMM and BALD is (39 ± 6) mm in direction $(329 \pm 7)^\circ$. The observed displacements suggest widening of faults underlying Hálslón. Assuming a superposition of the fault movements and the elastic response to the load, the widening accross faults may be somewhat larger than observed.

For stations at a greater distance from the dam area, (those in Figure 4.6 that are not in Table 4.2), a significant asymmetry is observed from west to east.

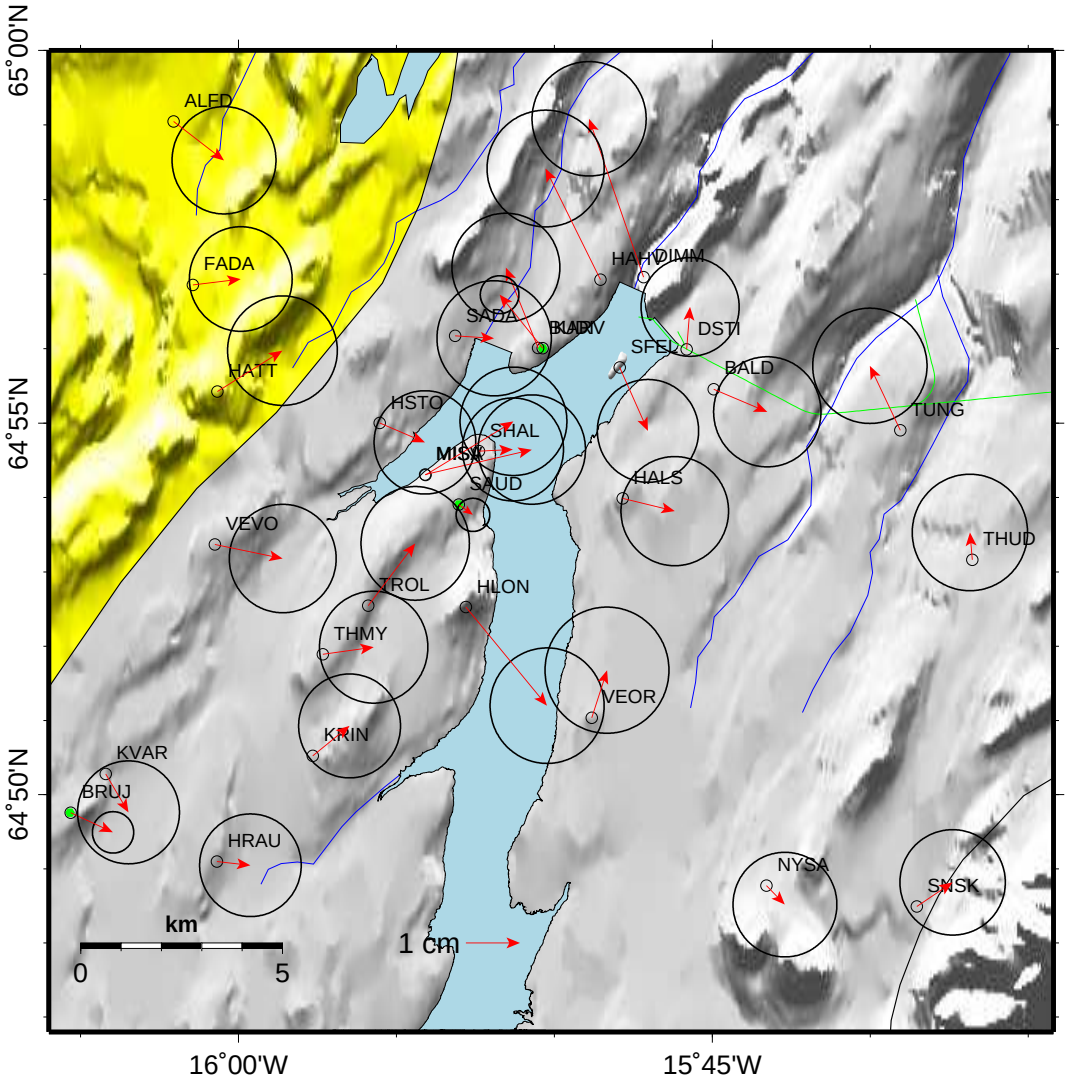

Figure 4.6: Estimated horizontal displacements due to the filling of Hálslón. The calculated velocities 2005-2006 are extrapolated to the same epoch as the measurements in 2007 and the difference between the estimated and the measured displacement calculated. The ellipses show the 95% confidence interval.

On the west site, displacements of 1-2 cm are generally in accordance with the model in Figure 4.5, but on the east side the displacements are negligible. This suggests that the crustal parameters are changing significantly across the area. The vertical displacements are less conclusive then the horizontal displacements, due to the large uncertainties. But a general subsidence of (14 ± 10) mm is observed (Figure 4.7). This is around half of the subsidence predicted by the model in Figure 4.5.

Table 4.2: The displacement field of the GPS stations closest to the dam area as displayed in Figure 4.6. The displacements are represented as size u and azimuth θ.

Station	u [mm]	θ [°]
BALD	10.7±4.1	113.0±28.5
BUDI	16.0±4.1	338.1±7.7
DIMM	30.9±4.3	341.0±3.7
DSTI	7.9±3.7	4.5±3.0
HAHV	22.9±4.4	333.7±6.9
HALS	9.9±4.1	103.7±32.5
KARV	12.7±1.4	321.2±5.8
SFEL	12.8±3.9	156.0±9.9

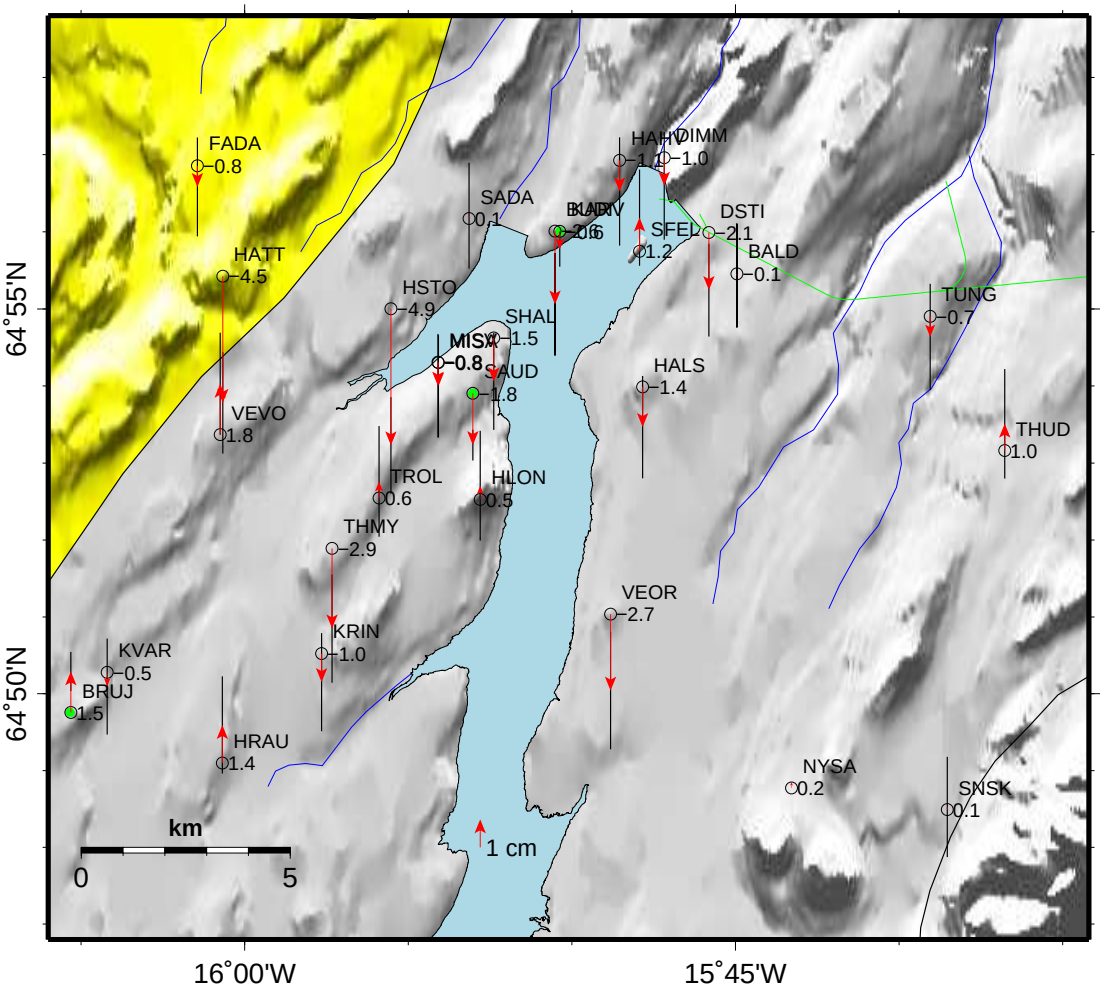

Figure 4.7: vertical displacements due to the filling of Hálslón. The calculated velocities 2005-2006 are extrapolated to the same epoch as the measurements in 2007 and the difference between the estimated and the measured displacement calculated. The black bars show the 95% confidence interval.

Chapter 5

Conclusions

A new study of load induced deformation has been conducted in the area north of Vatnajökull ice cap, in association with formation of the Hálslón water reservoir in the Kárahnjúkar area. An extensive network for crustal deformation research was established in the area in 2005 and later resurveyed. A total of 35 benchmarks were measured in GPS-campaigns in August, 2005, August, 2006 and again in August 2007.

The results from the 2005-2006 GPS campaigns suggest that the area close to Hálslón is outside the main deformation zone of the plate boundary. The deformation observed in the 2006-2007 GPS campaign can therefore be related directly to the filling of Hálslón, if "background" deformation processes operating prior to the filling are properly considered.

Deformation related to formation of Hálslón 2006-2007, in the vicinity of the dams, shows horizontal velocity field pointing away from the reservoir. The largest velocities, in the 2006-2007 period, are at stations DIMM, (24±3) mm/yr with azimuth (342±3)°, located north of the Kárahnjúkar dam, and HAHV, (21 ± 3) mm/yr with azimuth (342±4)°, located west of the dam. On the east side of Kárahnjúkar dam, DSTI, (9 ± 3) mm/yr with azimuth (113±20)°, is moving in the opposite direction. Local fault movements are the most likely cause for these movements. The displacements associated with the filling of Hálslón have been derived from from the change is velocities between the interval before the filling of Hálslón began (2005-2006) and the interval during the filling of Hálslón (2006-2007). The largest displacements observed are on HAHV: (23 ± 5) mm in direction (334±7)° and DIMM: (31±4) mm direction (341±4)°, both on the west side of Hálslón. On the east side of Hálslón at BALD the infered displacement is (11 ± 4) mm in direction (113 ± 30)°, in opposite direction to the stations on west side of Hálslón. The widening across the reservoir between DIMM and BALD is (39 ± 6) mm in direction (329 ± 7)°. The widening of faults may be larger

than these displacements indicate, as the load response can reduce the observed widening.

In the far region a different displacement field is observed. The horizontal displacements west of Hálslón are on the order of 10-15 mm toward Hálslón, but on the east side significant movements are absent. This suggests that the crustal parameters are changing significantly with distance from the plate boundary.

The glacial isostatic adjustments dominates the vertical displacements. At distance of about 50 km from the center of Vatnajökull the uplift rate is 20-30 mm/yr and is for most parts in agreement with previous studies of glacio-istostacy around Vatnajökull. The average uplift rate in the Hálslón area (average of 73 km distance from centre of Vatnajökull) prior to the filling is (16 ± 8) mm/yr reducing to averge of (2 ± 7) mm/yr between August 2006 and August 2007, while Hálslón was being filled. Estimated average subsidence during the filling of Hálslón (2006-2207) is (14 ± 10) mm.

The model using a Green's function approach to apply the load of Hálslón on an elastic half space, assuming Young's modulus of 30 GPa, overestimates the vertical response by a factor of two but the horizontal model displacements west of Hálslón are in a general agreement with the observed displacements in the far field. This indicates variable crustal strength, and that the crust in the area can not be characterised by a single Young's modulus.

Bibliography

Altamimi, Z., X. Collilieux, J. Legrand, B. Garayt, and C. Boucher (2007), ITRF2005: A new release of the international terrestrial reference frame based on time series of station positions and earth orientation parameters, *Journal of Geophysical Research*, *112*, B09401, doi:10.1029/2007JB004949.

Apostol, T. M. (1975), *Calculus: Multi-Variable Calculus and Linear Algebra, with Applications to Differential Equations and Probability*, vol. 2, 2nd ed., John Whiley & Sons Inc.

Árnadóttir, T., B. Lund, W. Jiang, H. Geirsson, E. Sturkell, F. Sigmundsson, P. Einarsson, and T. Sigurdsson (2007), Rapid uplift and plate spreading observed by GPS in Iceland, in *EGU General Assembly*, vol. 9, European Geosciences Union, Vienna, Austria, Geophys. Res. Abstracts.

Björnsson, H. (1979), Glaciers in Iceland, *Jökull*, *29*, 74 – 80.

Björnsson, H., F. Pálsson, and H. H. Haraldsson (2002), Mass balance of Vatnajökull (1991-2001) and Langjökull (1996-2001), Iceland, *Jökull*, *51*, 75 – 78.

Brohan, P., J. J. Kennedy, I. Harris, S. F. B. Tett, and P. D. Jones (2006), Uncertainty estimates in regional and global observed temperature changes: A new data set from 1850, *JGR*, *111*, D12106, doi:10.1029/2005JD006548.

Dach, R., U. Hugentobler, P. Fridez, and M. Meindl (2007), *Bernes GPS software Version 5.0*, user manual of the Bernese GPS Software Version 5.0.

DeMets, C., G. Gordon, D. Argus, and S. Stein (1994), Effect of recent revision to the geomagnetic reversal time scale on estimates of current plate motions, *GRL*, *21*, 2191 – 2194.

Einarsson, P. (1991a), Earthquakes and present-day tectonism in Iceland, *Tectonophysics*, *189*, 261 – 279.

Einarsson, P. (1991b), Umbrotin við Kröflu 1975 – 1989, in *Náttúra Mývatns*, edited by Árni Einarsson and A. Garðarsson, pp. 97 – 139, Hið Íslenska Náttúrufræðifélag.

Einarsson, P., and K. Sæmundsson (1987), Earthquake epicenters 1982-1985 and volcanic systems in Iceland, in *Í hlutarins eðli*, edited by Þ. I. Sigfússon, Menningarsjóður, Reykjavík, map accompanying Festschrift for Þorbjörn Sigurgeirsson.

Geirsson, H. (2003), Continuous GPS measurements in Iceland 1999 - 2002, Master's thesis, Faculty of Science, Department of Physics, University of Iceland.

Geirsson, H. (2008), Samfelldar GPS-mælingar Veðurstofunnar, Vefsíða. URL `http://hraun.vedur.is/ja/gps.html`

Geirsson, H., T. Árnadóttir, C. Völksen, W. Jiang, E. Sturkell, T. Villemin, P. Einarsson, F. Sigmundsson, and R. Stefánsson (2006), Current plate movements across the Mid-Atlantic ridge determined from 5 years of continuous GPS measurements in Iceland, *Journal of Geophysical Research*, *111*, B09407, doi:19.1029/2005JB003717.

Grapenthin, R., and F. Sigmundsson (2006), *Green's Funcions and Crustal Deformation - Manual and Examples*, Institute of Earth Sciences, University of Iceland, Nordic Volcanological Center, report 0602.

Grapenthin, R., F. Sigmundsson, H. Geirsson, T. Árnadóttir, and V. Pinel (2006), Icelandic rhythmics: Annual modulation of land elevation and plate spreading by snow load, *GRL*, *33*, L24305, doi:10.1029/2006GL028081.

Gupta, H. K. (2002), A review of recent studies of triggered earthquakes by artificial water reservoirs with special emphasis on earthquakes in Koyna, India, *Earth-Science Reviews*, *58*, 279–310.

Guðmundsson, A., and J. Helgason (2004), Kárahnjúkar hydroelectric project, *Assessment of the Hálslón tectonic activity LV-2004/162*, Landsvirkjun.

Hards, V. L., P. D. Kempton, R. N. Thompson, and P. B. Greenwood (2000), The magmatic evolution of the Snaefell volcanic centre; an example of volcanism during incipient rifting in Iceland, *Journal of Volcanology and Geothermal Research*, *99*, 97–121.

Höskuldsson, A., R. S. J. Sparks, and M. R. Carroll (2006), Constraints on the dynamics of subglacial basalt eruptions from geological and geochemical observations at Kverkfjöll, NE-Iceland, *Bulletin of Volcanology*, *68*, 689–701, doi: 10.1007/s00445-005-0043-4.

LaFemina, P. C., T. H. Dixon, R. Malservisi, T. Árnadóttir, E. Sturkell, F. Sigmundsson, and P. Einarsson (2005), Geodetic gps measurements in south Iceland: Strain accumulation and partitioning in a propagating ridge system, *Journal of Geophysical Research*, *110*(B1140), doi:10.1029/2005JB003675.

McCarthy, D. D., and G. Petit (2004), IERS conventions (2003), *Technical Note 32*, IERS Convention Centre.

Ófeigsson, B. G., P. Einarsson, F. Sigmundsson, E. Sturkell, H. Ólafsson, R. Grapenthin, and H. Geirsson (2006a), Expected crustal movements due to the planned Hálslón reservoir in Iceland, in *Fall Meeting suppl.*, vol. 87(52), Eos, Transactions, AGU, abstract T13A-0495.

Ófeigsson, B. G., E. Sturkell, H. Ólafsson, P. E. Freysteinn Sigmundsson, and J. T. X. Búi (2006b), GPS network measurements in the kárahnjúkar area 2005, *Tech. Rep. LV-2006/092*, Landsvirkjun.

Ófeigsson, B. G., P. Einarsson, F. Sigmundsson, E. Sturkell, H. Ólafsson, R. Grapenthin, and H. Geirsson (2007a), Crustal response to the formation of the Hálslón reservoir in Iceland., in *Fall Meeting suppl.*, vol. 88(52), Eos, Transactions, AGU, abstract T21B-0583.

Ófeigsson, B. G., E. Sturkell, H. Ólafsson, F. Sigmundsson, P. Einarsson, and J. T. X. Búi (2007b), GPS network measurments in the Kárahnjúkar area 2006, *Tech. Rep. RH-15-2007*, Institution of Earth sciences, University of Iceland. URL `http://www.raunvis.hi.is/reports/2007/RH-15-2007.pdf`

Pagli, C., F. Sigmundsson, B. Lund, E. Sturkell, H. Geirsson, P. Einarsson, T. Árnadóttir, and S. Hreinsdóttir (2007), Glacio-isostatic deformation around Vatnajökull ice cap, Iceland, induced by recent climate warming: GPS observations and finite element modeling, *Journal of Geophysical Research*, *112*, B08405, doi:10.1029/2006JB004421.

Sella, G. F., T. H. Dixon, and A. Mao (2001), Revel: A model for recent plate velocities from space geodesy, *Journal of Geophysical Research*, *107*(B4), doi: 10.1029/2000JB000033.

Sigmundsson, F. (1991), Post-glacial rebound and asthenosphere viscosity in Iceland, *Geophysical Research Letters*, *18*(6), 1131 – 1134.

Sigmundsson, F. (2002), Greinargerð um landhæðarbreytingar vegna Hálslóns.

Sigmundsson, F. (2006), *Iceland Geodynamics, Crustal Deformation and Divergent Plate Tectonics*, Praxis Publiching-Springer Verlag, Chichester, UK, 209 pp.

Sigmundsson, F., and P. Einarsson (1992), Glacio-isostatic crustal movements caused by historical volume change of the Vatnajökull ice cap, Iceland, *Geophysical Research Letters*, *19*(21), 2123 – 2126.

Sigmundsson, F., P. Einarsson, P. Halldórsson, S. Jakobsdóttir, K. Vogfjörð, R. Sigbjörnsson, and J. Þór Snæbjörnsson (2005), Earthquakes and faults in the Kárahnjúkar area, *Review of hazard and recommended further studies LV-2005/027*, Landsvirkjun.

Sigurdsson, H., and R. S. J. Sparks (1978), Rifting episode in north Iceland in 1874-1875 and the eruptions of Askja and Sveinagja, *Bulletin of Volcanology*, *41*(3), 149 – 167, doi:10.1007/BF02597219.

Sigvaldason, G. E. (2002), Volcanic and tectonic processes coinciding with glaciation and crustal rebound: an early Holocene rhyolitic eruption in the Dyngjufjöll volcanic centre and the formation of the Askja caldera, north Iceland, *Bulletin of Volcanology*, *64*(3–4), 192 – 205, doi:10.1007/s00445-002-0204-7.

Sjöberg, L. E., M. Pan, S. Erlingsson, and E. Asenjo (2004), Land uplift near Vatnajökull, Iceland, as observed by GPS in 1992, 1996, 1999, *Geophysical Journal International*, *159*, 943 – 948.

Snæbjörnsson, J. T., C. A. Taylor, and R. Sigbjörnsson (2006), Kárahnjúkar hydroelectric project, hálslón area, *Assessment of crustal Strain and Fault Movements LV-2006/013*, Landsvirkjun.

Sturkell, E., and F. Sigmundsson (2000), Continuous deflation of the Askja caldera, Iceland, during the 1983-1998 noneruptive period, *Journal of Geophysical Research*, *105*, 25,671–25,684, doi:10.1029/2000JB900178.

Sturkell, E., P. Einarsson, F. Sigmundsson, H. Geirsson, H. Olafsson, R. Pedersen, E. de Zeeuw-van Dalfsen, A. T. Linde, S. I. Sacks, and R. Stefansson (2006a), Volcano geodesy and magma dynamics in Iceland, *Journal of Volcanology and Geothermal Research*, *150*(1–3), 14–34.

Sturkell, E., F. Sigmundsson, and R. Slunga (2006b), 1983-2003 decaying rate of deflation at Askja caldera: Pressure decrease in an extensive magma plumbing system at a spreading plate boundary., *Bulletin of Volcanology*, *68*(7–8), 727 – 735, doi:10.1007/s00445-005-0046-1.

Sæmundsson, K., and H. Jóhannesson (2005), Inspection of faults at Kárahnjúkar carried out in July and August 2005, *Tech. Rep. Report VÍ-ES-01*, ÍSOR Iceland Geosurvey.

Thorarinsson, S., and G. E. Sigvaldason (1962), The eruption in Askja, 1961; a preliminary report, *American Journal of Science*, *260*, 641 – 651.

Tómasson, H. (1976), The opening of tectonic fractures at the Landgalda dam, in *Douzième Congrès des Grands Barrages*, pp. 75 – 91, Commission International Des Grands Barrages, Mexico.

Appendix A

Station coordinates and velocities

A.1 Station coordinates

Table A.1: Coordinates in ITRF2005 reference system derived from the 2005 GPS-campaign with $1\,\sigma$ uncertainties.

Point	x [m]	σ_x [m]	y [m]	σ_y [m]	z [m]	σ_z [m]
ALFD	2599642.4105	0.0024	-747114.4912	0.0015	5757625.9241	0.0051
BALD	2609137.7057	0.0018	-735815.2559	0.0012	5754774.9932	0.0038
BUDI	2607056.1742	0.0020	-739780.1243	0.0012	5755226.3286	0.0044
BRUJ	2613994.9890	0.0013	-753921.4222	0.0010	5750376.6049	0.0026
DIMM	2606188.1926	0.0017	-736801.8468	0.0011	5755878.9323	0.0037
DSTI	2608084.2925	0.0019	-736217.2954	0.0011	5755184.4678	0.0039
FADA	2603338.1306	0.0020	-747675.8731	0.0013	5755930.8838	0.0041
GRUN	2582199.6489	0.0019	-718008.7960	0.0011	5769023.1484	0.0040
HAHV	2606002.8854	0.0018	-737864.5388	0.0011	5755967.2573	0.0036
HALS	2610918.2502	0.0017	-738682.6681	0.0010	5753663.2442	0.0035
HATU	2632703.4454	0.0021	-741354.5345	0.0015	5743624.6576	0.0045
HDAL	2605996.2825	0.0024	-725815.6587	0.0013	5757521.6741	0.0051
HEID	2579186.1714	0.0015	-668989.7864	0.0012	5775788.9691	0.0029
HLON	2612253.8526	0.0021	-743131.5782	0.0013	5752603.7477	0.0043
HRAU	2616052.2177	0.0018	-750701.0322	0.0012	5749819.5444	0.0038
HSTO	2607617.7239	0.0017	-744050.8141	0.0010	5754459.7219	0.0033
KARV	2607091.5869	0.0012	-739674.5561	0.0010	5755222.3425	0.0024
KRIN	2614404.6529	0.0019	-747730.4252	0.0013	5750927.8220	0.0039
KVAR	2613373.5200	0.0018	-752828.3913	0.0013	5750748.3545	0.0038
KVEA	2611373.6829	0.0019	-759806.2673	0.0013	5750688.0954	0.0040
LAFE	2618922.1551	0.0022	-721853.4305	0.0013	5752169.3645	0.0045
LAVE	2600325.4845	0.0016	-735996.7018	0.0010	5758748.2241	0.0033
MISA	2609037.2860	0.0020	-743264.0112	0.0011	5753856.4060	0.0044
MISV	2609019.9357	0.0020	-743275.9278	0.0011	5753857.6207	0.0043
NYSA	2620384.7983	0.0020	-737611.3283	0.0012	5749647.6150	0.0040
SADA	2606224.7324	0.0019	-741695.6208	0.0011	5755350.7859	0.0041
SAUD	2609938.8676	0.0014	-742658.4350	0.0011	5753603.3287	0.0028
SFEL	2608044.6761	0.0020	-737942.6627	0.0012	5755038.8277	0.0042
SHAL	2608894.0257	0.0020	-741836.1204	0.0011	5754125.9869	0.0042
SNES	2622807.0232	0.0020	-725652.7719	0.0012	5749893.2389	0.0042
SNSK	2621860.1239	0.0021	-734112.6940	0.0014	5749433.1370	0.0044
THMY	2612283.1525	0.0023	-746861.4380	0.0013	5752054.7045	0.0046
THUD	2614654.1034	0.0019	-730656.0315	0.0011	5753084.2771	0.0040
TROL	2611527.1488	0.0024	-745466.3210	0.0014	5752556.8728	0.0048
TUNG	2611307.7366	0.0015	-731586.2726	0.0009	5754376.8410	0.0030
VEOR	2615478.4342	0.0016	-740778.0601	0.0010	5751319.6361	0.0033
VEVO	2609155.0157	0.0018	-748772.9134	0.0012	5753233.2590	0.0038
VIKD	2592243.7109	0.0022	-740904.1555	0.0014	5761679.1001	0.0046

Table A.2: Coordinates in ITRF2005 reference system derived from the 2006 GPS-campaign with 1σ uncertainties.

Point	x [m]	σ_x [m]	y [m]	σ_y [m]	z [m]	σ_z [m]
ALFD	2599642.4102	0.0016	-747114.4822	0.0014	5757625.9601	0.0033
BALD	2609137.6967	0.0020	-735815.2452	0.0015	5754775.0065	0.0043
BUDI	2607056.1762	0.0020	-739780.1148	0.0015	5755226.3581	0.0042
BRUJ	2613994.9810	0.0016	-753921.4120	0.0013	5750376.6181	0.0033
DIMM	2606188.1922	0.0020	-736801.8342	0.0016	5755878.9496	0.0044
DSTI	2608084.3003	0.0021	-736217.2802	0.0015	5755184.4874	0.0043
FADA	2603338.1269	0.0016	-747675.8622	0.0014	5755930.9085	0.0033
GRUN	2582199.6423	0.0016	-718008.7897	0.0014	5769023.1658	0.0032
HAHV	2606002.8811	0.0015	-737864.5247	0.0013	5755967.2786	0.0030
HALS	2610918.2398	0.0017	-738682.6570	0.0014	5753663.2615	0.0035
HATU	2632703.4441	0.0019	-741354.5239	0.0015	5743624.6867	0.0040
HDAL	2605996.2839	0.0016	-725815.6498	0.0014	5757521.6995	0.0033
HEID	2579186.1558	0.0022	-668989.7748	0.0015	5775788.9686	0.0046
HLON	2612253.8396	0.0015	-743131.5666	0.0013	5752603.7589	0.0030
HRAU	2616052.2117	0.0018	-750701.0196	0.0014	5749819.5677	0.0037
HSTO	2607617.7235	0.0022	-744050.8025	0.0015	5754459.7584	0.0045
KARA	2607017.4184	0.0022	-736777.1519	0.0015	5755627.8192	0.0041
KARV	2607091.5778	0.0014	-739674.5447	0.0012	5755222.3549	0.0028
KRIN	2614404.6551	0.0022	-747730.4149	0.0016	5750927.8541	0.0045
KVAR	2613373.5161	0.0019	-752828.3753	0.0016	5750748.3880	0.0039
KVEA	2611373.6776	0.0020	-759806.2640	0.0016	5750688.1251	0.0040
LAFE	2618922.1488	0.0018	-721853.4184	0.0014	5752169.3896	0.0037
LAVE	2600325.4718	0.0019	-735996.6966	0.0015	5758748.2211	0.0040
MISA	2609037.2826	0.0017	-743264.0028	0.0014	5753856.4234	0.0035
MISV	2609019.9324	0.0022	-743275.9218	0.0016	5753857.6448	0.0046
NYSA	2620384.7934	0.0017	-737611.3143	0.0014	5749647.6373	0.0036
SADA	2606224.7227	0.0015	-741695.6103	0.0013	5755350.8042	0.0030
SAUD	2609938.8626	0.0018	-742658.4213	0.0014	5753603.3510	0.0037
SFEL	2608044.6765	0.0017	-737942.6472	0.0014	5755038.8453	0.0035
SHAL	2608894.0207	0.0017	-741836.1101	0.0014	5754126.0058	0.0035
SNES	2622807.0274	0.0017	-725652.7583	0.0014	5749893.2685	0.0036
SNSK	2621860.1162	0.0019	-734112.6809	0.0015	5749433.1537	0.0040
THMY	2612283.1508	0.0018	-746861.4252	0.0014	5752054.7342	0.0037
THUD	2614654.0928	0.0019	-730656.0171	0.0015	5753084.2818	0.0040
TROL	2611527.1440	0.0022	-745466.3072	0.0016	5752556.8883	0.0046
TUNG	2611307.7357	0.0019	-731586.2558	0.0015	5754376.8516	0.0040
VEOR	2615478.4316	0.0019	-740778.0488	0.0015	5751319.6590	0.0039
VEVO	2609155.0058	0.0017	-748772.8948	0.0015	5753233.2761	0.0035
VIKD	2592243.7134	0.0017	-740904.1464	0.0014	5761679.1374	0.0035

Table A.3: Coordinates in ITRF2005 reference system derived from the 2007 GPS-campaign with $1\,\sigma$ uncertainties.

Point	x [m]	σ_x [m]	y [m]	σ_y [m]	z [m]	σ_z [m]
ALFD	2599642.4105	0.0017	-747114.4648	0.0009	5757625.9773	0.0034
BALD	2609137.6931	0.0019	-735815.2254	0.0012	5754775.0186	0.0040
BUDI	2607056.1537	0.0018	-739780.1036	0.0011	5755226.3732	0.0037
BRUJ	2613994.9826	0.0011	-753921.3961	0.0007	5750376.6441	0.0023
DIMM	2606188.1604	0.0018	-736801.8220	0.0012	5755878.9715	0.0042
DSTI	2608084.2945	0.0012	-736217.2599	0.0008	5755184.4935	0.0025
FADA	2603338.1209	0.0015	-747675.8421	0.0008	5755930.9273	0.0031
GRUN	2582199.6260	0.0016	-718008.7753	0.0009	5769023.1640	0.0034
HAHV	2606002.8535	0.0013	-737864.5133	0.0008	5755967.2992	0.0025
HALS	2610918.2272	0.0020	-738682.6348	0.0012	5753663.2661	0.0040
HATU	2632703.4253	0.0015	-741354.5056	0.0009	5743624.6783	0.0032
HDAL	2605996.2816	0.0016	-725815.6373	0.0009	5757521.7134	0.0033
HLON	2612253.8470	0.0018	-743131.5450	0.0011	5752603.7678	0.0039
HRAU	2616052.2129	0.0017	-750701.0018	0.0010	5749819.6044	0.0035
HSTO	2607617.7092	0.0015	-744050.7776	0.0010	5754459.7527	0.0032
KARA	2607017.4217	0.0015	-736777.1275	0.0008	5755627.8415	0.0027
KARV	2607091.5550	0.0011	-739674.5365	0.0007	5755222.3670	0.0022
KRIN	2614404.6503	0.0018	-747730.3947	0.0011	5750927.8816	0.0039
KVAR	2613373.5170	0.0015	-752828.3554	0.0011	5750748.4160	0.0032
KVEA	2611373.6862	0.0016	-759806.2436	0.0011	5750688.1693	0.0033
LAFE	2618922.1454	0.0015	-721853.4025	0.0009	5752169.4051	0.0031
LAVE	2600325.4608	0.0016	-735996.6834	0.0009	5758748.2382	0.0034
MISA	2609037.2717	0.0017	-743263.9751	0.0011	5753856.4390	0.0036
MISV	2609019.9269	0.0018	-743275.8946	0.0012	5753857.6656	0.0039
NYSA	2620384.7925	0.0016	-737611.2977	0.0009	5749647.6611	0.0034
SADA	2606224.7149	0.0015	-741695.5924	0.0010	5755350.8244	0.0031
SAUD	2609938.8527	0.0011	-742658.4032	0.0007	5753603.3578	0.0022
SFEL	2608044.6931	0.0018	-737942.6297	0.0011	5755038.8705	0.0036
SHAL	2608894.0107	0.0018	-741836.0912	0.0011	5754126.0127	0.0038
SNES	2622807.0102	0.0016	-725652.7414	0.0009	5749893.2676	0.0034
SNSK	2621860.1056	0.0014	-734112.6609	0.0008	5749433.1731	0.0029
THMY	2612283.1390	0.0018	-746861.3991	0.0011	5752054.7414	0.0037
THUD	2614654.0811	0.0016	-730656.0020	0.0009	5753084.2968	0.0034
TROL	2611527.1335	0.0019	-745466.2823	0.0012	5752556.9146	0.0040
TUNG	2611307.7204	0.0017	-731586.2395	0.0009	5754376.8615	0.0034
VEOR	2615478.4118	0.0015	-740778.0295	0.0009	5751319.6631	0.0032
VEVO	2609155.0082	0.0017	-748772.8659	0.0011	5753233.3095	0.0036
VIKD	2592243.6952	0.0017	-740904.1298	0.0010	5761679.1455	0.0035

A.2 Station velocities

Table A.4: Velocities relative to the ITRF2005 reference frame, 2005-2006 with 1σ uncertainties.

			Velocities mm/yr		
Station	Long	Lat	East	North	Up
ALFD	-16.0342	64.9841	8.8 ±1.3	18.2±1.4	30.4±4.4
BALD	-15.7492	64.9243	9.0 ±1.1	16.7±1.2	7.9 ±3.7
BRUJ	-16.0885	64.8293	8.9 ±0.6	17.1±0.5	8.5 ±1.6
BUDI	-15.8419	64.9335	10.6±1.2	14.0±1.1	28.5±3.5
DIMM	-15.7863	64.9493	12.9±1.3	11.1±1.1	15.7±3.7
DSTI	-15.7635	64.9332	17.9±1.2	5.5 ±1.0	20.4±3.5
FADA	-16.0240	64.9476	9.7 ±1.3	17.6±1.1	18.9±3.6
GRUN	-15.5392	65.2281	4.5 ±1.3	15.3±1.2	13.1±4.1
HAHV	-15.8090	64.9488	13.4±1.4	17.0±1.0	17.1±3.3
HALS	-15.7973	64.8998	8.5 ±1.2	20.4±1.1	10.5±3.4
HATT	-16.0111	64.9237	11.0±1.4	12.5±1.1	30.6±3.3
HATU	-15.7269	64.6854	10.8±1.5	16.7±1.2	25.3±3.8
HDAL	-15.5635	64.9812	9.5 ±1.3	12.2±1.4	23.7±4.7
HEBL	-16.2098	65.1800	7.7 ±0.7	21.1±0.7	34.7±2.1
HEID	-14.5409	65.3808	7.7 ±0.4	16.3±0.3	-7.1±0.9
HLON	-15.8799	64.8755	7.9 ±1.4	19.8±1.3	3.6 ±4.2
HRAU	-16.0113	64.8183	11.6±1.2	19.0±1.0	16.8±3.6
HSTO	-15.9254	64.9167	12.3±1.1	19.3±1.1	32.5±3.3
HVAN	-16.3857	64.8064	9.7 ±1.3	20.7±1.1	32.0±4.0
KARV	-15.8395	64.9334	9.9 ±0.5	17.9±0.3	7.2 ±0.9
KREP	-16.1712	65.0990	6.7 ±1.3	19.0±1.1	14.7±3.7
KRET	-16.2780	64.9425	10.2±1.3	17.0±1.1	32.5±3.6
KRIN	-15.9607	64.8420	11.6±1.2	15.3±1.2	28.2±3.7
KVAR	-16.0700	64.8380	15.0±1.2	22.6±1.1	27.3±3.2
KVEA	-16.2229	64.8376	2.5 ±1.1	18.5±1.1	26.4±3.3
KVER	-16.6519	64.7454	11.4±1.4	20.0±1.2	28.3±4.1
LAFE	-15.4098	64.8683	10.5±1.2	19.6±1.2	19.9±3.7
LAVE	-15.8036	65.0078	2.3 ±1.1	11.5±1.0	-8.2±3.1
LIND	-16.3111	64.8817	7.8 ±0.8	20.1±0.7	24.7±2.1
MISA	-15.9012	64.9051	8.2 ±1.1	13.1±1.0	14.3±3.5
MISV	-15.9016	64.9052	5.8 ±1.1	15.7±1.1	20.8±3.7
NYSA	-15.7214	64.8129	13.3±1.3	17.5±1.1	17.7±3.7
SADA	-15.8856	64.9362	8.1 ±1.4	19.9±1.2	10.7±3.4
SAUD	-15.8837	64.8984	12.6±0.4	18.1±0.2	17.7±0.8
SFEL	-15.7988	64.9291	15.8±1.1	11.5±1.1	15.7±3.3
SHAL	-15.8730	64.9104	9.0 ±1.1	15.7±1.1	14.7±3.6
SNES	-15.4652	64.8210	14.4±1.4	12.8±1.3	29.0±4.1
SNSK	-15.6421	64.8082	11.4±1.5	17.7±1.2	10.8±4.0
THMY	-15.9554	64.8648	12.3±1.3	18.3±1.4	26.0±4.8
THUD	-15.6128	64.8860	12.5±1.3	15.5±1.2	-0.8±3.8
TROL	-15.9315	64.8758	12.3±1.3	15.2±1.5	10.1±5.1
TUNG	-15.6508	64.9151	16.7±1.3	9.9 ±1.1	8.0 ±3.1
VEOR	-15.8136	64.8506	11.1±1.1	15.4±1.0	20.1±3.2
VEVO	-16.0124	64.8895	16.7±1.1	21.3±1.0	9.9 ±3.4
VIKD	-15.9508	65.0712	9.7 ±1.4	16.3±1.4	34.8±4.5

Table A.5: Velocities relative to the Eurasian Plate, 2005-2006 with 1σ uncertainties.

			Velocities mm/yr		
Station	Long	Lat	East	North	Up
ALFD	-16.0342	64.9841	-1.3±1.3	1.9 ±1.4	30.4±4.4
BALD	-15.7492	64.9243	-1.3±1.1	0.4 ±1.2	7.9 ±3.7
BRUJ	-16.0885	64.8293	-1.3±0.6	0.7 ±0.5	8.5 ±1.6
BUDI	-15.8419	64.9335	0.4 ±1.2	-2.3 ±1.1	28.5±3.5
DIMM	-15.7863	64.9493	2.6 ±1.3	-5.2 ±1.1	15.7±3.7
DSTI	-15.7635	64.9332	7.6 ±1.2	-10.8±1.0	20.4±3.5
FADA	-16.0240	64.9476	-0.5±1.3	1.3 ±1.1	18.9±3.6
GRUN	-15.5392	65.2281	-5.7±1.3	-1.0 ±1.2	13.1±4.1
HAHV	-15.8090	64.9488	3.2 ±1.4	0.6 ±1.0	17.1±3.3
HALS	-15.7973	64.8998	-1.8±1.2	4.0 ±1.1	10.5±3.4
HATT	-16.0111	64.9237	0.8 ±1.4	-3.9 ±1.1	30.6±3.3
HATU	-15.7269	64.6854	0.5 ±1.5	0.3 ±1.2	25.3±3.8
HDAL	-15.5635	64.9812	-0.8±1.3	-4.1 ±1.4	23.7±4.7
HEBL	-16.2098	65.1800	-2.3±0.7	4.8 ±0.7	34.7±2.1
HEID	-14.5409	65.3808	-2.7±0.4	0.0 ±0.3	-7.1±0.9
HLON	-15.8799	64.8755	-2.3±1.4	3.5 ±1.3	3.6 ±4.2
HRAU	-16.0113	64.8183	1.3 ±1.2	2.7 ±1.0	16.8±3.6
HSTO	-15.9254	64.9167	2.1 ±1.1	2.9 ±1.1	32.5±3.3
HVAN	-16.3857	64.8064	-0.4±1.3	4.4 ±1.1	32.0±4.0
KARV	-15.8395	64.9334	-0.3±0.5	1.6 ±0.3	7.2 ±0.9
KREP	-16.1712	65.0990	-3.4±1.3	2.6 ±1.1	14.7±3.7
KRET	-16.2780	64.9425	0.0 ±1.3	0.6 ±1.1	32.5±3.6
KRIN	-15.9607	64.8420	1.4 ±1.2	-1.0 ±1.2	28.2±3.7
KVAR	-16.0700	64.8380	4.8 ±1.2	6.2 ±1.1	27.3±3.2
KVEA	-16.2229	64.8376	-7.7±1.1	2.1 ±1.1	26.4±3.3
KVER	-16.6519	64.7454	1.3 ±1.4	3.6 ±1.2	28.3±4.1
LAFE	-15.4098	64.8683	0.1 ±1.2	3.2 ±1.2	19.9±3.7
LAVE	-15.8036	65.0078	-7.9±1.1	-4.9 ±1.0	-8.2±3.1
LIND	-16.3111	64.8817	-2.3±0.8	3.7 ±0.7	24.7±2.1
MISA	-15.9012	64.9051	-2.1±1.1	-3.2 ±1.0	14.3±3.5
MISV	-15.9016	64.9052	-4.4±1.1	-0.7 ±1.1	20.8±3.7
NYSA	-15.7214	64.8129	3.0 ±1.3	1.2 ±1.1	17.7±3.7
SADA	-15.8856	64.9362	-2.1±1.4	3.5 ±1.2	10.7±3.4
SAUD	-15.8837	64.8984	2.4 ±0.4	1.7 ±0.2	17.7±0.8
SFEL	-15.7988	64.9291	5.6 ±1.1	-4.9 ±1.1	15.7±3.3
SHAL	-15.8730	64.9104	-1.2±1.1	-0.6 ±1.1	14.7±3.6
SNES	-15.4652	64.8210	4.0 ±1.4	-3.6 ±1.3	29.0±4.1
SNSK	-15.6421	64.8082	1.1 ±1.5	1.4 ±1.2	10.8±4.0
THMY	-15.9554	64.8648	2.1 ±1.3	1.9 ±1.4	26.0±4.8
THUD	-15.6128	64.8860	2.2 ±1.3	-0.9 ±1.2	-0.8 ±3.8
TROL	-15.9315	64.8758	2.1 ±1.3	-1.2 ±1.5	10.1±5.1
TUNG	-15.6508	64.9151	6.5 ±1.3	-6.4 ±1.1	8.0 ±3.1
VEOR	-15.8136	64.8506	0.8 ±1.1	-0.9 ±1.0	20.1±3.2
VEVO	-16.0124	64.8895	6.5 ±1.1	4.9 ±1.0	9.9 ±3.4
VIKD	-15.9508	65.0712	-0.5±1.4	-0.0 ±1.4	34.8±4.5

Table A.6: Velocities relative to the ITRF2005 reference frame, 2006-2007 with 1σ uncertainties.

			Velocities mm/yr		
Station	Long	Lat	East	North	Up
ALFD	-16.0342	64.9841	17.7±1.2	11.3±1.3	14.3 ±4.0
BALD	-15.7492	64.9243	18.5±1.2	13.2±1.2	6.2 ±3.9
BRUJ	-16.0885	64.8293	16.0±0.4	13.6±0.4	22.6 ±1.2
BUDI	-15.8419	64.9335	4.5 ±1.3	28.0±1.1	3.4 ±3.5
DIMM	-15.7863	64.9493	2.2 ±1.3	39.1±1.1	4.3 ±3.5
DSTI	-15.7635	64.9332	18.2±1.0	12.9±0.9	0.1 ±2.8
FADA	-16.0240	64.9476	18.2±1.0	17.9±1.0	12.8 ±3.4
GRUN	-15.5392	65.2281	10.1±1.1	17.2±1.1	-8.9 ±3.8
HAHV	-15.8090	64.9488	3.5 ±1.2	36.7±0.9	6.2 ±3.0
HALS	-15.7973	64.8998	18.5±1.2	17.4±1.2	-0.5 ±3.6
HATT	-16.0111	64.9237	22.4±1.2	19.6±0.9	-12.2±2.7
HATU	-15.7269	64.6854	12.4±1.3	17.1±1.1	-17.4±3.4
HDAL	-15.5635	64.9812	11.6±1.1	10.9±1.3	10.4 ±4.1
HEBL	-16.2098	65.1800	9.1 ±0.9	21.3±0.8	-28.2±2.8
HLON	-15.8799	64.8755	22.2±1.2	3.0 ±1.1	8.1 ±3.8
HRAU	-16.0113	64.8183	16.4±1.0	18.3±1.0	30.5 ±3.2
HSTO	-15.9254	64.9167	19.4±1.1	16.2±1.0	-13.1±3.1
HVAN	-16.3857	64.8064	4.9 ±1.5	17.0±1.2	26.8 ±4.2
KARA	-15.7810	64.9420	25.2±1.1	12.2±1.0	20.4 ±3.0
KARV	-15.8395	64.9334	1.8 ±0.3	27.6±0.2	0.6 ±0.7
KREP	-16.1712	65.0990	7.9 ±1.4	22.9±1.1	7.0 ±3.9
KRET	-16.2780	64.9425	11.6±1.4	14.3±1.2	22.1 ±3.8
KRIN	-15.9607	64.8420	17.3±1.1	20.1±1.1	20.4 ±3.5
KVAR	-16.0700	64.8380	17.9±1.1	15.4±1.0	22.8 ±3.0
KVEA	-16.2229	64.8376	21.3±1.1	16.2±1.0	38.8 ±3.0
KVER	-16.6519	64.7454	5.4 ±1.4	22.7±1.1	18.9 ±3.9
LAFE	-15.4098	64.8683	14.2±0.9	13.5±1.0	10.0 ±3.3
LAVE	-15.8036	65.0078	10.1±1.1	20.1±0.9	10.2 ±3.0
MISA	-15.9012	64.9051	23.0±1.1	22.5±1.1	5.8 ±3.5
MISV	-15.9016	64.9052	23.9±1.2	19.6±1.2	12.2 ±3.7
NYSA	-15.7214	64.8129	16.0±1.2	14.5±1.0	18.7 ±3.4
SADA	-15.8856	64.9362	14.6±1.2	19.6±1.0	12.7 ±3.0
SAUD	-15.8837	64.8984	15.0±0.4	16.1±0.3	0.4 ±0.8
SFEL	-15.7988	64.9291	20.8±1.0	0.4 ±1.0	25.2 ±3.0
SHAL	-15.8730	64.9104	15.0±1.0	16.0±1.0	-0.5 ±3.1
SNES	-15.4652	64.8210	11.9±1.3	17.8±1.1	-9.3 ±3.7
SNSK	-15.6421	64.8082	17.2±1.3	21.9±1.1	11.9 ±3.6
THMY	-15.9554	64.8648	21.2±1.3	19.3±1.4	-0.3 ±4.7
THUD	-15.6128	64.8860	11.3±1.2	20.2±1.1	9.4 ±3.5
TROL	-15.9315	64.8758	20.6±1.3	25.0±1.6	16.3 ±5.2
TUNG	-15.6508	64.9151	11.4±1.2	21.1±1.0	1.5 ±3.0
VEOR	-15.8136	64.8506	13.3±1.3	23.8±1.4	-7.3 ±4.2
VEVO	-16.0124	64.8895	27.8±1.1	18.8±1.1	25.6 ±3.5
VIKD	-15.9508	65.0712	11.7±1.3	23.4±1.3	-1.2 ±4.3

Table A.7: Velocities relative to the Eurasian Plate, 2006-2007 with $1\,\sigma$ uncertainties.

			Velocities mm/yr		
Station	Long	Lat	East	North	Up
ALFD	-16.0342	64.9841	7.6 ±1.2	-5.1 ±1.3	14.3 ±4.0
BALD	-15.7492	64.9243	8.2 ±1.2	-3.2 ±1.2	6.2 ±3.9
BRUJ	-16.0885	64.8293	5.8 ±0.4	-2.8 ±0.4	22.6 ±1.2
BUDI	-15.8419	64.9335	-5.7±1.3	11.6 ±1.1	3.4 ±3.5
DIMM	-15.7863	64.9493	-8.1±1.3	22.8 ±1.1	4.3 ±3.5
DSTI	-15.7635	64.9332	7.9 ±1.0	-3.4 ±0.9	0.1 ±2.8
FADA	-16.0240	64.9476	8.0 ±1.0	1.6 ±1.0	12.8 ±3.4
GRUN	-15.5392	65.2281	-0.1±1.1	0.8 ±1.1	-8.9 ±3.8
HAHV	-15.8090	64.9488	-6.7±1.2	20.4 ±0.9	6.2 ±3.0
HALS	-15.7973	64.8998	8.3 ±1.2	1.1 ±1.2	-0.5 ±3.6
HATT	-16.0111	64.9237	12.2±1.2	3.3 ±0.9	-12.2±2.7
HATU	-15.7269	64.6854	2.1 ±1.3	0.7 ±1.1	-17.4±3.4
HDAL	-15.5635	64.9812	1.4 ±1.1	-5.4 ±1.3	10.4 ±4.1
HEBL	-16.2098	65.1800	-0.9 ±0.9	5.0 ±0.8	-28.2±2.8
HLON	-15.8799	64.8755	12.0±1.2	-13.3±1.1	8.1 ±3.8
HRAU	-16.0113	64.8183	6.2 ±1.0	1.9 ±1.0	30.5 ±3.2
HSTO	-15.9254	64.9167	9.2 ±1.1	-0.2 ±1.0	-13.1±3.1
HVAN	-16.3857	64.8064	-5.3±1.5	0.7 ±1.2	26.8 ±4.2
KARA	-15.7810	64.9420	14.9±1.1	-4.2 ±1.0	20.4 ±3.0
KARV	-15.8395	64.9334	-8.4±0.3	11.2 ±0.2	0.6 ±0.7
KREP	-16.1712	65.0990	-2.2±1.4	6.5 ±1.1	7.0 ±3.9
KRET	-16.2780	64.9425	1.5 ±1.4	-2.1 ±1.2	22.1 ±3.8
KRIN	-15.9607	64.8420	7.1 ±1.1	3.7 ±1.1	20.4 ±3.5
KVAR	-16.0700	64.8380	7.7 ±1.1	-0.9 ±1.0	22.8 ±3.0
KVEA	-16.2229	64.8376	11.1±1.1	-0.1 ±1.0	38.8 ±3.0
KVER	-16.6519	64.7454	-4.7±1.4	6.4 ±1.1	18.9 ±3.9
LAFE	-15.4098	64.8683	3.9 ±0.9	-2.9 ±1.0	10.0 ±3.3
LAVE	-15.8036	65.0078	-0.1±1.1	3.7 ±0.9	10.2 ±3.0
MISA	-15.9012	64.9051	12.8±1.1	6.2 ±1.1	5.8 ±3.5
MISV	-15.9016	64.9052	13.7±1.2	3.3 ±1.2	12.2 ±3.7
NYSA	-15.7214	64.8129	5.7 ±1.2	-1.8 ±1.0	18.7 ±3.4
SADA	-15.8856	64.9362	4.4 ±1.2	3.2 ±1.0	12.7 ±3.0
SAUD	-15.8837	64.8984	4.8 ±0.4	-0.3 ±0.3	0.4 ±0.8
SFEL	-15.7988	64.9291	10.6±1.0	-15.9±1.0	25.2 ±3.0
SHAL	-15.8730	64.9104	4.8 ±1.0	-0.4 ±1.0	-0.5 ±3.1
SNES	-15.4652	64.8210	1.6 ±1.3	1.5 ±1.1	-9.3 ±3.7
SNSK	-15.6421	64.8082	6.9 ±1.3	5.6 ±1.1	11.9 ±3.6
THMY	-15.9554	64.8648	11.0±1.3	2.9 ±1.4	-0.3 ±4.7
THUD	-15.6128	64.8860	1.0 ±1.2	3.9 ±1.1	9.4 ±3.5
TROL	-15.9315	64.8758	10.4±1.3	8.6 ±1.6	16.3 ±5.2
TUNG	-15.6508	64.9151	1.1 ±1.2	4.7 ±1.0	1.5 ±3.0
VEOR	-15.8136	64.8506	3.0 ±1.3	7.4 ±1.4	-7.3 ±4.2
VEVO	-16.0124	64.8895	17.6±1.1	2.5 ±1.1	25.6 ±3.5
VIKD	-15.9508	65.0712	1.5 ±1.3	7.1 ±1.3	-1.2 ±4.3

Table A.8: velocities relative to the ITRF2005 reference frame, 2005-2007 with 1σ uncertainties.

			Velocities mm/yr		
Station	Long	Lat	East	North	Up
ALFD	-16.0342	64.9841	13.3±0.6	14.6±0.7	21.8±2.1
BALD	-15.7492	64.9243	13.6±0.5	15.0±0.6	7.0 ±2.0
BRUJ	-16.0885	64.8293	13.1±0.3	15.0±0.2	16.7±0.7
BUDI	-15.8419	64.9335	7.8 ±0.6	21.0±0.6	15.8±1.8
DIMM	-15.7863	64.9493	7.3 ±0.5	25.2±0.5	9.9 ±1.5
DSTI	-15.7635	64.9332	18.0±0.4	9.6 ±0.4	8.9 ±1.3
FADA	-16.0240	64.9476	14.4±0.5	17.8±0.5	15.7±1.8
GRUN	-15.5392	65.2281	7.6 ±0.5	16.3±0.6	1.5 ±2.0
HAHV	-15.8090	64.9488	8.2 ±0.5	27.6±0.5	11.3±1.4
HALS	-15.7973	64.8998	13.5±0.6	19.0±0.6	5.2 ±1.8
HATT	-16.0111	64.9237	17.1±0.7	16.5±0.5	6.0 ±1.6
HATU	-15.7269	64.6854	11.7±0.7	16.9±0.5	2.4 ±1.8
HDAL	-15.5635	64.9812	10.7±0.6	11.5±0.7	16.4±2.3
HEBL	-16.2098	65.1800	8.3 ±0.3	21.2±0.3	8.8 ±1.1
HEID	-14.5409	65.3808	7.7 ±0.4	16.3±0.3	-7.1±0.9
HLON	-15.8799	64.8755	15.8±0.5	10.4±0.6	6.0 ±1.9
HRAU	-16.0113	64.8183	14.2±0.5	18.7±0.5	24.1±1.7
HSTO	-15.9254	64.9167	16.0±0.5	17.7±0.5	8.7 ±1.5
HVAN	-16.3857	64.8064	7.5 ±0.7	19.0±0.6	29.5±2.1
KARA	-15.7810	64.9420	25.2±1.1	12.2±1.0	20.4±3.0
KARV	-15.8395	64.9334	4.7 ±0.2	23.8±0.1	3.1 ±0.4
KREP	-16.1712	65.0990	7.2 ±0.6	20.9±0.5	11.0±1.7
KRET	-16.2780	64.9425	10.8±0.6	15.7±0.5	27.5±1.6
KRIN	-15.9607	64.8420	14.6±0.5	17.8±0.5	24.1±1.8
KVAR	-16.0700	64.8380	16.5±0.5	18.9±0.5	24.9±1.5
KVEA	-16.2229	64.8376	11.9±0.5	17.3±0.5	32.9±1.6
KVER	-16.6519	64.7454	8.4 ±0.6	21.4±0.5	23.5±1.8
LAFE	-15.4098	64.8683	12.7±0.5	16.1±0.6	14.6±1.9
LAVE	-15.8036	65.0078	6.4 ±0.4	16.1±0.5	1.3 ±1.5
LIND	-16.3111	64.8817	7.8 ±0.8	20.1±0.7	24.7±2.1
MISA	-15.9012	64.9051	15.8±0.5	17.7±0.6	10.0±1.9
MISV	-15.9016	64.9052	14.7±0.5	17.6±0.6	16.5±1.9
NYSA	-15.7214	64.8129	14.8±0.6	16.0±0.5	18.2±1.7
SADA	-15.8856	64.9362	11.6±0.5	19.7±0.5	11.8±1.4
SAUD	-15.8837	64.8984	13.7±0.1	17.0±0.1	9.3 ±0.3
SFEL	-15.7988	64.9291	18.4±0.4	5.5 ±0.5	20.7±1.6
SHAL	-15.8730	64.9104	12.1±0.4	15.9±0.5	6.4 ±1.7
SNES	-15.4652	64.8210	13.1±0.6	15.5±0.6	8.8 ±2.0
SNSK	-15.6421	64.8082	14.6±0.7	20.0±0.5	11.4±1.8
THMY	-15.9554	64.8648	16.7±0.7	18.8±0.8	12.7±2.5
THUD	-15.6128	64.8860	11.9±0.4	17.9±0.5	4.6 ±1.6
TROL	-15.9315	64.8758	16.3±0.7	19.9±0.8	13.2±2.7
TUNG	-15.6508	64.9151	14.0±0.4	15.7±0.4	4.7 ±1.2
VEOR	-15.8136	64.8506	12.1±0.6	18.7±0.7	9.2 ±2.0
VEVO	-16.0124	64.8895	22.3±0.5	20.1±0.5	17.5±1.8
VIKD	-15.9508	65.0712	10.7±0.6	20.0±0.7	16.4±2.2

Table A.9: Velocities relative to the Eurasian Plate, 2005-2007 with $1\,\sigma$ uncertainties.

			Velocities mm/yr		
Station	Long	Lat	East	North	Up
ALFD	-16.0342	64.9841	3.2 ±0.6	-1.7 ±0.7	21.8±2.1
BALD	-15.7492	64.9243	3.4 ±0.5	-1.3 ±0.6	7.0 ±2.0
BRUJ	-16.0885	64.8293	2.9 ±0.3	-1.4 ±0.2	16.7±0.7
BUDI	-15.8419	64.9335	-2.4 ±0.6	4.7 ±0.6	15.8±1.8
DIMM	-15.7863	64.9493	-2.9 ±0.5	8.8 ±0.5	9.9 ±1.5
DSTI	-15.7635	64.9332	7.8 ±0.4	-6.7 ±0.4	8.9 ±1.3
FADA	-16.0240	64.9476	4.2 ±0.5	1.4 ±0.5	15.7±1.8
GRUN	-15.5392	65.2281	-2.6 ±0.5	-0.0 ±0.6	1.5 ±2.0
HAHV	-15.8090	64.9488	-2.0 ±0.5	11.2 ±0.5	11.3±1.4
HALS	-15.7973	64.8998	3.3 ±0.6	2.6 ±0.6	5.2 ±1.8
HATT	-16.0111	64.9237	6.9 ±0.7	0.2 ±0.5	6.0 ±1.6
HATU	-15.7269	64.6854	1.3 ±0.7	0.5 ±0.5	2.4 ±1.8
HDAL	-15.5635	64.9812	0.4 ±0.6	-4.8 ±0.7	16.4±2.3
HEBL	-16.2098	65.1800	-1.7 ±0.3	4.9 ±0.3	8.8 ±1.1
HEID	-14.5409	65.3808	-2.7 ±0.4	0.0 ±0.3	-7.1±0.9
HLON	-15.8799	64.8755	5.6 ±0.5	-6.0 ±0.6	6.0 ±1.9
HRAU	-16.0113	64.8183	4.0 ±0.5	2.3 ±0.5	24.1±1.7
HSTO	-15.9254	64.9167	5.8 ±0.5	1.3 ±0.5	8.7 ±1.5
HVAN	-16.3857	64.8064	-2.7 ±0.7	2.6 ±0.6	29.5±2.1
KARA	-15.7810	64.9420	14.9 ±1.1	-4.2 ±1.0	20.4±3.0
KARV	-15.8395	64.9334	-5.5 ±0.2	7.5 ±0.1	3.1 ±0.4
KREP	-16.1712	65.0990	-2.9 ±0.6	4.5 ±0.5	11.0±1.7
KRET	-16.2780	64.9425	0.7 ±0.6	-0.6 ±0.5	27.5±1.6
KRIN	-15.9607	64.8420	4.4 ±0.5	1.4 ±0.5	24.1±1.8
KVAR	-16.0700	64.8380	6.3 ±0.5	2.5 ±0.5	24.9±1.5
KVEA	-16.2229	64.8376	1.8 ±0.5	0.9 ±0.5	32.9±1.6
KVER	-16.6519	64.7454	-1.7 ±0.6	5.0 ±0.5	23.5±1.8
LAFE	-15.4098	64.8683	2.3 ±0.5	-0.3 ±0.6	14.6±1.9
LAVE	-15.8036	65.0078	-3.9 ±0.4	-0.3 ±0.5	1.3 ±1.5
LIND	-16.3111	64.8817	-2.3 ±0.8	3.7 ±0.7	24.7±2.1
MISA	-15.9012	64.9051	5.6 ±0.5	1.4 ±0.6	10.0±1.9
MISV	-15.9016	64.9052	4.4 ±0.5	1.3 ±0.6	16.5±1.9
NYSA	-15.7214	64.8129	4.5 ±0.6	-0.4 ±0.5	18.2±1.7
REYK	-21.9555	64.1388	-19.9±0.1	2.6 ±0.1	-0.1±0.3
SADA	-15.8856	64.9362	1.4 ±0.5	3.4 ±0.5	11.8±1.4
SAUD	-15.8837	64.8984	3.4 ±0.1	0.7 ±0.1	9.3 ±0.3
SFEL	-15.7988	64.9291	8.2 ±0.4	-10.9±0.5	20.7±1.6
SHAL	-15.8730	64.9104	1.9 ±0.4	-0.5 ±0.5	6.4 ±1.7
SNES	-15.4652	64.8210	2.7 ±0.6	-0.8 ±0.6	8.8 ±2.0
SNSK	-15.6421	64.8082	4.3 ±0.7	3.6 ±0.5	11.4±1.8
THMY	-15.9554	64.8648	6.4 ±0.7	2.4 ±0.8	12.7±2.5
THUD	-15.6128	64.8860	1.6 ±0.4	1.6 ±0.5	4.6 ±1.6
TROL	-15.9315	64.8758	6.1 ±0.7	3.6 ±0.8	13.2±2.7
TUNG	-15.6508	64.9151	3.7 ±0.4	-0.6 ±0.4	4.7 ±1.2
VEOR	-15.8136	64.8506	1.8 ±0.6	2.3 ±0.7	9.2 ±2.0
VEVO	-16.0124	64.8895	12.1 ±0.5	3.7 ±0.5	17.5±1.8
VIKD	-15.9508	65.0712	0.6 ±0.6	3.6 ±0.7	16.4±2.2

A.3 Estimated displacements

Table A.10: Displacements as derived from equation 4.4 and uncertainties from equation 4.4.

			displacements mm		
Station	Long	Lat	East	North	Up
ALFD	-16.0342	64.9841	8.8 ±1.7	-6.9 ±1.9	-16.0± 5.8
BALD	-15.7492	64.9243	9.8 ±1.6	-3.7 ±1.7	-1.8 ± 5.4
BRUJ	-16.0885	64.8293	7.3 ±0.7	-3.6 ±0.6	14.3 ± 2.0
BUDI	-15.8419	64.9335	-6.2 ±1.8	14.4 ±1.5	-25.9± 4.9
DIMM	-15.7863	64.9493	-11.0±1.8	28.7 ±1.5	-11.6± 5.0
DSTI	-15.7635	64.9332	0.3 ±1.5	7.3 ±1.3	-19.9± 4.3
FADA	-16.0240	64.9476	8.4 ±1.6	0.3 ±1.5	-6.1 ± 4.9
GRUN	-15.5392	65.2281	5.5 ±1.6	1.8 ±1.5	-21.8± 5.4
HAHV	-15.8090	64.9488	-9.7 ±1.8	19.3 ±1.3	-10.7± 4.3
HALS	-15.7973	64.8998	10.4 ±1.7	-3.0 ±1.6	-11.4± 4.9
HATT	-16.0111	64.9237	11.5 ±1.8	7.2 ±1.4	-43.2± 4.3
HATU	-15.7269	64.6854	1.6 ±2.0	0.4 ±1.6	-43.2± 5.1
HDAL	-15.5635	64.9812	2.1 ±1.7	-1.3 ±1.9	-13.3± 6.1
HEBL	-16.2098	65.1800	1.4 ±1.2	0.2 ±1.1	-61.7± 3.5
HEID	-14.5409	65.3808	1.1 ±6.6	1.4 ±5.6	-2.6 ±18.4
HLON	-15.8799	64.8755	14.9 ±1.9	-17.5±1.7	4.7 ± 5.7
HRAU	-16.0113	64.8183	5.1 ±1.6	-0.8 ±1.4	14.2 ± 4.8
HSTO	-15.9254	64.9167	7.3 ±1.5	-3.2 ±1.4	-46.7± 4.5
HVAN	-16.3857	64.8064	-4.7 ±1.9	-3.6 ±1.6	-5.2 ± 5.7
KARV	-15.8395	64.9334	-8.2 ±0.6	9.7 ±0.4	-6.8 ± 1.1
KREP	-16.1712	65.0990	1.2 ±1.9	3.9 ±1.5	-7.6 ± 5.3
KRET	-16.2780	64.9425	1.4 ±1.9	-2.6 ±1.6	-10.2± 5.2
KRIN	-15.9607	64.8420	5.9 ±1.6	4.9 ±1.6	-8.1 ± 5.1
KVAR	-16.0700	64.8380	3.0 ±1.6	-7.4 ±1.4	-4.5 ± 4.3
KVEA	-16.2229	64.8376	19.3 ±1.6	-2.3 ±1.4	12.6 ± 4.5
KVER	-16.6519	64.7454	-5.8 ±1.9	2.7 ±1.6	-9.1 ± 5.5
LAFE	-15.4098	64.8683	3.8 ±1.5	-6.3 ±1.5	-10.1± 4.9
LAVE	-15.8036	65.0078	7.7 ±1.5	8.5 ±1.3	18.2 ± 4.2
MISA	-15.9012	64.9051	15.3 ±1.6	9.7 ±1.5	-8.7 ± 4.9
MISV	-15.9016	64.9052	18.6 ±1.6	4.0 ±1.6	-8.8 ± 5.2
NYSA	-15.7214	64.8129	2.7 ±1.8	-3.0 ±1.5	1.0 ± 5.0
SADA	-15.8856	64.9362	6.7 ±1.8	-0.3 ±1.5	2.1 ± 4.5
SAUD	-15.8837	64.8984	2.2 ±0.5	-2.2 ±0.4	-18.2± 1.2
SFEL	-15.7988	64.9291	5.2 ±1.5	-11.4±1.4	9.9 ± 4.5
SHAL	-15.8730	64.9104	6.2 ±1.5	0.2 ±1.5	-15.8± 4.7
SNES	-15.4652	64.8210	-2.5 ±1.8	5.1 ±1.7	-39.0± 5.4
SNSK	-15.6421	64.8082	5.8 ±2.0	4.2 ±1.6	1.1 ± 5.3
THMY	-15.9554	64.8648	9.2 ±1.8	1.1 ±2.0	-27.3± 6.6
THUD	-15.6128	64.8860	-1.2 ±1.7	4.8 ±1.6	10.3 ± 5.1
TROL	-15.9315	64.8758	8.5 ±1.8	10.0 ±2.2	6.4 ± 7.3
TUNG	-15.6508	64.9151	-5.4 ±1.7	11.4 ±1.5	-6.6 ± 4.3
VEOR	-15.8136	64.8506	2.2 ±1.7	8.4 ±1.7	-27.4± 5.2
VEVO	-16.0124	64.8895	11.4 ±1.6	-2.5 ±1.5	16.1 ± 4.8
VIKD	-15.9508	65.0712	2.0 ±1.8	7.0 ±1.9	-35.7± 6.2

Appendix B

Time Series of displacements

The following figures show the time series of displacements along with the least square fit for the two intervals 2005-2006 and 2006-2007. The NNR-NUVEL1A velocity of each station has been subtracted from the time series. The time series shown are from the stations in Appendix A.2.

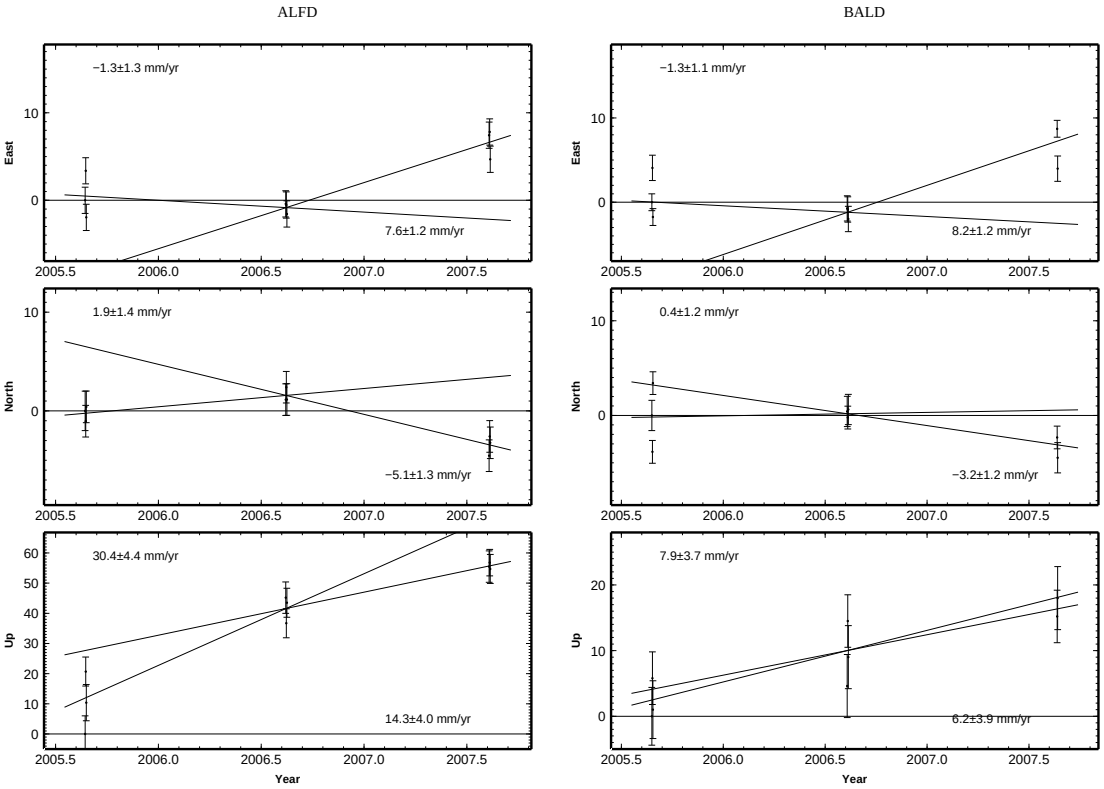
ALFD
East
−1.3±1.3 mm/yr
7.6±1.2 mm/yr
North
1.9±1.4 mm/yr
−5.1±1.3 mm/yr
Up
30.4±4.4 mm/yr
14.3±4.0 mm/yr
Year
BALD
East
−1.3±1.1 mm/yr
8.2±1.2 mm/yr
North
0.4±1.2 mm/yr
−3.2±1.2 mm/yr
Up
7.9±3.7 mm/yr
6.2±3.9 mm/yr
Year

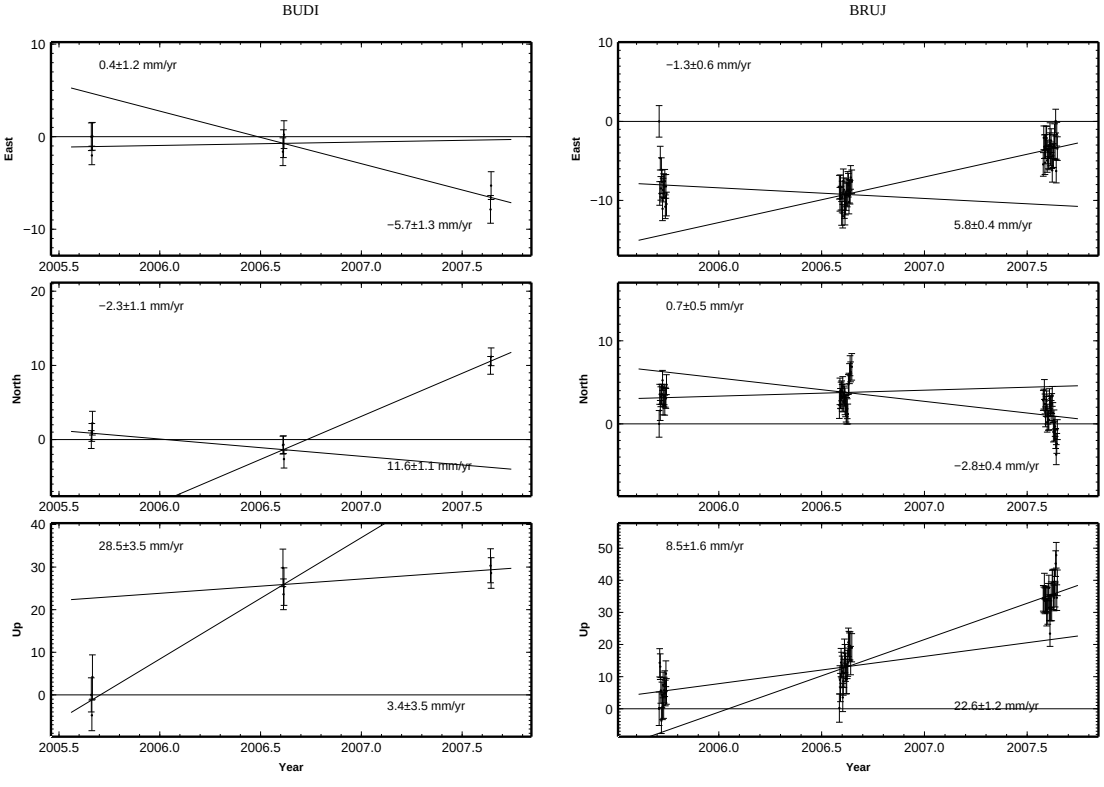
BUDI
East
0.4±1.2 mm/yr
−5.7±1.3 mm/yr
North
−2.3±1.1 mm/yr
11.6±1.1 mm/yr
Up
28.5±3.5 mm/yr
3.4±3.5 mm/yr
Year
BRUJ
East
−1.3±0.6 mm/yr
5.8±0.4 mm/yr
North
0.7±0.5 mm/yr
−2.8±0.4 mm/yr
Up
8.5±1.6 mm/yr
22.6±1.2 mm/yr
Year

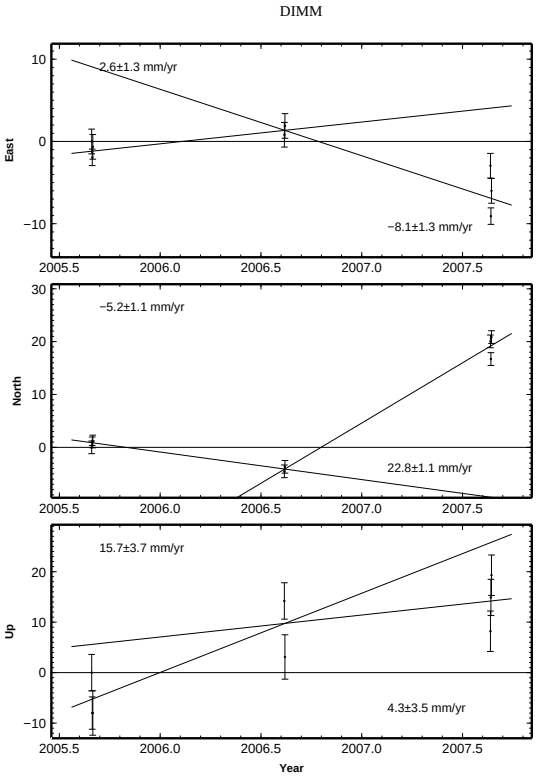
DIMM
East
2.6±1.3 mm/yr
−8.1±1.3 mm/yr
North
−5.2±1.1 mm/yr
22.8±1.1 mm/yr
Up
15.7±3.7 mm/yr
4.3±3.5 mm/yr
Year

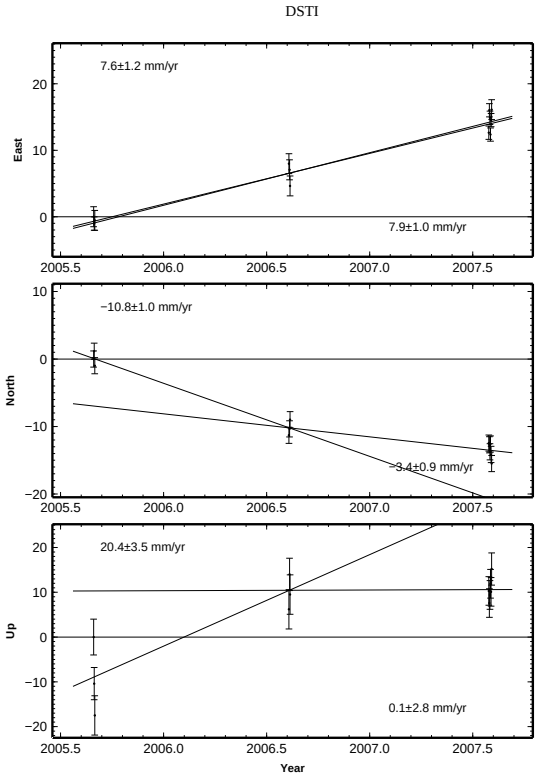
DSTI
East
7.6±1.2 mm/yr
7.9±1.0 mm/yr
North
−10.8±1.0 mm/yr
−3.4±0.9 mm/yr
Up
20.4±3.5 mm/yr
0.1±2.8 mm/yr
Year

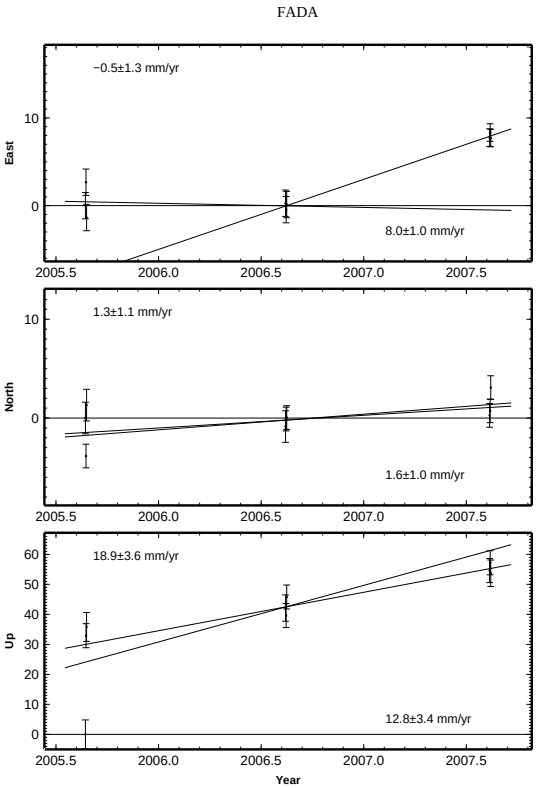
FADA
East
−0.5±1.3 mm/yr
8.0±1.0 mm/yr
North
1.3±1.1 mm/yr
1.6±1.0 mm/yr
Up
18.9±3.6 mm/yr
12.8±3.4 mm/yr
Year

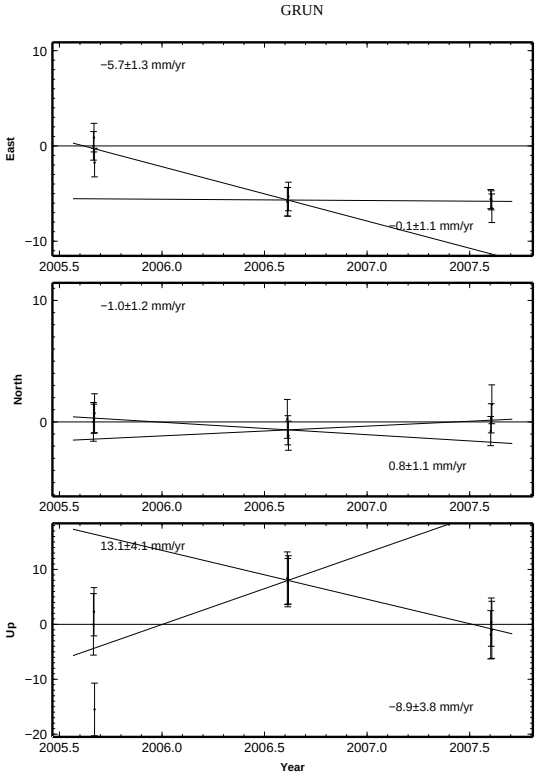
GRUN
East
−5.7±1.3 mm/yr
−0.1±1.1 mm/yr
North
−1.0±1.2 mm/yr
0.8±1.1 mm/yr
Up
13.1±4.1 mm/yr
−8.9±3.8 mm/yr
Year

HAHV

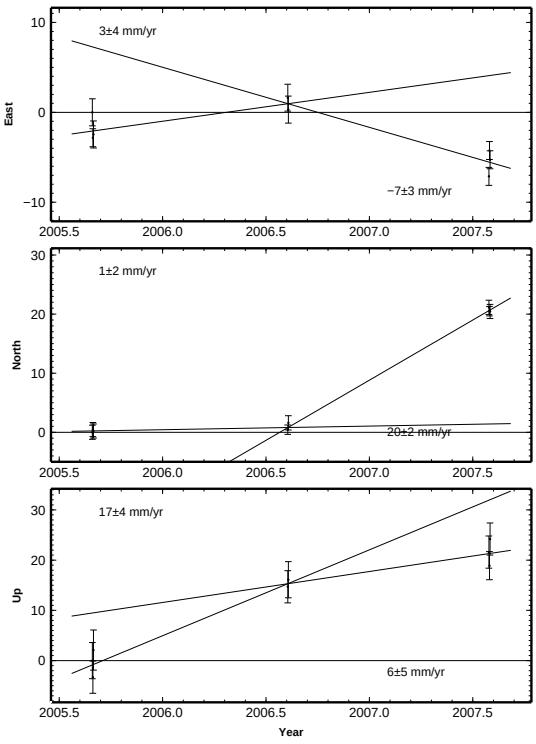

HALS

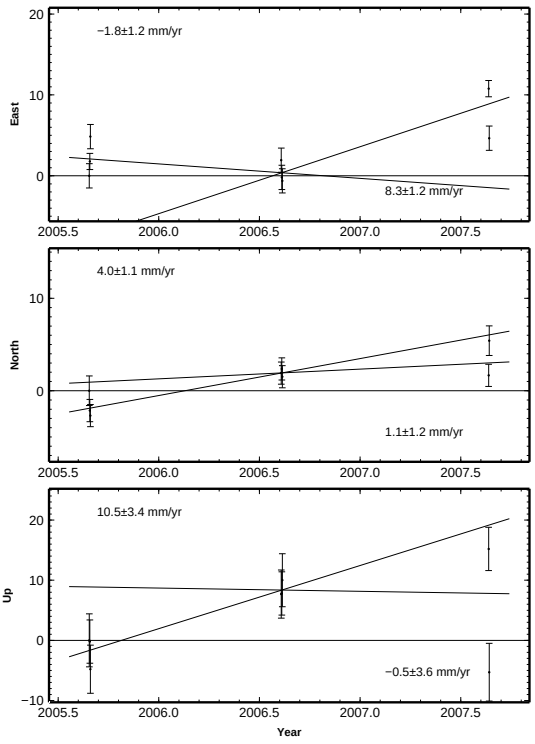

HATU

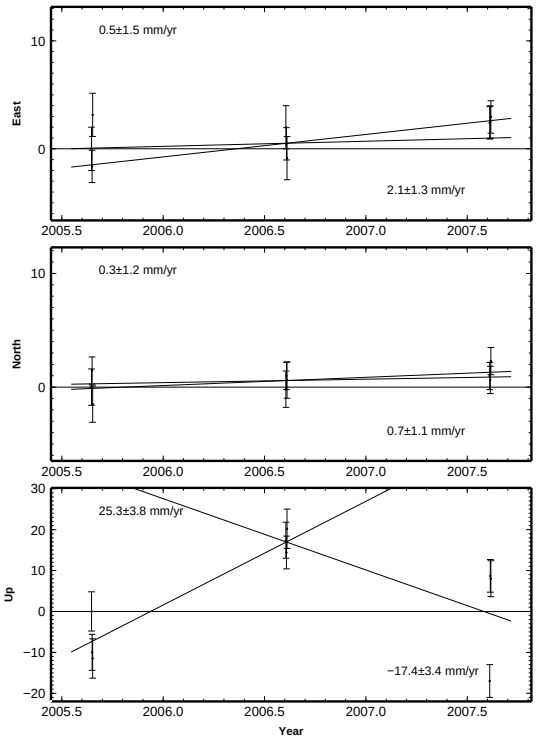

HDAL

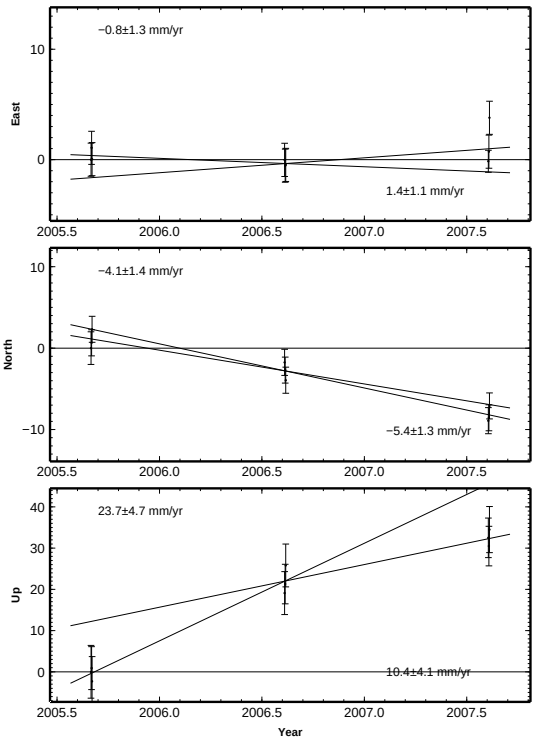

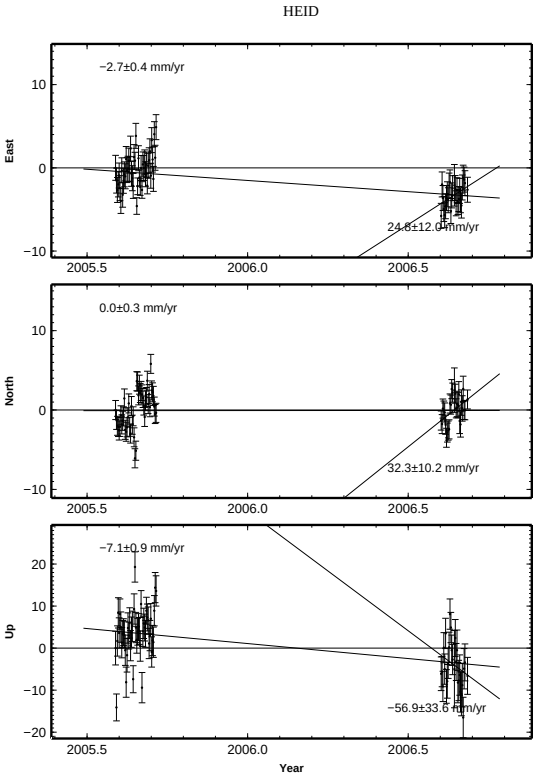
HEID
East
−2.7±0.4 mm/yr
24.8±12.0 mm/yr
North
0.0±0.3 mm/yr
32.3±10.2 mm/yr
Up
−7.1±0.9 mm/yr
−56.9±33.6 mm/yr
Year

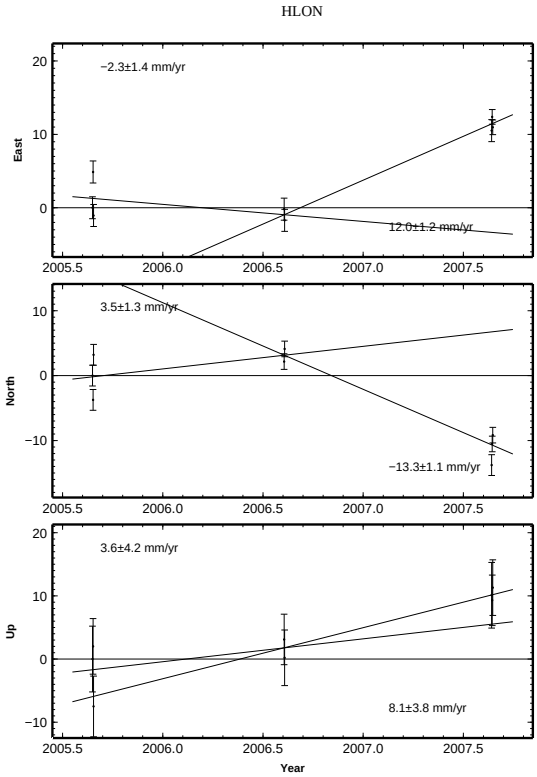
HLON
East
−2.3±1.4 mm/yr
12.0±1.2 mm/yr
North
3.5±1.3 mm/yr
−13.3±1.1 mm/yr
Up
3.6±4.2 mm/yr
8.1±3.8 mm/yr
Year

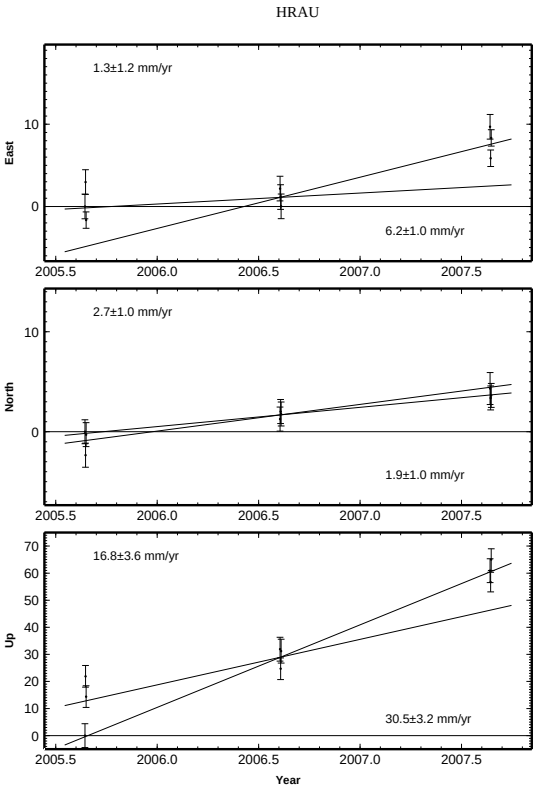
HRAU
East
1.3±1.2 mm/yr
6.2±1.0 mm/yr
North
2.7±1.0 mm/yr
1.9±1.0 mm/yr
Up
16.8±3.6 mm/yr
30.5±3.2 mm/yr
Year

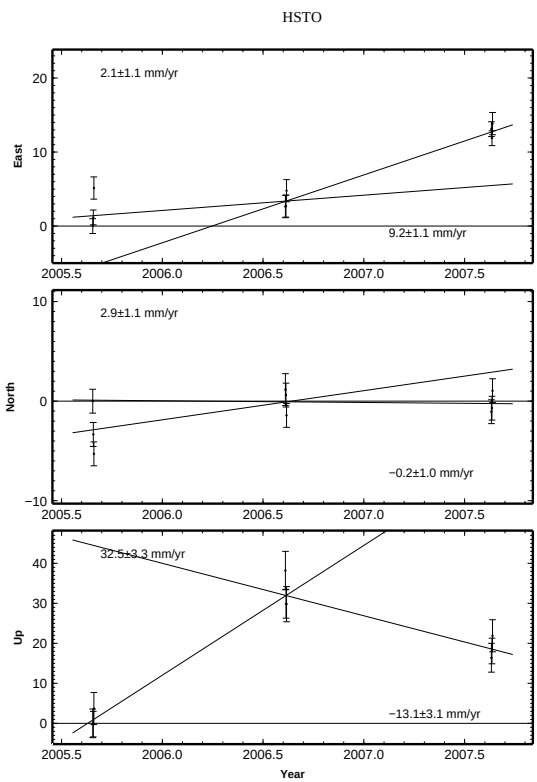
HSTO
East
2.1±1.1 mm/yr
9.2±1.1 mm/yr
North
2.9±1.1 mm/yr
−0.2±1.0 mm/yr
Up
32.5±3.3 mm/yr
−13.1±3.1 mm/yr
Year

KARA

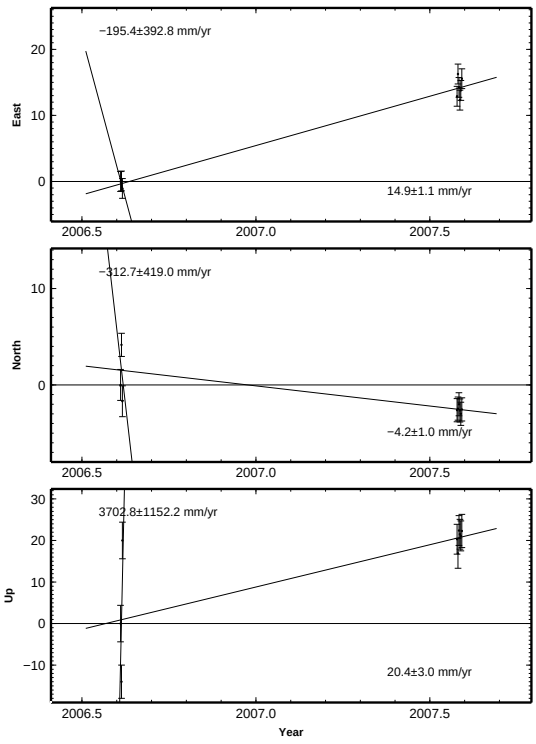

KARV

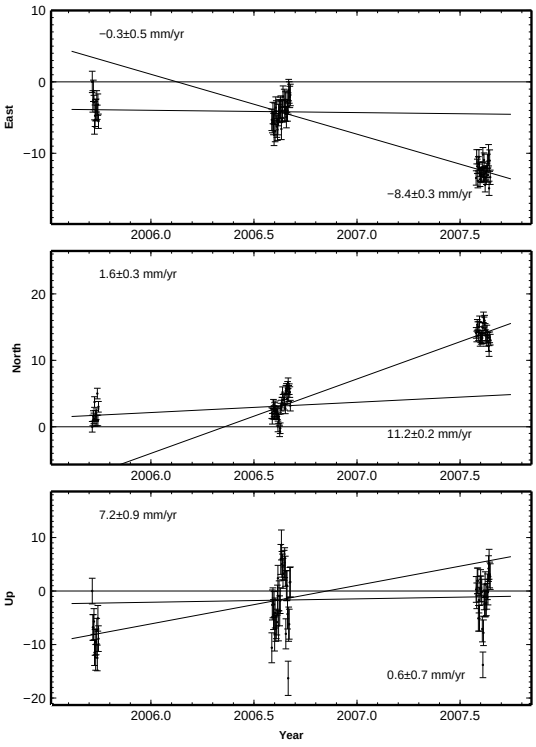

KRIN

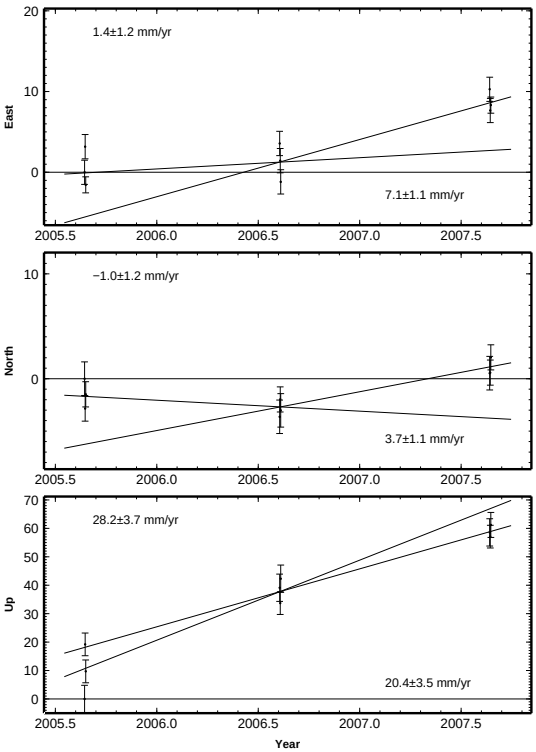

KVAR

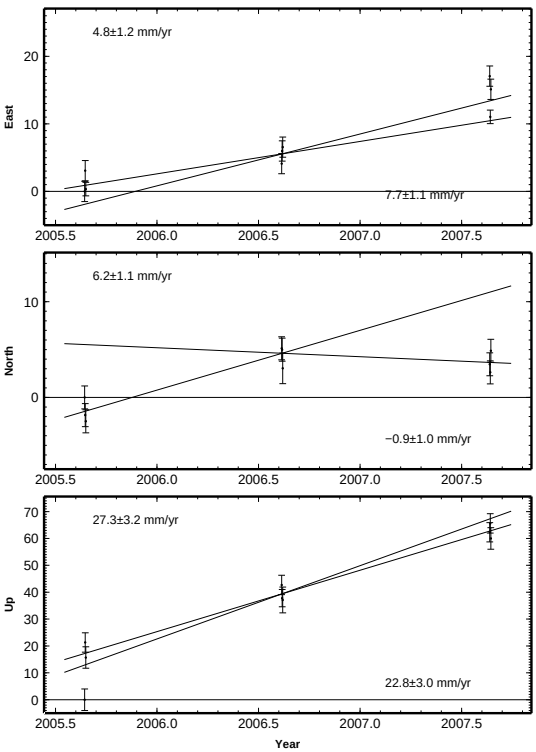

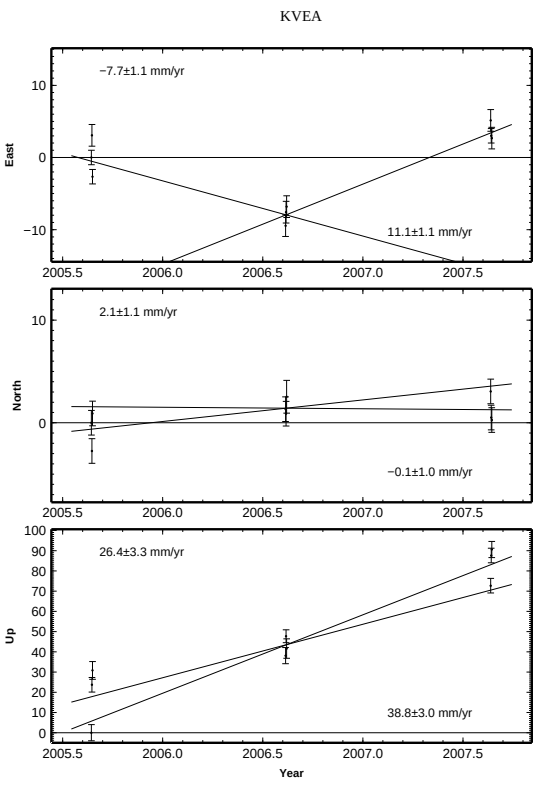
KVEA
East
−7.7±1.1 mm/yr
11.1±1.1 mm/yr
North
2.1±1.1 mm/yr
−0.1±1.0 mm/yr
Up
26.4±3.3 mm/yr
38.8±3.0 mm/yr
Year

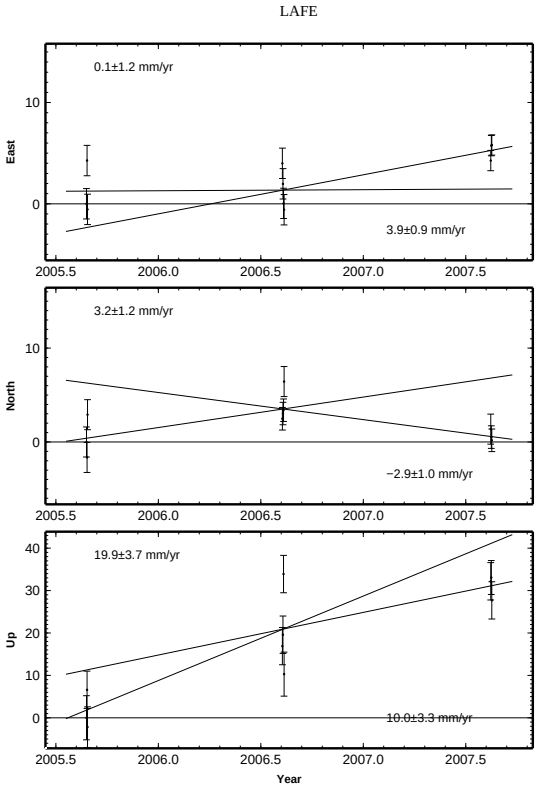
LAFE
East
0.1±1.2 mm/yr
3.9±0.9 mm/yr
North
3.2±1.2 mm/yr
−2.9±1.0 mm/yr
Up
19.9±3.7 mm/yr
10.0±3.3 mm/yr
Year

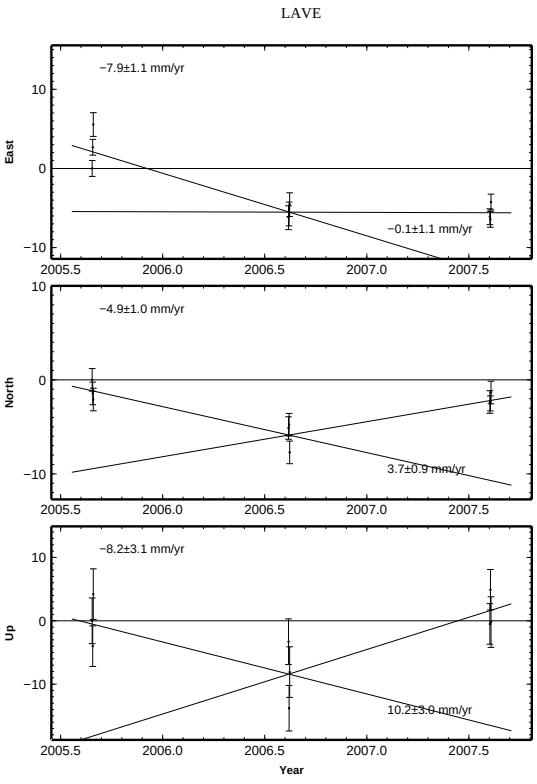
LAVE
East
−7.9±1.1 mm/yr
−0.1±1.1 mm/yr
North
−4.9±1.0 mm/yr
3.7±0.9 mm/yr
Up
−8.2±3.1 mm/yr
10.2±3.0 mm/yr
Year

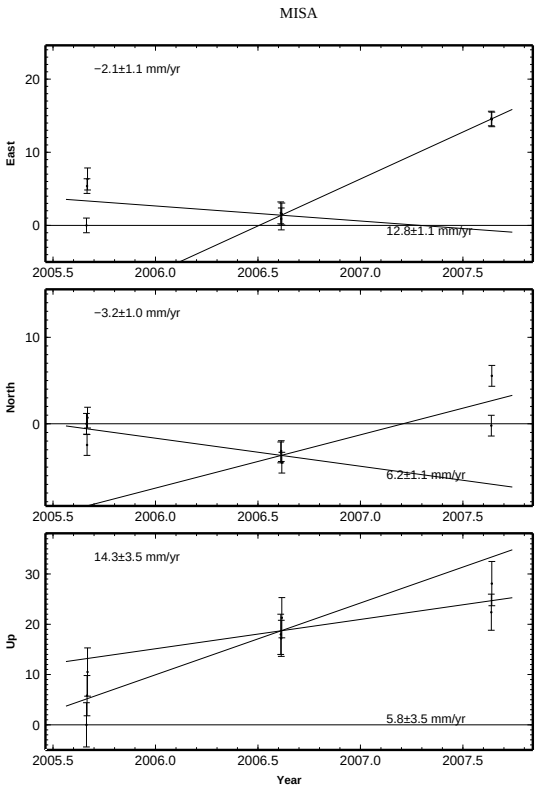
MISA
East
−2.1±1.1 mm/yr
12.8±1.1 mm/yr
North
−3.2±1.0 mm/yr
6.2±1.1 mm/yr
Up
14.3±3.5 mm/yr
5.8±3.5 mm/yr
Year

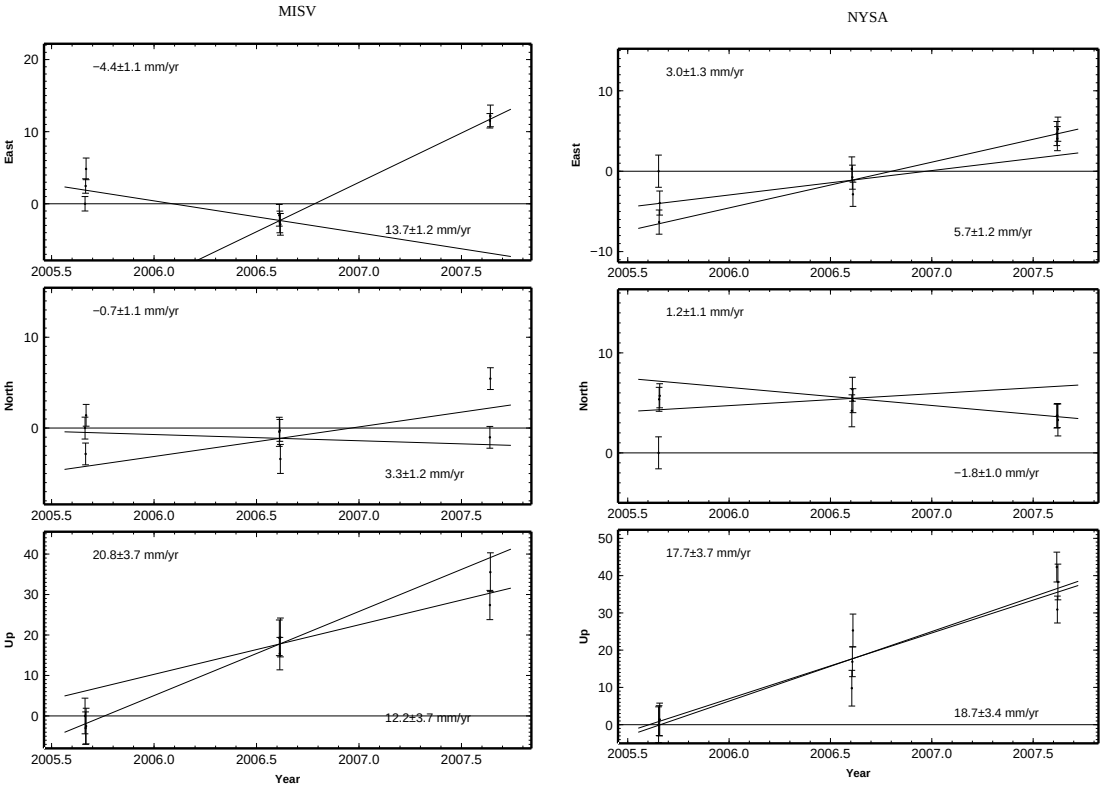
MISV
East
−4.4±1.1 mm/yr
13.7±1.2 mm/yr
North
−0.7±1.1 mm/yr
3.3±1.2 mm/yr
Up
20.8±3.7 mm/yr
12.2±3.7 mm/yr
Year
NYSA
East
3.0±1.3 mm/yr
5.7±1.2 mm/yr
North
1.2±1.1 mm/yr
−1.8±1.0 mm/yr
Up
17.7±3.7 mm/yr
18.7±3.4 mm/yr
Year

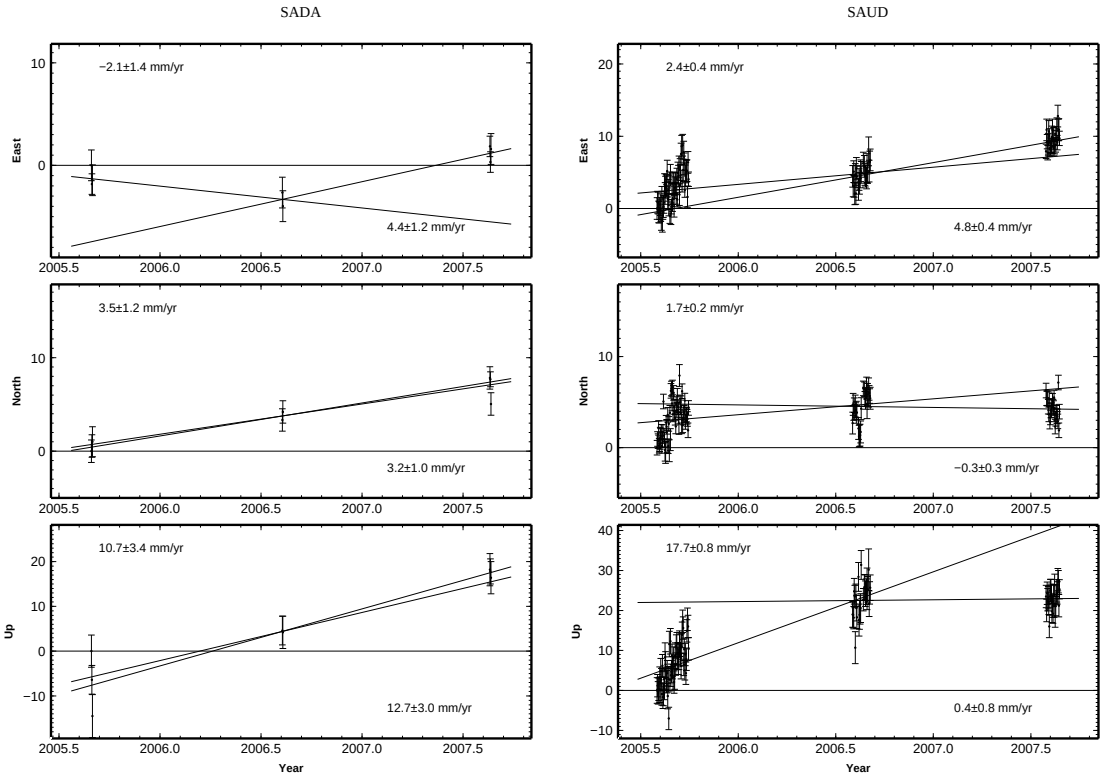
SADA
East
−2.1±1.4 mm/yr
4.4±1.2 mm/yr
North
3.5±1.2 mm/yr
3.2±1.0 mm/yr
Up
10.7±3.4 mm/yr
12.7±3.0 mm/yr
Year
SAUD
East
2.4±0.4 mm/yr
4.8±0.4 mm/yr
North
1.7±0.2 mm/yr
−0.3±0.3 mm/yr
Up
17.7±0.8 mm/yr
0.4±0.8 mm/yr
Year

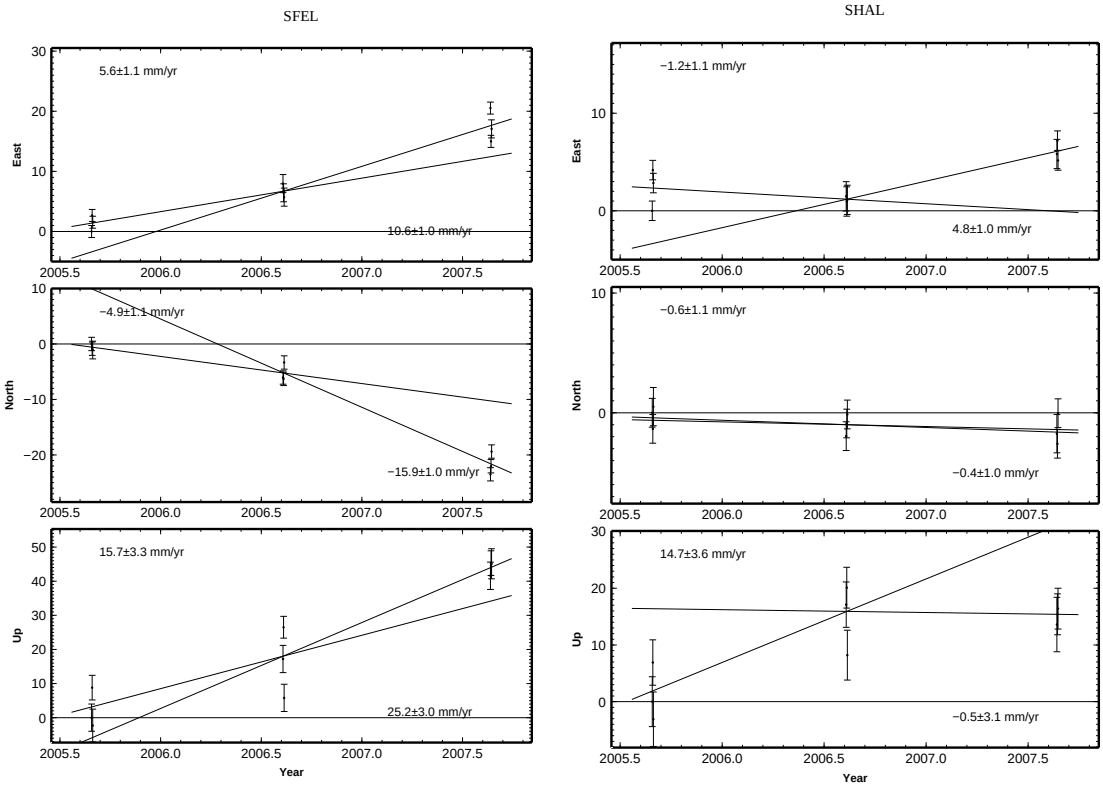
SFEL
5.6±1.1 mm/yr
10.6±1.0 mm/yr
East
−4.9±1.1 mm/yr
−15.9±1.0 mm/yr
North
15.7±3.3 mm/yr
25.2±3.0 mm/yr
Up
Year
SHAL
−1.2±1.1 mm/yr
4.8±1.0 mm/yr
East
−0.6±1.1 mm/yr
−0.4±1.0 mm/yr
North
14.7±3.6 mm/yr
−0.5±3.1 mm/yr
Up
Year

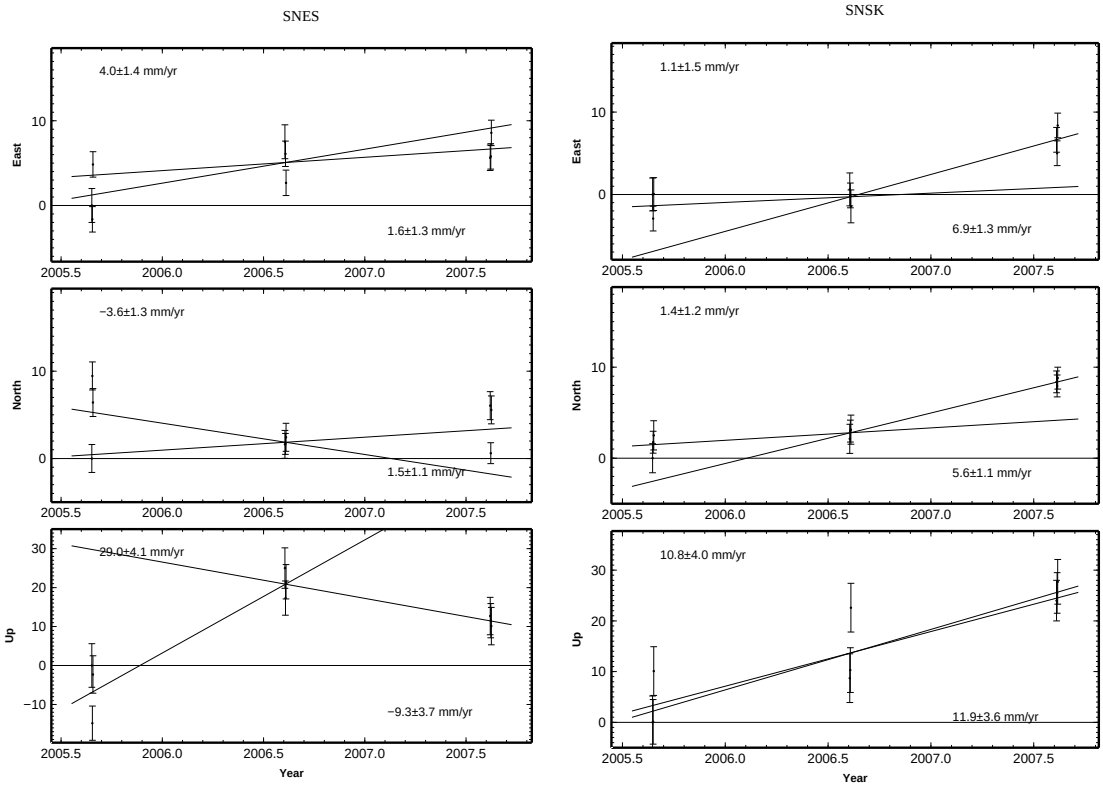
SNES
4.0±1.4 mm/yr
1.6±1.3 mm/yr
East
−3.6±1.3 mm/yr
1.5±1.1 mm/yr
North
29.0±4.1 mm/yr
−9.3±3.7 mm/yr
Up
Year
SNSK
1.1±1.5 mm/yr
6.9±1.3 mm/yr
East
1.4±1.2 mm/yr
5.6±1.1 mm/yr
North
10.8±4.0 mm/yr
11.9±3.6 mm/yr
Up
Year

THMY

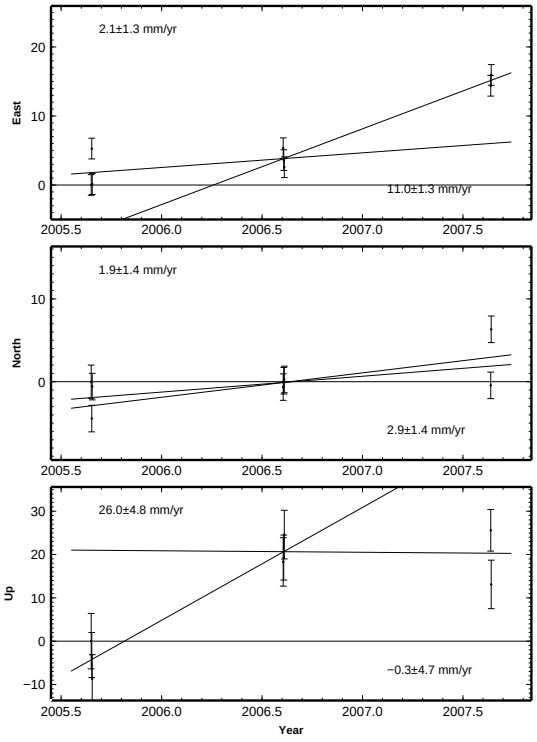

THUD

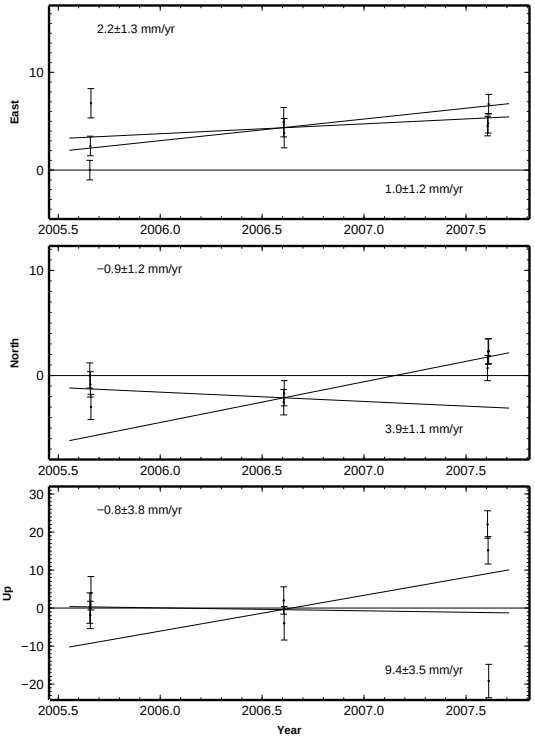

TROL

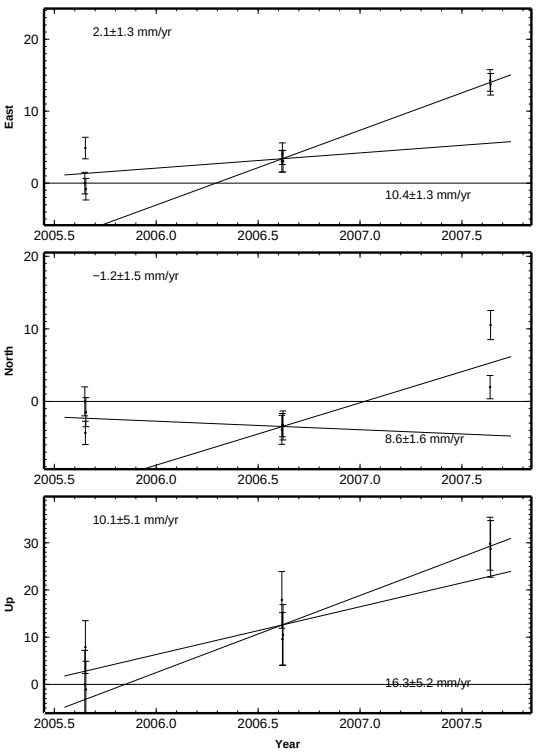

TUNG

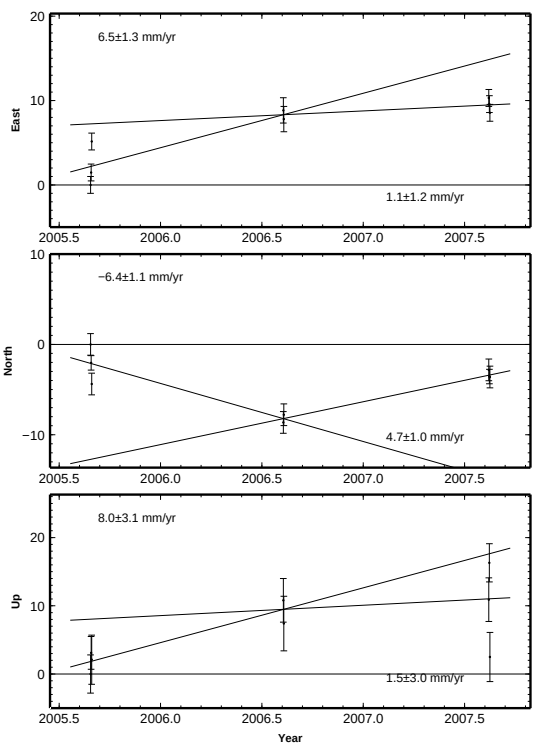

VEOR

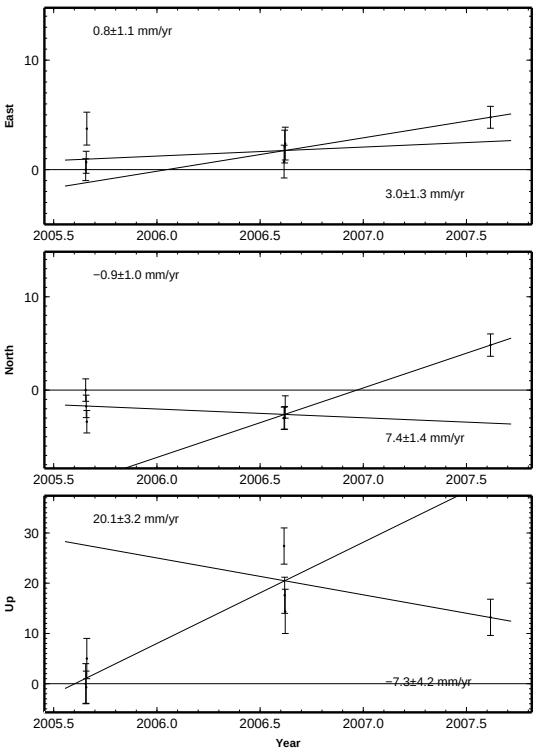

VEVO

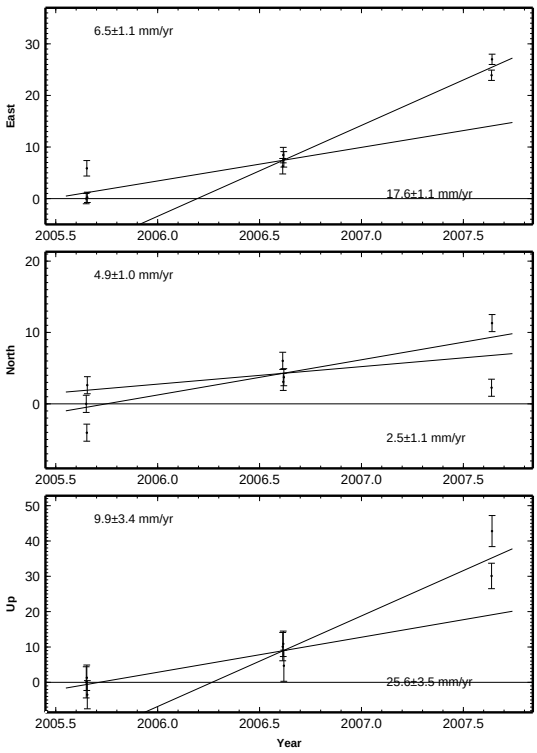

VIKD